Deciphering drip-line decays

- the case of ^{31}Ar

Gunvor T. Koldste

Department of Physics and Astronomy
Aarhus University, Denmark

Dissertation for the degree
of Doctor of Philosophy

September 2015

Gunvor T. Koldste
Department of Physics and Astronomy
Aarhus University
Ny Munkegade, Bldg. 1520
8000 Aarhus C
Denmark

This dissertation has been submitted to the Faculty of Science at Aarhus University, Denmark, in partial fulfilment of the requirements for the PhD degree in physics. The work presented has been performed in the period from August 2010 to August 2015 under the supervision of Hans O. U. Fynbo and Karsten Riisager. The experimental work was carried out at the ISOLDE facility at CERN, Switzerland in August 2009 and the analysis work was mainly carried out at the Department of Physics and Astronomy in Aarhus.

Contents

Summary

^{31}Ar is the last argon isotope that is stable against proton emission. It lies at the proton drip-line (where the nuclei become unstable with respect to proton emission) and has a large energy window for beta emission. This along with small proton separation energies of the daughter make its decay very complex with many open decay modes.

In this thesis we study the exotic three-proton decay mode, which was only recently discovered in the decay of ^{31}Ar and has only been observed in two other nuclei. We perform the first spectroscopic analysis of this decay mode made possible by the good resolution of our setup and its large solid angle for particle detection.

All the proton decay modes are examined in detail to extract the beta-strength and to investigate the evolution of the proton decay modes. From this study we propose a simple model to predict the beta-delayed one-, two- and three-proton branching ratios of other nuclei and test it on the decay of ^{39}Ti and ^{43}Cr.

Finally, we use the decay of ^{31}Ar to study the levels of the beta-proton daughter ^{30}S, which are relevant to astrophysics. These levels are normally studied in reaction experiments using stable nuclei, but we show that, even though we populate the levels from the drip-line, we are able to study the spectroscopic properties on a competing level. We provide the first experimental limits on the ratio between the proton and gamma partial widths of the levels in ^{30}S just above the proton threshold. These influence the $^{29}\mathrm{P}(p,\gamma)^{30}\mathrm{S}$ reaction rate, which are relevant when studying type I X-ray bursts and presolar dust grains from classical novae.

Dansk resumé (Summary in Danish)

^{31}Ar er det sidste argon isotop der er stabilt overfor protonudsendelse. Den ligger på protondryplinjen (hvor kerner bliver ustabile overfor protonudsendelse) og har et meget stort energivindue for betaemission. Dette sammen med små protonseparationsenergier af datteren gør dens henfald meget komplekst med mange åbne henfaldskanaler.

I denne afhandling studerer vi det eksotiske tre-protonhenfald, der kun for nyligt er opdaget i henfaldet af ^{31}Ar og som kun er observeret i to andre kerner. Vores kompakte opstilling med god opløsning og stor effektivitet for protondetektion har gjort det muligt at lave den første spektroskopiske analyse af denne henfaldstype.

Alle protonhenfaldskanalerne er undersøgt i detalje for at ekstrahere betastyrken og for at undersøge udviklingen af protonhenfaldskanalerne. På baggrund af denne undersøgelse opstiller vi en model til at forudsige forgreningsforholdene af det betaforsinkede en-, to- og tre-protonhenfald for andre kerner og tester det på henfaldet af ^{39}Ti og ^{43}Cr.

Endeligt bruger vi henfaldet af ^{31}Ar til at undersøge niveauerne af beta-protondatteren ^{30}S, som er relevant for astrofysik. Disse niveauer bliver normalt studeret i reaktionseksperimenter med stabile kerner, men vi viser at vi kan undersøge de spektroskopiske egenskaber på et tilsvarende niveau selvom vi populerer niveauerne fra dryplinjen. Vi finder de første eksperimentelle grænser på forholdet mellem proton- og gamma-henfaldsbredderne af niveauerne i ^{30}S lige over protontærskelen. Disse påvirker reaktionsraten af reaktionen $^{29}\mathrm{P}(p,\gamma)^{30}\mathrm{S}$, som er relevant for studier af type I røngtenstråleudbrud og støvkorn produceret i klassiske novaer før dannelsen af vores solsystem.

Preface

A single experiment form the basis of this thesis. The reason for this is that the ^{31}Ar data set of this experiment has contained so much physics that it has not been possible in the time of a PhD to study it all. I have focused on the parts that have not previously been studied, i.e. what new physics we could learn from the data.

The first year of my PhD I worked on ^{9}Li data from an experiment made in 2005 and on production of neutron deficient carbon beams. I spend three months from April 2010 at CERN working with the ISOLDE target group helping with the latter. Throughout my PhD I have also taken part in a number of experiments and tests performed at ISOLDE.

The ^{31}Ar experiment IS476 was performed in August 2009 before I started my PhD studies. I had made simulations of the setup as part of my Bachelor's project and since I was a summer student at ISOLDE that summer I participated in the experiment. The analysis presented here has mainly been performed in a period from August 2011 to August 2015 (with a one year break from March 2014). The work has resulted in three papers [Kol13,Kol14a, Kol14b], which all form the basis of this thesis. In the time between the first paper and the other two I made significant improvements to my analysis program. For this reason I have re-analysed the data and present here improved results of the first paper. Further analysis has been performed since the last paper was published and are also presented here.

List of Publications

I. [Kol14b]
Sizeable beta-strength in ^{31}Ar (β3p) decay
G. T. Koldste, B. Blank, M. J. G. Borge, J. A. Briz, M. Carmona-Gallardo, L. M. Fraile, H. O. U. Fynbo, J. Giovinazzo, J. G. Johansen, A. Jokinen, B. Jonson, T. Kurturkian-Nieto, T. Nilsson, A. Perea, V. Pesudo, E. Picado, K. Riisager, A. Saastamoinen, O. Tengblad, J.-C. Thomas, J. Van de Walle.
Physics Letters B **737**, 383 (2014).

II. [Kol14a]
Multiparticle emission in the decay of ^{31}Ar
G. T. Koldste, B. Blank, M. J. G. Borge, J. A. Briz, M. Carmona-Gallardo, L. M. Fraile, H. O. U. Fynbo, J. Giovinazzo, B. D. Grann, J. G. Johansen, A. Jokinen, B. Jonson, T. Kurturkian-Nieto, J. H. Kusk, T. Nilsson, A. Perea, V. Pesudo, E. Picado, K. Riisager, A. Saastamoinen, O. Tengblad, J.-C. Thomas, J. Van de Walle.
Physical Review C **89**, 064315 (2014).

III. [Ram14]
Intense 31-35Ar beams produced with nano-structured CaO target at ISOLDE.
J.P. Ramos, A. Gottberg, T.M. Mendonça, C. Seiffert, A.M.R. Senos, H.O.U. Fynbo, O. Tengblad, J.A. Briz, M.V. Lund, **G. T. Koldste**, M. Carmona-Gallardo, V. Pesudo, T. Stora.
Nuclear Instruments and Methods in Physics Research Section B: Beam Interactions with Materials and Atoms **320**, 83 (2014).

IV. [Joh13]
Experimental study of bound states in ^{12}Be through low-energy ^{11}Be(d,p)-transfer reactions.
J. G. Johansen, V. Bildstein, M. J. G. Borge, M. Cubero, J. Diriken, J. Elseviers, L. M. Fraile, H. O. U. Fynbo, L. P. Gaffney, R. Gernhäuser, B. Jonson, **G. T. Koldste**, J. Konki, T. Kröll, R. Krücken, D. Mücher, T. Nilsson, K. Nowak, J. Pakarinen, V. Pesudo, R. Raabe, K. Riisager, M. Seidlitz, O. Tengblad, H. Törnqvist, D. Voulot, N. Warr, F. Wenander, K. Wimmer, H. De Witte.
Physical Review C **88**, 044619 (2013).

V. [Kol13]
Relative proton and γ widths of astrophysically important states in ^{30}S studied in the β-delayed decay of ^{31}Ar.
G. T. Koldste, B. Blank, M. J. G. Borge, J. A. Briz, M. Carmona-Gallardo, L. M. Fraile, H. O. U. Fynbo, J. Giovinazzo, J. G. Johansen, A. Jokinen, B. Jonson, T. Kurturkian-Nieto, J. H. Kusk, T. Nilsson, A. Perea, V. Pesudo, E. Picado, K. Riisager, A. Saastamoinen, O. Tengblad, J.-C. Thomas, J. Van de Walle.
Physical Review C **87**, 055808 (2013).

VI. *The resonances of ^{30}S and the ^{29}P(p,γ)^{30}S reaction*.
G. T. Koldste, IS476 Collaboration.
Proceeding of Science, NIC XII, 205 (2012).

Acknowledgements

First I would like to thank my supervisors Karsten Riisager and Hans O. U. Fynbo for their support and guidance in the last seven years. In particular I would like to thank them for supporting my aspirations — even when they changed, and for their positive attitude when I needed encouragement. A special thanks to my main supervisor Karsten for making sure I took time off when needed and for trusting me to finish my PhD from England.

I would very much like to thank the experimental and theoretical nuclear groups for discussions of both academic and non-academic character. I would also like give a special thanks to my classmates and my friends from the department, TAAGEKAMMERET and the Physics Friday Bar who have made my university years colourful and unforgettable.

I would like to thank the people who participated in the IS476 experiment and our collaborators in Madrid and Gothenburg. A special thanks to Olof Tengblad for teaching me about electronics and to Maria J. G. Borge and Björn Jonson for discussions about ^{31}Ar and for making me feel that my work was valuable. I would also like to thank the physics group and the target group at ISOLDE for their hospitality during my three month stay with them and during the experiments and tests I have participated in.

I would also very much like to thank my parents for all their support and encouragement throughout the years and my father for introducing me to the interesting world of physics. My daughter Luna deserves a special thank for bringing me joy and teaching me that I cannot prepare for everything. I would also like to thank my aunt Bodil Vendelev for proofreading this thesis.

Finally my beloved husband Thomas deserve a great appreciation and thank. Without him this work would have never been possible. I would like to thank him for our physics discussions, for his technical and programming support and for his inputs on and proofreading of this thesis. I would also very much like to thank him for all his encouragement, support and comfort, for making everything work at home and for listening to me and believing in me.

CHAPTER 1

Introduction

The elusive Higgs boson was recently discovered at CERN [CMS12, ATL12] providing the last missing piece of the Standard Model. Together with Einstein's general relativity, the Standard Model forms our current picture of the world by describing the basic building blocks of matter and their interactions through the four fundamental forces. The Standard Model was finalised in the mid seventies as a gauge theory for the electromagnetic, the weak and the strong interactions, including 18 elementary particles (not counting the anti-particles of the fermions and colour states of the quarks and gluon). The theory was verified with the discovery of a number of these particles predicted by the model (the W and Z bosons, the gluon and the top, bottom and charm quarks), but it was not until the discovery of the Higgs boson in 2013 that the validation of the theory was finally cemented.

One of the major challenges for the Standard Model is to bridge between the few-particle interactions between quarks and the many-body interactions of collective states of nucleons and nuclei. This is due to the strong interaction, described by Quantum Chromo Dynamics (QCD), which is responsible for the binding of quarks in nucleons and nucleons in nuclei. Unlike the electromagnetic and the weak force, QCD is a strongly coupled theory at low energy. This means that while observables can be computed to exquisite precision in both the weak and the electromagnetic part of the Standard Model, this is not the case for QCD. Computing the spectrum of bound states in QCD, for instance, is a non-trivial numerical task: The state-of-the-art is currently limited to the proton and the deuteron [Dür08, Bea12]. Not even the newly discovered pentaquark resonance [LHC15] and the recently confirmed tetraquark resonance [Bel08, Bel13, LHC14] were predicted by the numerical computations.

Thus we find ourselves in the peculiar situation that we believe we have the correct theory for the interactions but we cannot even compute the mass

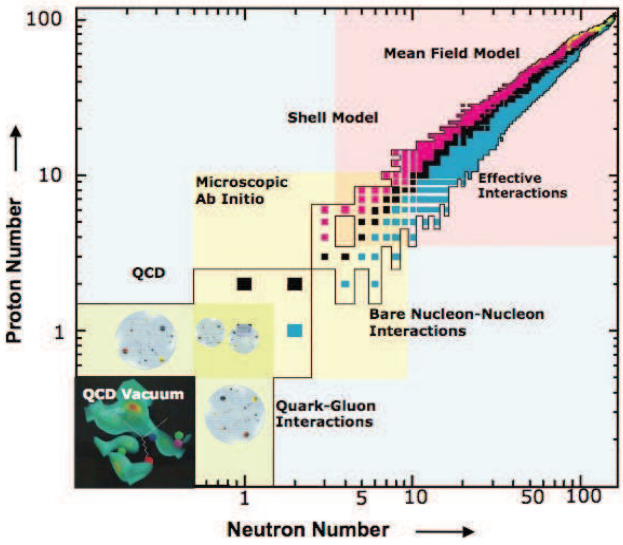

Figure 1.1: The nuclear chart indicating the regions of use for different models. Note that the regions overlap; the hope is to be able to bridge between the different models and to the basic theory QCD of the strong interaction.

and structure of nuclei. To proceed we must rely on effective models of the nuclear forces guided by experiments. However, we need different models to describe different regions of the nuclear chart as illustrated in Figure 1.1. Since the regions overlap the long term aim is to bridge between them and possibly calculate some input parameters from the more basic theory lying beneath. The first bridge between QCD and ab-initio theories with free nucleon-nucleon interactions (the green and the yellow part in Figure 1.1) is currently limited by computational power, while the latter bridge between the yellow and the red part in Figure 1.1 needs better comprehension of how nuclear degrees of freedom (e.g. collective behaviour) emerge from ab-initio theories. Furthermore, new experimental data is needed to refine and test ab-initio and effective field theories.

The field of nuclear physics is thus still very open, even though the fundamental interactions behind are believed to be more or less well known. The reason for this is to a large extent that more is different [And72], so we need not only to understand the interactions, but also the collective behaviour. The

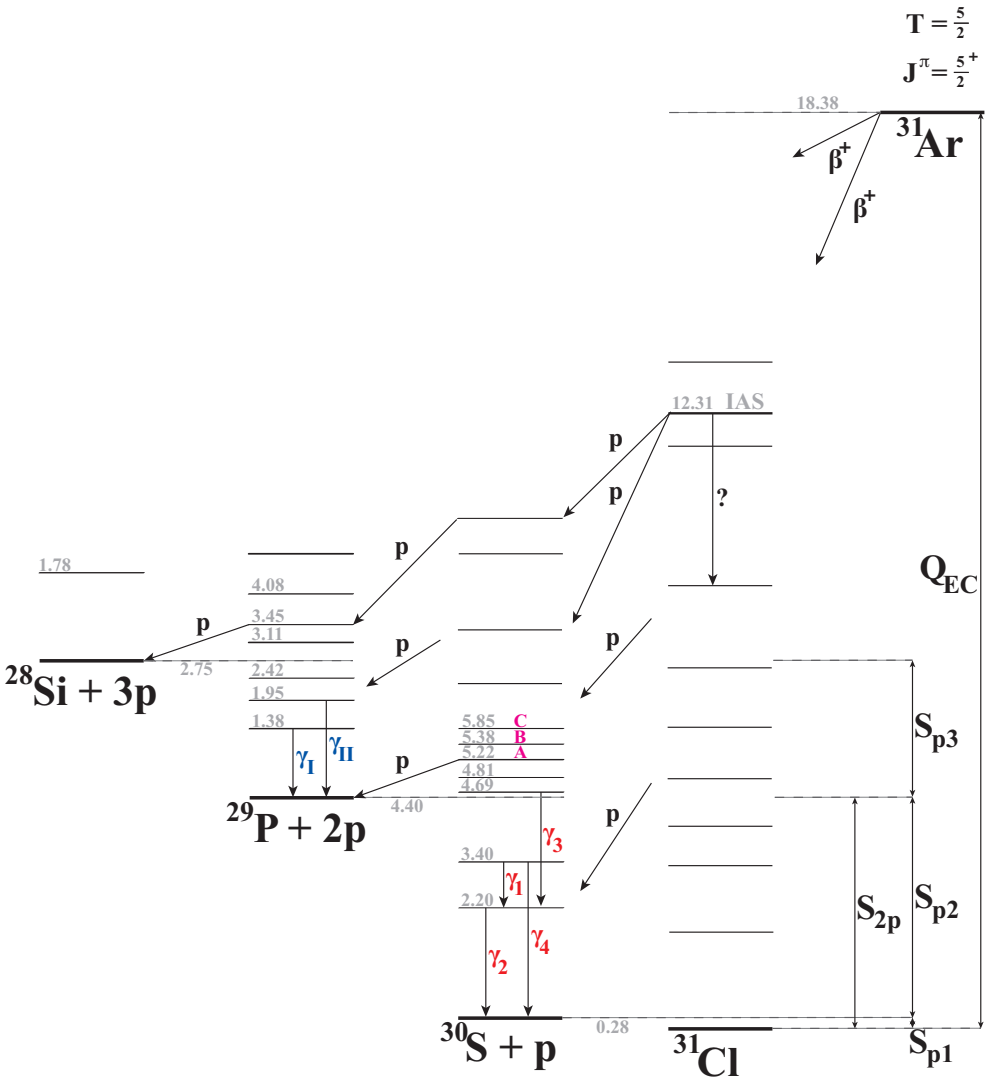

Figure 1.2: The decay scheme of ^{31}Ar. Different proton decays are drawn as an illustration. Some of the most important levels for this thesis are shown and labelled with their excitation energy. The levels marked by letters in ^{30}S correspond to Figure 6.1 and the marked gamma transitions correspond to Figure 6.2 from Chapter 6. The proton separation energies are also shown.

nuclear chart currently counts about 3000 nuclei [Erl12] and we cannot wait for the development of the theoretical models to answer some of the questions arising: What are the boundaries of the nuclear chart? Which decay modes exist? How were the nuclei produced in the early Universe? And many more. These questions can only be answered from experiments studying the structure of the nuclei. In principle all nuclei should be examined in detail, but this is not possible and instead we focus on nuclei that can help answer as many questions as possible and which can be produced in large enough numbers to allow a detailed study.

The topic of this thesis is the decay of the nucleus ^{31}Ar, which is the last argon isotope that is stable against proton emission. Since it lies at the proton drip-line (where the nuclei become unstable with respect to proton emission) the energy window for beta-emission is very large, which means that many states, some even with high energy, are fed in the beta-daughter. This is of course the case for most nuclei along the proton drip-line, but the beauty of ^{31}Ar is that it can be produced with a high yield as a radioactive beam, and it is thus possible to study the decay in great detail.

The decay of ^{31}Ar is very complex as can be seen in Figure 1.2. To decipher this decay we thus need a detailed understanding of both the weak, the strong and the electromagnetic interaction. The extracted matrix elements between the populated levels allow us to follow the development of the structure.

As seen in Figure 1.2 the large beta-window entails that many different decay modes are open. The beta-delayed three-proton decay is a newly discovered decay mode and has only been observed in two other nuclei so far [Pom11, Aud12b]. In this thesis we present the first spectroscopic analysis of this exotic decay mode (Chapter 7). The one- and two-proton decay have been studied in many previous experiments (see Section 2) and are mainly used here (together with subsequent gamma decays) as a tool for assigning the beta-strength (Chapter 8) and for studying the structure of the levels of the beta-proton daughter ^{30}S (Chapter 6), which are relevant to astrophysics (Section 2.2).

1.1 Beta decay

- an effect of the weak interaction

Beta decay is a decay through the weak interaction, which changes the isospin of the nucleon, i.e it. changes a neutron into a proton and vice versa. There are three types of nucleon changing weak decays: β^-, β^+ and electron capture (EC). In the β^- decay a neutron is transformed into a proton and it is thus the dominating decay mode on the neutron rich side of stability. In the β^+ decay and for electron capture the opposite reaction occurs creating a neutron from a proton and these processes thus dominate the proton rich side of stability.

The three decay processes follow the reactions

$$\beta^- : \quad (A, Z) \longrightarrow (A, Z+1) + \mathrm{e}^- + \bar{\nu}_e \tag{1.1}$$

$$\beta^+ : \quad (A, Z) \longrightarrow (A, Z-1) + \mathrm{e}^+ + \nu_e \tag{1.2}$$

$$EC : \quad \mathrm{e}^- + (A, Z) \longrightarrow (A, Z-1) + \nu_e \tag{1.3}$$

where A and Z are the number of nucleons and protons in the mother nucleus, respectively. The energy released in the reactions, called Q values, are given by

$$Q_{\beta^-} = M(Z)c^2 - M(Z+1)c^2 \tag{1.4}$$

$$Q_{\beta^+} = M(Z)c^2 - M(Z-1)c^2 - 2m_e c^2 \tag{1.5}$$

$$Q_{EC} = M(Z)c^2 - M(Z-1)c^2, \tag{1.6}$$

where $M(Z)$ and $M(Z-1)$ are the atomic mass of the mother and daughter nucleus, respectively, and m_e is the electron mass. The beta decay may populate excited states in the daughter nucleus (or atom) and the Q value is then reduced by the excitation energy.

Electron capture mainly occurs for nuclei close to stability, so in the case of ^{31}Ar only the β^+ decay is relevant. For that reason, we will limit the following discussion to the beta decay with a focus on the β^+ decay.

1.1.1 Fermi and Gamow-Teller decays

The weak interaction is a vector minus axial-vector (V-A) type transition, so it can be decomposed into two parts, which we, for the β^+ decay, can represent

by the following operators (if we omit the lepton operators) [Jen87]:

$$\hat{O}_V^+ = -\frac{G_F}{\sqrt{2}}\delta(\vec{r}_p - \vec{r}_n)\, T_-, \tag{1.7}$$

$$\hat{O}_A^+ = -\frac{G_F}{\sqrt{2}}\frac{g_A}{g_V}\delta(\vec{r}_p - \vec{r}_n)\, \frac{2\vec{s}}{\hbar} T_-. \tag{1.8}$$

The vector part is called the Fermi interaction and the axial vector part is called the Gamow-Teller interaction. G_F is the Fermi constant and g_V and g_A are the free vector and axial vector coupling constants. We can consider the decay to be a point interaction as seen by the δ-function. T_- is the isospin lowering operator which changes the proton ($T_3 = +\frac{1}{2}$) into a neutron ($T_3 = -\frac{1}{2}$). The operators for the β^- decay are similar, but with the isospin lowering operator T_- replaced by the isospin raising operator T_+. $\vec{s} = \frac{1}{2}\hbar\vec{\sigma}$ is the spin operator, which changes the spin of the nucleon ($\vec{\sigma}$ is a vector of the 2×2 Pauli matrices). This means that the total spin carried by the leptons is 0 for the Fermi decays and 1 for the Gamow-Teller decays, which implies that the angular momentum, J and the total isospin T of the nucleus can change by one unit in the Gamow-Teller decay, but is conserved in the Fermi decay. The nuclear parity P is conserved in both decays.

The strong interaction is charge-independent, and isospin is thus a good symmetry for the nucleus, if we neglect the charge-dependent interactions. The Fermi decay will therefore populate a single state in the daughter nucleus belonging to the same isospin multiplet as the initial state. This final state in the daughter is called the isobaric analogue state (IAS). The mass difference of the members of an isospin multiplet is only due to the difference in Coulomb energy and the mass difference between the proton and neutron. We therefore get that

$$M(Z)c^2 - M_{\mathrm{IAS}}(Z-1)c^2 = \Delta E_C + \left(M\left({}^1\mathrm{H}\right) - m_n\right)c^2, \tag{1.9}$$

where ΔE_C is the Coulomb displacement energy, m_n is the mass of the neutron and $M({}^1\mathrm{H})$ is the mass of the hydrogen atom. The hydrogen mass is used instead of the proton mass to account for the missing electron when using atomic masses. Note that the Fermi transition is only energetically possible in β^+ decays for nuclei with $N < Z$.

Isospin is not an exact symmetry and the Fermi decay will thus not only populate the IAS, but a small part (about 1–2 %) will go to other states mainly

close to the IAS, but also some with higher energies. This is due to an incomplete overlap between the initial and final wave functions and isospin mixing (together called isospin symmetry breaking). The isospin mixing is caused by the Coulomb force and entails that the IAS is not a pure isospin state. Instead it will consist of two contributions:

$$|IAS\rangle = \sqrt{1-a}\,|T\rangle + \sqrt{a}\,|T-1\rangle\,, \tag{1.10}$$

where T is the isospin of the mother nucleus. The impurities must lie close to the IAS since the mixing amplitude a (typically at most $0.1\,\%$) is inversely proportional to the energy difference. The lowest state with isospin T in the system consisting of the beta-proton daughter (e.g. ^{30}S in the case of ^{31}Ar) plus a free proton will lie above the IAS (or at most a few hundred keV below): We expect the proton separation energy for the ground state to be approximately the same as the energy needed to remove a proton from the IAS without breaking isospin, and the proton separation energies in beta-daughters are positive or small if they are negative. This means that the isospin T part of the IAS cannot decay by proton emission and the proton decay will thus go entirely through the $T-1$ part. It can be seen from the proton width (Γ_p) of the IAS, which is only about $0.1\,\%$ of the proton widths of the nearby states. This is the reason why the IAS has a longer lifetime than the nearby states, and why we would expect the gamma branching ratio of this state to be large.

Due to the strong spin-dependence of the nuclear forces there does not exist a state similar to the IAS for the Gamow-Teller decay. However, much of the Gamow-Teller strength remains in a group of collective states close to the IAS called the Gamow-Teller giant resonance (GTGR).

1.1.2 Beta strength

The intensity of the beta decay can be expressed in terms of its reduced transition probability, defined as the product of its partial half-life t (in seconds) and a dimensionless integral over the beta spectrum proportional to the decay rate, called the phase space factor f. The reduced transition probability is therefore also known as the ft value. The phase space factor depends on the charge Z of the daughter and the maximum kinetic energy of the beta particle.

It can be approximated by

$$f \approx \frac{E_\beta^5}{30\,(m_e c^2)^5}, \tag{1.11}$$

where the maximum kinetic energy of the beta is given as $E_\beta = Q_\beta - E^*$, with E^* being the excitation energy of the final state [Bla08]. This approximation is best for large E_β and low Z. A more detailed evaluation can be found in Ref. [Wil74], which we will use here for evaluating f. The approximation can be used to estimate the relative uncertainty on f as

$$\frac{\sigma_f}{f} \approx 5 \cdot \frac{\sigma\,(E_\beta))}{E_\beta} \approx 5 \cdot \frac{\sigma\,(Q_{EC})}{Q_\beta - E^*}. \tag{1.12}$$

The ft value is directly proportional to the inverse square of the nuclear overlap matrix element [Jen87], so using the operators from Eqs. (1.7)-(1.8) we get

$$ft = \frac{C}{B_F + \frac{g_A^2}{g_V^2} B_{GT}}, \tag{1.13}$$

where $B_F = |M_F|^2$ and $B_{GT} = |M_{GT}|^2$ are the reduced matrix elements squared for the Fermi and Gamow-Teller parts, respectively. They are often referred to as the strengths of the interactions. C is a constant dependent on the coupling constant. The current best-fit values of the parameters are $C = 6144.2(16)$ and $\frac{g_A}{g_V} = -1.2694(28)$ [Tow10].

Employing the relation $T_{1/2} = t \cdot b$ between the partial half-life, t, and the total half-life, $T_{1/2}$, we obtain a relation between the branching ratio, b, and the strength of the Fermi and Gamow-Teller decays, respectively:

$$B_F = \frac{C \cdot b_F}{f \cdot T_{1/2}} \tag{1.14}$$

$$B_{GT} = \left(\frac{g_A}{g_V}\right)^{-2} \frac{C \cdot b_{GT}}{f \cdot T_{1/2}}. \tag{1.15}$$

1.1.3 Sum rules

Using Eq. (1.7) and that $T_3 = \frac{Z-N}{2}$ we can derive a sum rule for the Fermi decay:

$$\sum_f |\langle f|\hat{O}_V^+|i\rangle|^2 - \sum_{f'} |\langle f'|\hat{O}_V^-|i\rangle|^2 = Z - N. \tag{1.16}$$

When only β^+ decays are allowed and if we neglect the isospin symmetry breaking, i.e. assume that the whole Fermi strength is collected in the IAS, we get that $B_F = \sum_f |\langle f|\hat{O}_V^+|i\rangle|^2 = Z - N$. A similar sum rule can be derived for the Gamow-Teller decay [Pfü12b]

$$\sum_f |\langle f|\hat{O}_A^+|i\rangle|^2 - \sum_{f'} |\langle f'|\hat{O}_A^-|i\rangle|^2 = 3(Z-N), \tag{1.17}$$

where the factor of 3 comes from the contribution from the spin-term. When calculating the Gamow-Teller strength in theoretical models the number of final states has to be limited and the theoretical B_{GT} thus needs to be scaled by a model-dependent factor q, called the quenching factor [Cau95].

1.1.4 The anti isobaric analogue state

A β^+ decay is essentially just an interchange of a proton with a neutron. Thus in some sense we can view ^{31}Ar as a core of ^{30}Cl (ground state) plus a proton (in $1d_{3/2}$), which is changed into a neutron in the β^+ decay. However, the beta decay could also happen in the core leaving the proton unchanged. If we look at it in terms of isospin eigenstates $|T\ T_3\rangle$, we can write

$$\left|^{31}\mathrm{Ar}\right\rangle = \left|\tfrac{5}{2}\ \tfrac{5}{2}\right\rangle = \left|2\,2\,,\tfrac{1}{2}\ \tfrac{1}{2}\right\rangle = \left|^{30}\mathrm{Cl} + \mathrm{p}\right\rangle. \tag{1.18}$$

When using the isospin lowering operator on this state we get the IAS. But since the operator works on both the core and the nucleon, the IAS consists of two terms:

$$\left|^{31}\mathrm{Cl}, \mathrm{IAS}\right\rangle = \left|\tfrac{5}{2}\ \tfrac{3}{2}\right\rangle = \sqrt{\frac{1}{5}}\left|2\,2\,,\tfrac{1}{2}\ {}^{-\frac{1}{2}}\right\rangle + \sqrt{\frac{4}{5}}\left|2\,1\,,\tfrac{1}{2}\ \tfrac{1}{2}\right\rangle \tag{1.19}$$

$$= \sqrt{\frac{1}{5}}\left|^{30}\mathrm{Cl} + \mathrm{n}\right\rangle + \sqrt{\frac{4}{5}}\left|^{30}\mathrm{S}^* + \mathrm{p}\right\rangle. \tag{1.20}$$

This state has an othogonal state consisting of the same two configurations, but with different weights:

$$\left|^{31}\mathrm{Cl}, \mathrm{AIAS}\right\rangle = \left|\tfrac{3}{2}\ \tfrac{3}{2}\right\rangle = \sqrt{\frac{4}{5}}\left|2\,2\,,\tfrac{1}{2}\ {}^{-\frac{1}{2}}\right\rangle - \sqrt{\frac{1}{5}}\left|2\,1\,,\tfrac{1}{2}\ \tfrac{1}{2}\right\rangle \tag{1.21}$$

$$= \sqrt{\frac{4}{5}}\left|^{30}\mathrm{Cl} + \mathrm{n}\right\rangle - \sqrt{\frac{1}{5}}\left|^{30}\mathrm{S}^* + \mathrm{p}\right\rangle, \tag{1.22}$$

where AIAS is the anti isobaric analogue state which lies below the IAS. Note that since the isospin lowering operator (and thus the Fermi operator) only changes the isospin of the state, the spin and parity of the core is unchanged. In this energy region the main gamma decay of the IAS is normally M1 transitions (defined in Section 1.3). The spin part of the M1 operator is very similar to the Gamow-Teller operator [Wil69] and the main gamma decays from the IAS will thus populate the same states as the Gamow-Teller decays of the mother nucleus. A more detailed description of the AIAS and the gamma decay of the IAS can be found in Ref. [Wil69].

1.2 Beta-delayed particle emission

- an effect of the strong interaction

When approaching the drip-line the energy window for beta-decay increases while the binding energy of the least bound nucleons decreases. It thus becomes more feasible for the states fed in the beta-decay to decay by particle emission. Naturally, the number of open channels (decay types, which are energetically allowed) increase the closer we get to the drip-line. The most exotic decay modes observed so far are the beta-delayed three-proton decay on the proton rich side of stability and the beta-delayed four-neutron decay on the neutron rich side.

Multi-particle emission is of great interest, since the mechanism of the breakup is not fully determined by energy and momentum conservation. For a three-body breakup (for example two-proton emission) there are two possible mechanisms: Either the breakup can happen in two steps (the two protons are emitted one by one), which is referred to as a sequential breakup, or it can break up directly into the three body continuum (the two protons are emitted simultaneously), referred to as a direct or simultaneous breakup. The four- or five body breakups (as the three-proton or four-neutron emissions) can be either fully sequential, fully simultaneous or partly sequential and simultaneous. The process is determined by the structure of the decaying state and the barrier and the width of the resonances in the subsystem(s).

A consequence of the large fragmentation of the decay of the nuclei close to the drip-line is a complication of extracting and assigning the beta strength.

To do this we need to have detailed information on all the possible channels, which we can obtain by detecting the emitted particles and possible gamma rays with high resolution and efficiency. This is most easily obtained for proton rich nuclei, since the emitted particles carry charge. Another benefit of studying the proton rich side is that the majority of the strength is accessible in the beta decay.

Finally, it is possible to use beta-delayed particle emission to study the structure of the nuclei involved. Again we need to detect the emitted particles and possible gamma rays with a high resolution. However, this makes it possible to determine the energy spectra of the nuclei and for the intermediate levels we can determine which decay channels are open and their corresponding branching ratios. Furthermore, for the proton rich nuclei it is also possible to extract the spin of intermediate levels as shown in Section 6.3. These features are also studied in reaction experiments, but the selection-rules of the beta-decay provides a selectivity, which means that the populated states can be studied with a much lower background. For example, at high energies (where the IAS is normally situated) the density of states is very large and it is thus here significantly easier to separate and identify the populated states in beta decay experiments. A detailed review of beta-delayed particle emission can be found in Refs. [Pfü12b, Bla08].

1.2.1 Q-values for multi-nucleon emission

For emission of i nucleons (N), where N can be either protons (p) or neutrons (n), the Q-value can be found solely from energy and momentum conservation as

$$Q_{iN} = E_r + \sum_{j=1}^{i} E_j = \frac{\vec{p}_r^{\,2}}{2M_r} + \sum_{j=1}^{i} \frac{\vec{p}_j^{\,2}}{2m_N}, \tag{1.23}$$

$$\vec{0} = \vec{p}_r + \sum_{j=1}^{i} \vec{p}_j, \tag{1.24}$$

where E_j and $\vec{p}_j$ are the energy and momentum of the j^{th} nucleon. m_N is the mass of the nucleon, while E_r, $\vec{p}_r$ and M_r are the energy, momentum and mass

of the recoiling nucleus, respectively. For two-proton emission this reduces to

$$Q_{2p} = E_1 + E_2 + \frac{m_p}{M_r}\left(E_1 + E_2 + 2\sqrt{E_1 E_2}\cos\Theta_{2p}\right), \tag{1.25}$$

where Θ_{2p} is the angle between the two protons given by

$$\cos\Theta_{2p} = \frac{\vec{p}_1 \cdot \vec{p}_2}{|\vec{p}_1||\vec{p}_2|} = \frac{1}{|\vec{p}_1||\vec{p}_2|}\left(p_{1_x}p_{2_x} + p_{1_y}p_{2_y} + p_{1_z}p_{2_z}\right). \tag{1.26}$$

Note that these formula are all independent of the mechanism of the emission.

1.2.2 Mechanism of sequential two-proton emission

The sequential two-proton decay can be used to study the intermediate levels. In the following we will for simplicity use the decay of ^{31}Ar as an example, but the derived formula are generally applicable for the two proton emission. In the decay of ^{31}Ar the two-proton emitting state is an excited state of ^{31}Cl. In the rest frame of ^{31}Cl the energy of the first emitted proton is given by

$$E_1 = \frac{M(^{30}\mathrm{S})}{M(^{30}\mathrm{S}) + m_p} Q_1, \tag{1.27}$$

where $M(^{30}\mathrm{S})$ are the mass of ^{30}S and Q_1 is the total energy released in the emission:

$$Q_1 = E(^{31}\mathrm{Cl}) - E(^{30}\mathrm{S}) - S_{p1}. \tag{1.28}$$

$E(^{31}\mathrm{Cl})$ and $E(^{30}\mathrm{S})$ are the excitation energies of ^{31}Cl and ^{30}S respectively, and S_{p1} is the proton separation energy of ^{31}Cl. Equivalently to this, the energy of the second emitted proton in the rest frame of the recoiling one-proton daughter ^{30}S can be found as

$$E_2' = \frac{M(^{29}\mathrm{P})}{M(^{29}\mathrm{P}) + m_p} Q_2 \tag{1.29}$$

$$Q_2 = E(^{30}\mathrm{S}) - E(^{29}\mathrm{P}) - S_{p2}, \tag{1.30}$$

where $M\left(^{29}\mathrm{P}\right)$ and $E\left(^{29}\mathrm{P}\right)$ are the mass and energy of the two-proton daughter ^{29}P and S_{p2} is the proton separation energy of ^{30}S. The energy of the second emitted proton in the rest frame of the emitter ^{31}Cl is obtained by a Galilei transformation:

$$E_2 = E_2' + \left(\frac{m_p}{M(^{30}\mathrm{S})}\right)^2 E_1 - 2\frac{m_p}{M(^{30}\mathrm{S})}\sqrt{E_1 E_2'}\cos\Theta_{2p}. \tag{1.31}$$

Rearranging (1.30) and combining with (1.27) gives

$$E(^{30}\mathrm{S}) = Q_{2p} + E(^{29}\mathrm{P}) - \frac{M(^{30}\mathrm{S}) + m_p}{M(^{30}\mathrm{S})} E_1 + S_{p2}, \tag{1.32}$$

where $Q_{2p} = Q_1 + Q_2$ and can be found by (1.25).

1.3 Gamma decay

- an effect of the electromagnetic interaction

Gamma rays are electromagnetic radiation emitted when an excited nucleus decays to a lower energy state. Gamma decays normally occur from states below the threshold for particle emission, since particle emission is favoured due to the strong interaction being much stronger than the electromagnetic interaction. However, gamma decays can also occur from states where particle emission is retarded by the Coulomb or angular momentum barriers or by selection rules.

The electromagnetic field can be expanded in multipoles (see Ref. [Jac98]), where each term can be classified according to its total angular momentum ℓ and parity. The possible multipolarities in a transition are determined by conservation of angular momentum and parity. The order of the multipole is given by 2^ℓ and the parity is split into two types: electric with parity $(-1)^\ell$ and magnetic with parity $(-1)^{\ell+1}$. The transitions are normally denoted $E\ell$ and $M\ell$, respectively. The monopole term is zero, due to conservation of charge, so the $0^+ \rightarrow 0^+$ gamma transition is not allowed. Conservation of angular momentum requires

$$|J_i - J_f| \leq \ell \leq J_i + J_f, \tag{1.33}$$

where J_i and J_f are the spin of the initial and final state, respectively. The transition rate in semi classical theory is given by [Jen87]

$$\lambda_{\mathrm{EM}}(\ell) = \frac{8\pi(\ell+1)}{\hbar\ell[(2\ell+1)!!]^2} \left(\frac{E_\gamma}{\hbar c}\right)^{2\ell+1} B_{\mathrm{EM}}(\ell), \tag{1.34}$$

where $(2\ell+1)!!$ is the double factorial of $2\ell+1$ defined as the product of all uneven integers from 1 to $2\ell+1$. E_γ is the photon energy and the function

$B_{\mathrm{EM}}(\ell)$ is the reduced transition strength, which contains all the nuclear information. Essentially it is just the squared matrix element of the operator causing the transition and producing the photons. The function is different for the two types of transitions and smallest for the magnetic multipoles. The transition rate decreases rapidly with increasing ℓ, so the gamma emission is dominated by the lowest allowed multipolarity.

1.3.1 Doppler broadening of gamma-lines

Gamma decays that occur just after a proton decay (as the case for the gamma transitions in ^{30}S in the decay of ^{31}Ar), will be emitted from a moving nucleus, since the nucleus will recoil after the proton decay to conserve momentum. A gamma ray emitted from a nucleus moving with a velocity $\vec{v}$ in an angle θ will be Doppler shifted according to the formula:

$$\cos\theta = \frac{E - E_0}{E_0}\frac{c}{v}, \tag{1.35}$$

where E_0 is the initial energy and E is the measured energy. Again we use the decay of ^{31}Ar as an example, but the derived formula are generally applicable. If the gamma ray is emitted instantaneously after the first proton, i.e. assuming that the momentum of ^{30}S is the same as the emitted proton but in opposite direction, then we can find the energy of the gamma ray as

$$E_0 = E \cdot \left(1 - \frac{\sqrt{2E_p m_p c^2}}{M(^{30}\mathrm{S})\,c^2}\cos\theta\right)^{-1}, \tag{1.36}$$

where E_p is the energy of the emitted proton. However, the levels populated in ^{30}S do not decay instantaneously. This means that ^{30}S will have been slowed down or perhaps stopped entirely before the gamma ray is emitted, depending on the life-time of the level and the stopping power of the nucleus in the material. Details on this process can be found in Ref. [Fyn03], which shows us that the Doppler width of a gamma-line with energy E_γ is

$$\Delta E_\gamma = 2E_\gamma\sqrt{\frac{2E_p m_p c^2}{\left(M(^{30}\mathrm{S})\,c^2\right)^2}}. \tag{1.37}$$

CHAPTER 2

The interesting properties of ^{31}Ar

2.1 The history of the ^{31}Ar research

The first interest in ^{31}Ar was due to the possible ground state two-proton decay to the ground state of ^{29}S. ^{31}Ar is the last of the argon isotopes that is one-proton stable, but at the time of the first experiments in the 1980s the two-proton separation energy was predicted to be $-233(206)\,\mathrm{keV}$, and it was thus thought that this decay mode, originally predicted by Goldansky [Gol60, Gol61], might exist for ^{31}Ar. However, even though the decay of ^{31}Ar was intensively studied at both GANIL [Bor87b, Bor91], Berkeley [Rei89] and ISOLDE [Bor90] it was not possible to detect any two-proton radioactivity. The current mass measurements indicate that the two-proton separation energy of ^{31}Ar is $130(210)\,\mathrm{keV}$, which makes a ground state two-proton decay very unlikely.

Even though the first experiments were unsuccessful in their original goal, they did provide the first information of what turned out to be a very fragmented beta-delayed proton decay of ^{31}Ar. From comparisons with the decays of ^{32}Ar [Bjö85] and ^{33}Ar [Bor87a] one would expect the decay of the isobaric analogue state (IAS) to dominate the proton spectrum for ^{31}Ar, since their proton spectra are completely dominated by the proton decay of the IAS to the ground state in sulphur. However, contrary to ^{32}Ar and ^{33}Ar, the IAS in ^{31}Ar lies well above the two-proton threshold so it mainly decays via two-proton emission. Even in the summed proton spectrum, this decay is only just visible [Bor90, Bor91]. Instead the proton spectrum is dominated by ground state proton decays of lower states in ^{31}Cl (see Section 5.1), which shows that the beta-decay is much more fragmented than first anticipated.

The first remeasurement of the ^{31}Ar decay was preformed at GANIL in 1992 [Baz92], where the setup was optimised for multi-particle detection. Here the main beta-delayed one- and two-proton branches were confirmed and a large beta-delayed three-proton branch of $2.1(10)\,\%$ was observed. However, this signal was later shown to originate from a beta-delayed two-proton branch [Fyn99]. The real beta-delayed three proton decay of ^{31}Ar was discovered only a few years ago by an experiment performed at GSI with an Optical Time Projection Chamber (OTPC) [Pfü12a, Lis15] and they measured a branching ratio of $0.07(2)\,\%$. The beta-delayed three proton decay is the most exotic decay mode on the proton rich side of stability, and it has only been seen in two other nuclei so far: ^{45}Fe [Mie07] and ^{43}Cr [Pom11, Aud12b]. It was also observed in the experiment presented here, which was performed at ISOLDE in 2009, making the first spectroscopic analysis of this decay mode possible, see Chapter 7.

Two further experiments were made at ISOLDE in 1995 and 1997 where the focus was to study the mechanism of the beta-delayed two-proton decay and to extract the beta strength distribution. It was shown by the latter experiment that the decay was dominated by sequential decays [Fyn00] as the results from the first experiment were inconclusive [Axe98b]. However, a (suppressed) simultaneous decay branch still remains possible originating from levels just above the two-proton threshold in ^{31}Cl, which are relatively strongly fed in the beta decay of ^{31}Ar. This was one of the original motivations for the IS476 experiment presented in this thesis [Fyn08]. This part has yet to be fully analysed, but a preliminary analysis showed no sign of a simultaneous decay branch [Kol09].

A complete analysis was made of the beta-delayed one- and two-proton decay including proton delayed gamma rays in both ^{29}P and ^{30}S from the 1995 and 1997 ISOLDE experiments [Axe98a, Fyn00]. This made it possible to extract most of the Fermi and Gamow-Teller strengths of the beta-decay. The newly discovered three-proton branch suggests that more of the strength goes through higher lying levels in ^{29}P than anticipated when these experiments were analysed, see Section 7.2. The disclosure of the three-proton branch and the population of the higher levels in ^{29}P make it possible to perform a better determination of the beta-strengths as presented in Chapter 8.

The sequential nature of the beta-delayed two-proton decay made it pos-

sible to deduce the energies of the levels in ^{30}S above the proton threshold. The levels just above the proton threshold are relevant to nuclear astrophysics and a detailed analysis of these was the other main motivation for the IS476 experimen [Fyn08]. However, it turned out to be possible to extract much more information about these levels from the decay of ^{31}Ar than anticipated and our results have proven competitive with reaction experiments, see Chapter 6.

2.2 The beta-proton daughter ^{30}S and astrophysics

2.2.1 The silicon isotopic abundance ratios in presolar grains

By studying presolar dust grains preserved in meteorites it is possible to study stellar processes. The dust grains are created in stellar winds and outflows before the solar system was formed so their composition can constrain the current models of stellar structure and nucleosynthesis. The most extensively studied grains are SiC since they are relatively abundant. A small fraction of these have been suggested to originate from classical novae [Ama01, Nit05] and are characterised by low $^{12}\mathrm{C}/^{13}\mathrm{C}$ and $^{14}\mathrm{N}/^{15}\mathrm{N}$ ratios, high $^{30}\mathrm{Si}/^{28}\mathrm{Si}$ ratios and $^{29}\mathrm{Si}/^{28}\mathrm{Si}$ ratios close to or lower than terrestrial. Classical novae are stellar explosions that occur in close binary systems consisting of a main sequence star and a white dwarf. Hydrogen rich matter is accreted from the main-sequence star to the surface of the white dwarf where it ignites. As the hydrogen fuses to helium the temperature increases. Eventually, when the nuclear burning is dominated by explosive hydrogen burning via the hot CNO cycles[1], a thermonuclear runaway sets in near the base of the accreted layers. Finally an explosion occurs sending up to 10^{-4} solar masses ($M_{\odot}$) worth of material away with ejection velocities of around $10^3\,\mathrm{km/s}$ [Ili07]. In the ejecta large amounts of matter from the white dwarf itself is present which could explain why these objects do not reach the Chandrasekhar limit[2] and explode as type Ia supernovae.

[1] A CNO cycle is a hydrogen burning cycle between carbon, nitrogen and oxygen creating helium.

[2] The Chandrasekhar limit is the mass where the electron degeneracy pressure in the core of the star becomes insufficient to balance the gravitational attraction from the star itself. The value is $1.44M_{\odot}$.

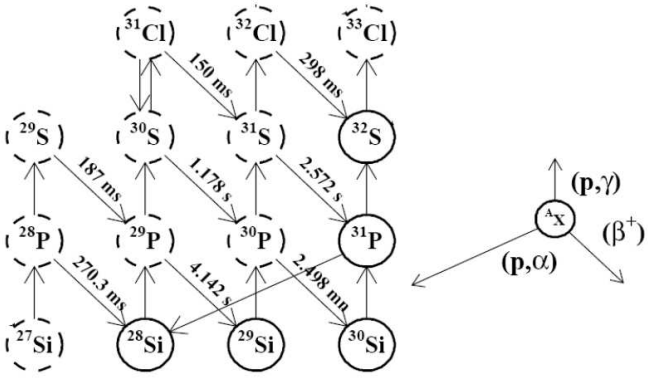

Figure 2.1: The main nuclear reaction paths in the region of interest for the abundances of ^{29}Si and ^{30}Si produced by ONe nova. It has been adopted from Ref. [Jos01] and the numbers shown are the half-lifes known at the time. The half-life of ^{30}S has recently been measured to be $1175.9(17)\,\mathrm{ms}$ [Sou11].

The silicon isotopic abundance can provide information on the temperatures attained in the explosion and the dominant nuclear-synthetic paths followed by the thermonuclear runaway [Jos04]. In order to understand the origin of the observed isotopic ratios, the processes that create and destroy the different silicon isotopes have to be well understood. One of the most important processes is the $^{29}\mathrm{P}(p,\gamma)^{30}\mathrm{S}$ reaction. The main nuclear reaction paths in the region for interest of an Oxygen-Neon (ONe) nova is shown in Figure 2.1. From this figure it is clear that if the $^{29}\mathrm{P}(p,\gamma)^{30}\mathrm{S}$ reaction is faster than the β^+ decay of ^{29}P, the amount of ^{30}Si would increase and the amount of ^{29}Si decrease. Iliadis *et al*. [Ili02] showed that the abundances of ^{29}Si and ^{30}Si are very sensitive to the uncertainty in the $^{29}\mathrm{P}(p,\gamma)^{30}\mathrm{S}$ reaction rate. This makes it important to determine the level structure of ^{30}S just over the proton threshold as well as the proton and gamma branching ratios for these levels.

2.2.2 The rp-process in type I X-ray bursts

The $^{29}\mathrm{P}(p,\gamma)^{30}\mathrm{S}$ reaction rate, and by extension the level structure of ^{30}S, is also important for understanding type I X-ray bursts [Sch11]. Type I X-ray bursts occur in close binary systems consisting of a neutron star with a strong

magnetic field and a massive population I star ($M \gtrsim 5M_{\odot}$). They are fuelled by explosive burning of the accreted matter on the surface of the neutron star. These bursts are the most frequent type of thermonuclear stellar explosions in the galaxy. The accreted matter consists mainly of ionised hydrogen and helium and it is compressed in a thin electron degenerate shell in which hydrogen can fuse into helium via the hot CNO cycles. When the accretion rate is high a breakout from the hot CNO cycles can occur, which is followed by a sequence of rapid proton captures and β^+ decays. This process is called rapid proton capture and referred to as the rp-process. The path of the rp-process is defined by the competition between β^+ decays and proton captures and decays. The nucleus will continue to absorb protons via a (p,γ) reaction and thus move toward the drip-line until it becomes more feasible to decay by β^+ emission. This will either happen if the rate for beta emission is larger than the rate of the (p,γ) reaction or if the rate of the (p,γ) reaction is smaller than the reverse photodisintegration rate. In the latter case the nucleus has to wait for the β^+ decay. If the lifetime of such an isotope is long it will cause a bottleneck in the reaction flow and the isotope is called a waiting point nucleus. The time scale of the explosion is mainly determined by a handful of these waiting point nuclei. Due to the long half-life of ^{30}S of $1175.9(17)\,\mathrm{ms}$ [Sou11] and its very low $Q_{p\gamma}$ value of $282.8(44)\,\mathrm{keV}$ [Saa11] ^{30}S is a key waiting point in the rp-process influencing the time scale of the explosion, the structure of the resulting light distribution and the energy generation of the burst [Fis04, Fis08].

2.2.3 The current status of the ^{30}S research

The range of energies, where the $^{29}\mathrm{P}(p,\gamma)^{30}\mathrm{S}$ reaction can occur, is known as the Gamow window. For the temperatures relevant to astrophysics it spans $100\,\mathrm{keV}$ to $1100\,\mathrm{keV}$. The proton separation energy of ^{30}S is $4395.6(7)\,\mathrm{keV}$ [Wan12] and the levels in ^{30}S interesting for astrophysics thus lie below $6\,\mathrm{MeV}$. These levels are all narrow and the $^{29}\mathrm{P}(p,\gamma)^{30}\mathrm{S}$ reaction rate through one of these levels just above the proton threshold is given by [Ili07]

$$N_A \langle \sigma v \rangle_r = N_A \left(\frac{2\pi}{\mu kT} \right)^{3/2} \hbar^2 (\omega\gamma)_r e^{-E_r/kT}. \tag{2.1}$$

The subscript r specifies that it belongs to a level or resonance with energy E_r and $\langle \sigma v \rangle$ denotes the thermally averaged cross section. μ is the reduced mass

and the resonance strength $(\omega\gamma)_r$ is given by

$$(\omega\gamma)_r = \frac{(2J_r+1)}{(2J_a+1)(2J_b+1)}\left(\frac{\Gamma_p\Gamma_\gamma}{\Gamma}\right)_r, \tag{2.2}$$

where J_r is the spin of the resonance, J_a and J_b are the spins of the original particles (in this case the proton and ^{29}P), and Γ_p and Γ_γ are the proton and gamma partial widths of the level with total width $\Gamma = \Gamma_p + \Gamma_\gamma$. The total reaction rate is the sum over the relevant resonances r of (2.1).

liadis *et al.* [Ili01] predicted that the reaction rate of the $^{29}\mathrm{P}(p,\gamma)^{30}\mathrm{S}$ reaction was dominated by two resonances in ^{30}S with spins 3^+ and 2^+ and excitation energies of $4733(40)\,\mathrm{keV}$ and $4888(40)\,\mathrm{keV}$, respectively. The literature list both as unobserved at that time and acknowledge the $^{32}\mathrm{S}(p,t)^{30}\mathrm{S}$ reaction experiments by Bardayan *et al.* [Bar07] and Setoodehnia *et al.* [Set10] for the first observation of the 3^+ and 2^+ state, respectively. However, a level at $4.85(6)\,\mathrm{MeV}$ was observed already in 1990 in the decay of ^{31}Ar [Bor90]. Table 2.1 shows the results of all the experiments from the last two decades, which focused on the low-lying levels of ^{30}S just above the proton threshold. It is not clear how the uncertainties are extracted in the measurements by Lotay *et al.*, but from the measured gamma lines it seems as though the uncertainty on the calibration is not included. The uncertainties on the energies measured by Fynbo *et al.* do not include the uncertainty on the calibration. Furthermore, the effect of the detector dead layers (see Section 3.3) was not included, which implies that the extracted energies for the levels just above the proton threshold are underestimated as discussed in Section 6.1. It should also be noted that the $5168(6)$-keV level measured by Bardayan *et al.* is an unresolved doublet consisting of a 0^+ and a 4^+ level. Lotay *et al.* assigns this to represent the 0^+ level, since the level measured at $5132\,\mathrm{keV}$ is found to be spin 4^+. However, it should be stressed that the energy of the 0^+ state is not $5168\,\mathrm{keV}$, since this energy is the mixture of both the 0^+ and the 4^+ level. There is still some disagreement about the assignment of the spin of the levels in this energy region as can be seen from Table 2.1. The spin assignments are only tentatively made from comparisons with the spin assignment of the mirror nucleus ^{30}Si. Figure 2.2 thus summarises what is known today about ^{30}S and ^{30}Si.

From Eqs. (2.1)-(2.2) we see that the reaction rate is calculated using the energy, spin, and the proton and gamma partial width of the relevant resonances. The improvements on the energies of the 3^+ and 2^+ levels have

reduced the uncertainties of the $^{29}\mathrm{P}(p,\gamma)^{30}\mathrm{S}$ reaction rate significantly for the relevant temperatures. Calculations made by Setoodehnia *et al.* [Set13] and by Richter and Brown [Ric13] show that the uncertainties are now so small that they no longer significantly influence the silicon abundances. These calculations, however, use proton and gamma partial widths, which are calculated based on the shell model and comparisons with the mirror nucleus. Experimental values for these would clearly be preferred. In Section 6.2 we present the first experimental limits on the ratio between the proton and gamma partial widths.

Table 2.1: Energy and spin of the ^{30}S levels below $6\,\mathrm{MeV}$ for experiments from the last two decades focusing on the levels just above the proton threshold. The proton separation energy of ^{30}S is $4395.6(7)\,\mathrm{keV}$ [Wan12].

[Fyn00]	[Bar07]		[Set10, Set11, Set13]			[Lot12]		[Alm12]	
$^{31}\mathrm{Ar}(\beta 2p)$	$^{32}\mathrm{S}(p,t)^{30}\mathrm{S}$		$^{28}\mathrm{Si}(^{3}\mathrm{He},n\gamma)^{30}\mathrm{S}$	$^{32}\mathrm{S}(p,t)^{30}\mathrm{S}$		$^{28}\mathrm{Si}(^{3}\mathrm{He},n\gamma)^{30}\mathrm{S}$		$^{32}\mathrm{S}(p,t)^{30}\mathrm{S}$	$^{28}\mathrm{Si}(^{3}\mathrm{He},n)^{30}\mathrm{S}$
E_x (keV)	E_x (keV)	J^π	E_x (keV)	E_x (keV)	J^π	E_x (keV)	J^π	E_x (keV)	E_x (keV)
	g.s.	0^+	g.s.		0^+	g.s.	0^+	g.s.	g.s.
	2010.7	2^+	2210.7(3)	2208(3)	2^+	2210.1(1)	2^+	2208.5(22)	2200(210)
	3402.6	2^+	3404.7(3)		2^+	3404.1(1)	2^+	3405.8(12)	
			3667.2(4)		0^+	3668.0(4)	0^+	3677.3(70)	3600(260)
	3680(6)	1^+	3676.9(4)	3681(3)	1^+	3677.1(4)	1^+		
	4704(5)	3^+	4688.1(4)	4688(2)	3^+	4687.6(2)	3^+	4682.5(57)	
			4809.8(5)	4812(2)	2^+	4808.7(3)	2^+		
	5168(6)	$4^+ + 0^+$	5132.3(5)		(4^+)	5132.1(1)	4^+	5130.0(18)	
5217.4(7)				5225(2)	(0^+)	5218.8(3)	3^+	5217.8(28)	5200(44)
				5315(2)	(3^-)		(3^-)	5312.1(20)	
5389(2)	5383(8)	$3^-, 2^+$		5393(2)	3^+		(2^+)	5382.0(7)	5400(43)
5842(4)				5849(2)	(2^+)	5848.0(4)	4^+	5835.5(13)	
				[5947(2)]	(4^+)				

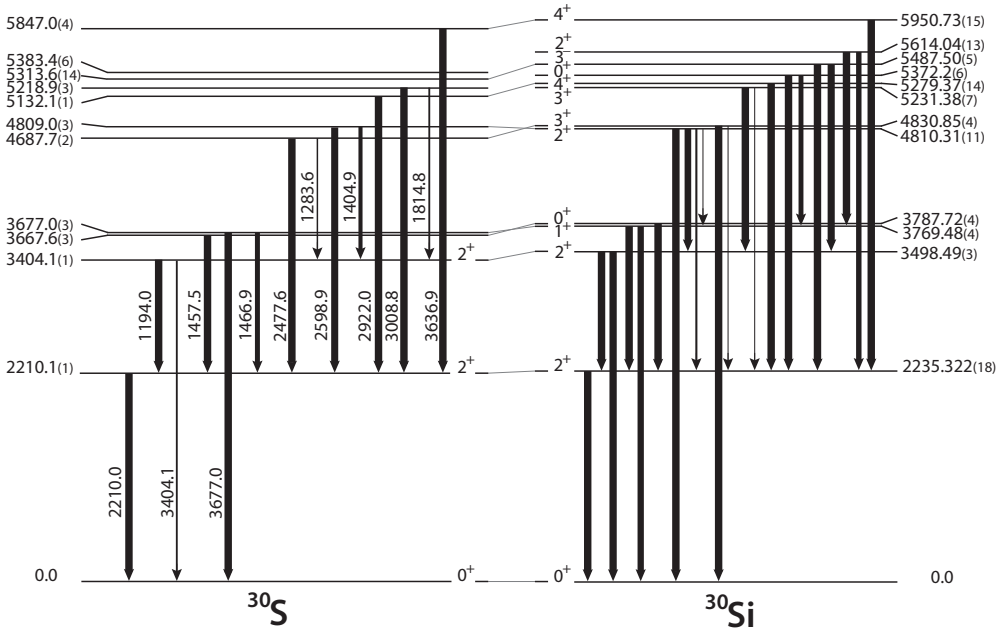

Figure 2.2: The level scheme of ^{30}S below $6\,\mathrm{MeV}$ and of its mirror nucleus ^{30}Si. The energies of ^{30}S are a weighted average of the energies listed in Table 2.1 while the energies of ^{30}Si are from Ref. [Bas10]. The observed gamma transitions are marked by arrows scaled in size to match the intensities. The most dominant transition from each level corresponds to an intensity of 1 [Bas10, Set13, Lot12]. For states above $5\,\mathrm{MeV}$ in ^{30}Si, only transitions having a strength of minimum $10\,\%$ of the main transition are included. The spins listed are measured spins. The spin of the remaining ^{30}S levels have been tentatively assigned by comparison with ^{30}Si, these are shown with grey lines where the assignment is unambiguous. The proton separation energy for ^{30}S is $4395.6(7)\,\mathrm{keV}$ [Wan12] and the resonances above this energy are thus proton unbound. The corresponding levels in ^{30}Si are not particle unbound and therefore decay only by gamma emission.

CHAPTER 3

The Experiment

As described in the previous chapters a number of things are important when studying the decay of ^{31}Ar. First of all it is essential that the setup used offers a large angular coverage for detection of both protons and gamma rays, to ensure that all particles in the decay can be measured with a high efficiency. Furthermore, the detectors should have a good energy and angular resolution. Finally, it is of course crucial to be able to study a large number of ^{31}Ar decays with as little background as possible. The ISOLDE facility at CERN, Geneva are able to produce a high-yield ^{31}Ar beam, which is why most of the ^{31}Ar decay studies have been performed here. The experimental data presented in this thesis originate from an ^{31}Ar experiment carried out in August 2009 at the ISOLDE facility at CERN, Geneva.

3.1 Beam production at ISOLDE

ISOLDE is, as implied by the name, an ISOL (Isotope Separator On-Line) facility used for production and separation of radioactive nuclear isotopes. An overview of the facility is shown in Figure 3.1. ISOLDE receives a $1.4\,\mathrm{GeV}$ pulsed proton beam from the CERN PS Booster, which is directed to one of the two target stations and aimed at a thick primary target kept at a high voltage of $60\,\mathrm{kV}$. A variety of nuclei are then produced by fragmentation or spallation and evaporate through the target to the transfer line. The evaporation is normally made faster by heating the targets to temperatures between $700\,^{\circ}\mathrm{C}$ and $2500\,^{\circ}\mathrm{C}$. The nuclei are ionised (positively) in the transfer line using surface, plasma or laser ionisation depending on the requested element. The beam line is kept at ground potential to accelerate the ionised nuclei through a mass separator. There are two separators, the High Resolution Separator (HRS) and the General Purpose Separator (GPS), each connected to one of the target stations. They separate the nuclei according to their masses using a series

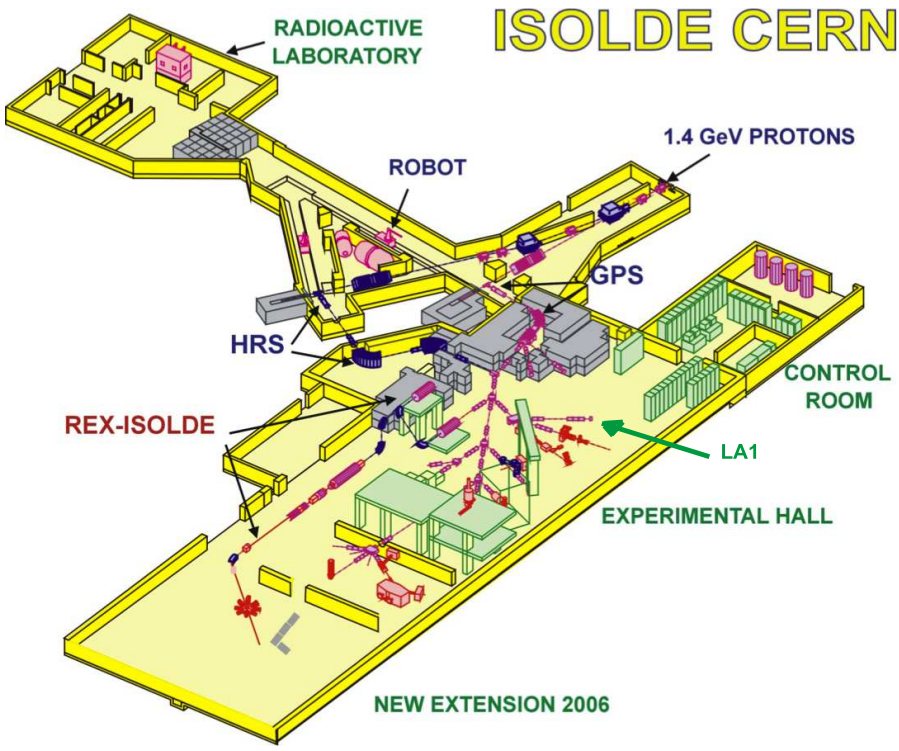

Figure 3.1: A schematic view of the ISOLDE hall. The facility is divided into three parts: The radioactive laboratory (top left), the target area (middle top) and the experimental hall. The target area houses the two target stations and corresponding mass separators (GPS and HRS) and is shielded from the radioactive laboratory and the experimental hall by massive concrete walls (the grey parts). The beam lines from the separators run to the different experiments located in the experimental hall. The experiment described in this thesis was performed at LA1 (marked by a green arrow).

of bending magnets, one for GPS and two for HRS. The final beam is then guided by means of electrostatic deflectors to the detector setup.

For the production of ^{31}Ar, a powder CaO target was used with a versatile arc discharge plasma ion source [Pen10]. The 60-keV ion beam was guided through the GPS to separate the desired argon isotopes. However, a significant contamination of nitrogen isotopes was present during the experiment, which also included runs with ^{32,33}Ar. In the case of ^{31}Ar the contamination consisted of ^{16,17}N, which were present in the beam as N_2 (^{15}N^{16}N or ^{14}N^{17}N) and N_2H (^{14}N^{16}N^{1}H). This contamination have been analysed in detail and can be found in Ref. [Kus11]. Due to technical problems the target heating was switched off half way during the experiment. This did not change the yield of ^{31}Ar significantly, while the yield of the nitrogen contamination was considerably reduced. The target heating was thus kept off for the remaining part of the experiment. In the case of ^{31}Ar there was also a substantial amount of contamination from ^{15}C, which together with the nitrogen contamination is used to improve the gamma calibration. An average ^{31}Ar yield of approximately 1 ion per second during the runs was obtained for a total run time of seven days.

3.2 Detector setup

The detector setup consisted of a silicon cube detector [Mat09] containing six double-sided silicon strip detectors (DSSSDs) in a cube formation, see Figure 3.2. The DSSSDs are segmented into 16 strips in the front and in the back, each $3\,\mathrm{mm}$ wide and $0.1\,\mathrm{mm}$ apart. For this experiment we used one detector with a thickness of $69\,\mu\mathrm{m}$ with a 100-nm dead layer (no. 1), one detector with a thickness of $494\,\mu\mathrm{m}$ and 800-nm dead layer (no. 5) and four detectors with thickness close to $300\,\mu\mathrm{m}$; three with a 800-nm dead layer (nos. 2, 3, 4) and one with a 100-nm dead layer (no. 6). For backing behind four of the detectors (nos. 1, 2, 3, 6) 1500-$\mu\mathrm{m}$ thick 50×50-mm unsegmented silicon pad detectors were used. The beam enters between detectors 5 and 6 and is stopped in a $50\,\mu\mathrm{g/cm^2}$ carbon foil mounted on a small metal holder entering between detectors 3 and 5. Two MINIBALL germanium cluster detectors [War13] were situated outside the cube chamber behind detectors 3 and 4. Each MINIBALL

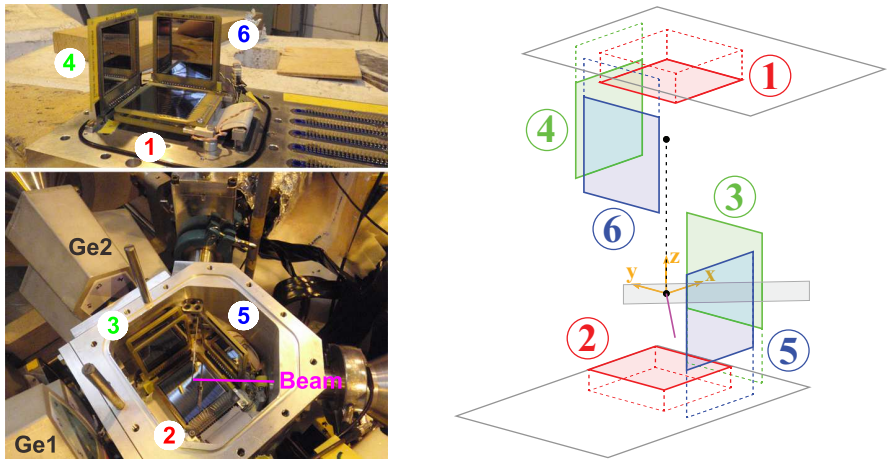

Figure 3.2: The experimental setup used for the experiment. **Left:** A picture of the setup with the cube opened. The lid is shown above with three of the detectors mounted. The beam enters between detectors 5 and 6 and is implemented in a thin foil mounted on a target latter entering between detectors 3 and 5. **Right:** A schematic view of the setup. The top of the cube is lifted with three of the DSSSDs, following the dotted line, for better visualisation on the bottom drawing. The coordinate system used for the analysis is shown. It is placed at the center of the beam spot with the z axis pointing towards detector 1, the x axis pointing towards detector 3 and the y axis pointing towards detector 4.

cluster consists of three crystals, but unfortunately one of the crystals of the cluster behind DSSSD 3 gave no signal.

3.3 Energy loss calculations

Particles travelling through matter lose energy. An understanding of this energy loss is important when reconstructing the initial energy of particles detected in an experiment. We can divide the particles into three groups: uncharged particles (such as gamma-rays), light charged particles (beta particles) and heavier charged particles (here protons and alpha particles).

Gamma rays lose energy by interacting with the material through electromagnetic interactions such as the photoelectric effect, Compton scattering and pair production. All energy will be lost in just a few interactions. The interac-

tion cross section is very small so the total energy absorption of a gamma ray requires a large volume. Since the energy from a gamma ray is not necessarily deposited in a single interaction, some of the energy can escape the detector. For a MINIBALL germanium detector, which consists of three crystals situated directly next to each other, this means that an incoming gamma ray can cause a signal in more than one crystal. Due to the limited angular coverage of the detectors, the probability of having multiple gamma rays in an event in the same cluster is very small. We can thus remove all gamma events with signals in neighbouring crystals with no significant loss of statistics.

Charged particles lose their energy by multiple interactions with the electrons and nuclei of the material. In contrast to gamma rays, the interaction cross section is very high and the charged particles lose their energy by many successive interactions that gradually decrees the energy. The scatterings cause beta particles to be spread in a detector due to their small mass, while heavier charged particles will only deviate a little from their incoming trajectories. In a DSSSD this means that a proton or alpha particle will deposit energy in only one pixel (unless it enters close to the edge) while a beta particle will deposit energy in multiple pixels. Furthermore, since the interaction cross section increases as the energy of the charged particle decreases, high energy beta particles will only deposit a small amount of their energy in the DSSSD and then the remaining in the pad detector (if this is sufficiently thick).

The energy deposited in a detector will not be equal to the energy of the emitted particle, since the energy loss is gradual and the particle will lose energy travelling out of the target and through the dead layer(s) of the detector(s). This effect needs to be taken into account. Since the process is stochastic a formula is not easily derived and instead we use the code `SRIM` (Stopping and Range of Ions in Matter) [Zie83]. `SRIM` is a Monte Carlo simulation that uses the binary collision approximation, in which the incoming ion is assumed to travel through the material having several independent binary collisions with the nuclei of the material. In between these collisions the ion is assumed to travel in straight lines experiencing electronic stopping power. As an input `SRIM` takes the incoming ion (here ^{1}H or ^{4}He ions for protons or alpha particles respectively) and the composition of the target (here natural silicon or carbon) and the output is a table of the range, the electronic and nuclear stopping powers, and the longitudinal and lateral straggling as a

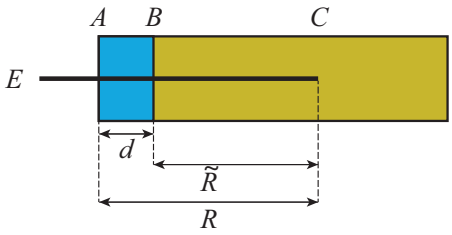

$$E_A = E, \quad R_A = R = \overline{AC},$$
$$E_B = \widetilde{E}, \quad R_B = \widetilde{R} = \overline{BC}$$
$$= \overline{AC} - \overline{AB} = R - d,$$
$$E_C = 0, \quad R_C = 0.$$

Figure 3.3: Illustration for calculation of the energy loss. The particle enters the material at point A with energy E and exits at point B with energy $\widetilde{E}$ depositing the energy $E - \widetilde{E}$ in the slab of thickness d. E_i and R_i are the energy and range of the particle in point $i = A, B, C$ assuming that the yellow part is made of the same material as the blue.

function of the energy of the incoming ion. For our purpose we use only the range as a function of energy.

If we have an ion with initial energy E travelling through a material with thickness d, we can use the corresponding energy-range table to find the energy $\widetilde{E}$ of the outgoing ion. We illustrate the situation in Figure 3.3, where the blue slab is the material with thickness d and the yellow slab is a hypothetical continuation of the material. The particle enters the material at point A with an energy E and exits at point B with an energy $\widetilde{E}$. If the material had continued beyond B (i.e. in the yellow slab) the particle would have stopped in point C. The range R of the particle with energy E in the material is thus the distance between point A and C. We can find this range R corresponding to energy E in the energy-range table using interpolation. At point B the particle must have a range $\widetilde{R}$ equal to $R - d$, since it has already travelled the distance d. The energy $\widetilde{E}$ of the particle at point B can thus be found in the energy-range table using this range $\widetilde{R}$ and interpolation. The energy deposited in the material is then $E - \widetilde{E}$. In this way we can calculate energy losses in the simulation and for the calibration. We do it slab by slab for all the slabs the ion travels through: the carbon target, the silicon dead layer on the DSSSD, the active part of the DSSSD and, if the particle has sufficient energy, also the dead layer on the back of the DSSSD, on the front of the pad detector and on the active part of the pad detector. In this way we can find the energy that is deposited in the detector(s). For the analysis we do the opposite, because

here we measure only the energy deposited in the detector(s). For argon we assume that the beam spot is a point source situated 508 Å inside the collection foil from the beam entrance side, since this is the range in carbon of a $60\,\mathrm{keV}$ ^{31}Ar beam.

3.4 Particle identification and data cut-offs

To reduce electronic noise and contamination from unwanted particles, different cut-offs are used in the analysis. Some cut-offs are used only for specific parts of the analysis and are mentioned in the relevant sections. Here we look at the more general cut-offs used throughout the analysis unless otherwise stated.

Data is recorded continuously, but for the main ^{31}Ar analysis we only include events happening $5\,\mathrm{ms}$ after each proton impact on the production target and until the beam gate was closed $100\,\mathrm{ms}$ after proton impact, see Section 5.4 This is done to reduce the background from long lived components (as ^{16,17}N) in the beam. This will not influence the amount of statistics significantly, since ^{31}Ar has a half-life of $15.1(3)\,\mathrm{ms}$ (see Section 5.5) and most of the collected ^{31}Ar will thus have decayed after $100\,\mathrm{ms}$.

For the analysis presented in Chapter 6 it is important to reduce the background from beta particles as much as possible since we are looking for a proton signal with very low energy around $280\,\mathrm{keV}$. For this reason we only match signals in the front and back strips of the DSSSDs if their energy difference does not exceed $40\,\mathrm{keV}$, while for the other parts of the analysis we use $100\,\mathrm{keV}$ as the limit. For this part of the analysis we also exclude particles believed to be mainly beta particles, giving rise to a low energy signal in both the DSSSD and the corresponding pad detector as described in Section 3.3 (see Figure 3.4 for a graphical illustration). Naturally this can only be done for the detectors with backing, nos. 1, 2, 3 and 6.

Low energy protons will be stopped in the DSSSD, so particles can be identified as such if they give a signal in the DSSSD but none in the pad detector. High energy protons will deposit some of their energy in the DSSSD and the remainder in the pad detector (see Section 3.3 on how to calculate energy loss). They can easily be identified in a ΔE-E plot, where the energy ΔE deposited in the DSSSD is plotted against the energy E deposited in the pad detector.

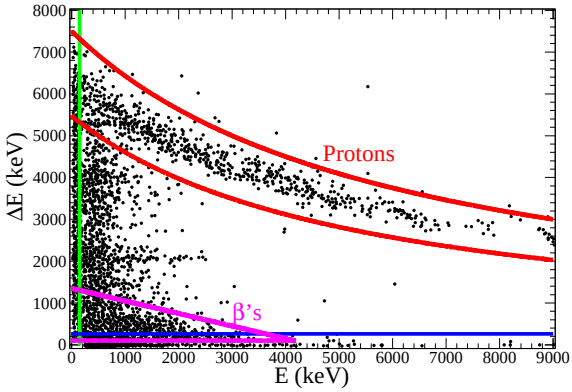

Figure 3.4: Energy in the DSSSD ΔE versus energy in pad detector E for detector 6. The green and the blue line represents the lower cuts in the DSSSD and the pad detector respectively. The high energy protons which are not stopped in the DSSSD are bounded by the two red lines. The particles bounded by the purple lines are believed to be mainly beta signals and are excluded for the analysis in Chapter 6.

This is illustrated in Figure 3.4.

DSSSD 3 gives significantly more signals than the other detectors. This is most likely due to contaminations on the pad detector from the alpha calibration. We solve this by demanding that the particle should be stopped in the DSSSD giving no signal in the pad detector or be identified as a proton in the ΔE-E plot.

Since DSSSD 4 and 5 are not backed by a pad detector we cannot do particle identification for these. Furthermore, the shading of DSSSD 5 (see Section 4.1.1) makes it difficult to determine its actual efficiency. For this reason we omit these DSSSDs for some parts of the analysis.

Unless otherwise stated, we use a lower energy cut-off of $800\,\mathrm{keV}$ for the protons, but allow the lowest energy proton in multi-proton events to have an energy as little as $500\,\mathrm{keV}$ unless it is detected by the thick DSSSD (no. 5) in which the beta particles can deposit more energy.

Since the gamma detectors were not included in the trigger we only include signals in the gamma detectors if a particle with an energy of minimum $800\,\mathrm{keV}$ (and not identified as a beta particle) were detected in the silicon de-

tectors. Furthermore, since the efficiency calibration can only be used above $600\,\mathrm{keV}$ we use this as a lower cut-off on the gamma rays. Finally, we include only events with maximum one signal in each detector in order to discard events where the gamma particle is scattered into the neighbouring clusters (see Section 3.3).

3.5 Simulation

Due to shading effects from the target holder and lower energy cut-offs on the protons, we made a Monte Carlo simulation to more accurately determine the efficiency of the silicon detectors. We also use it to study the resolution of the proton peaks for the different decay channels.

We use the Monte Carlo subroutine `genbod` from `CERNLIB` [CER] which generates multi-particle events weighted according to the Lorentz-invariant Fermi phase space, given initial and final states. The two- and three-proton decays can be simulated directly from the genbod routine or it can be divided into two or three single particle decays through specified states.

The detectors and strips hit by the particles are determined from geometric calculations and the energy losses in dead layers and target are calculated as explained in Section 3.3. The energy deposited in the detectors is then converted to a channel number using the calibration found for the data analysis (Chapter 4). The data are then stored in an n-tuple data structure, which can be analysed using the same analysis routine as the experimental data.

CHAPTER 4

Calibration

To obtain a high resolution it is crucial that the energy and geometry calibration is made with great accuracy. Furthermore, to be able to extract branching ratios a good efficiency calibration is also needed. The task of calibrating is not always straightforward and is often the most time consuming part of the analysis. In this chapter we will go through the calibrations of the different detectors.

4.1 The silicon detectors

As mentioned in Chapter 3 two types of silicon detectors were used for the experiment: Double-sided silicon strip detectors (DSSSDs) and silicon pad detectors. We first go through the calibration of the DSSSDs. They are calibrated in two steps: First, a rough calibration was made using a standard triple alpha sources (^{239}Pu, ^{241}Am and ^{244}Cm) and a ^{148}Gd-source. This calibration was used for analysis during the experiment. To ensure a precise calibration for the final analysis a number of runs with an ^{33}Ar-beam were made throughout the experiment. ^{33}Ar is ideal for calibration of the silicon detectors, since it decays by β-delayed proton emission with well known proton energies. Furthermore, it can be produced by the same target-ion source as ^{31}Ar and guided through ISOLDE in the same way just by changing the Q/M of the separator magnet. We compared the ^{33}Ar spectra for each run to check if the energies drifted during the experiment. This was not the case, which means that we could use a single calibration, made from all the ^{33}Ar runs, in the analysis.

Both calibrations include a geometry and an energy calibration. First, the geometry of the detectors in relation to the source/beam spot is found for each detector. The precise geometry is important for the energy calibration to ensure a correct calculation of the energy deposited in the collection foil and

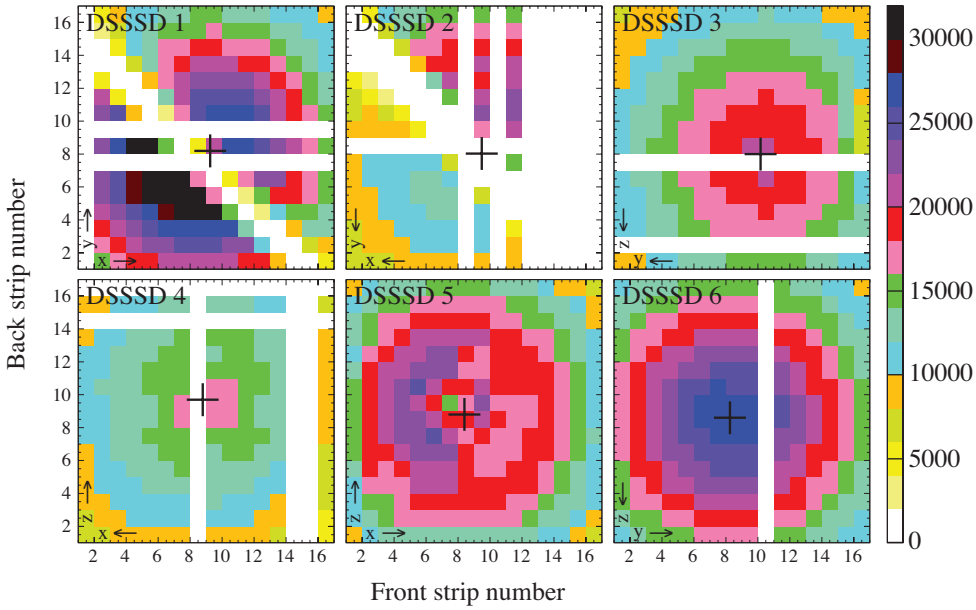

Figure 4.1: Hit-patterns of the DSSSDs from all the ^{33}Ar runs. The midpoint of the beam spot is shown with a cross. Some of the strips were broken, so no particles are detected in these. The positive direction of the x, y and z axis of the coordinate system introduced in Figure 3.2 used for the analysis are shown by symbols such as $y \rightarrow$. The diagonal shadow on DSSSD 1 and 2 are due to the target holder. Furthermore, on DSSSD 5 and 3 the shadow effects from the bolt used for mounting the target holder can be observed. Finally, this shows that there is an excess of counts in the beam side of the cube (i.e. in DSSSD 5 and 6, and half of DSSSD 1 and 2), implying that part of the beam hit the metal holder.

in the dead layers of the detectors. To reduce noise we use a lower cut-off of what corresponds to approximately $1.5\,\mathrm{MeV}$ (it is a channel cut-off) for the alpha calibration. For the ^{33}Ar spectra, where we also have a significant beta background, the alpha calibration is employed and a lower energy cut-off of $1\,\mathrm{MeV}$ is used. Furthermore, the front and back strips are matched with the restriction that their energy difference should not exceed $200\,\mathrm{keV}$. After the first geometry and energy calibration using ^{33}Ar, the energy calibration is repeated. This time using the first obtained calibration from ^{33}Ar and with a restriction of maximum $40\,\mathrm{keV}$ difference between the front and back strips. To further reduce background, we only include events with no signal in the

corresponding silicon pad detectors for the four detectors with backing (nos. 1, 2, 3 and 6). Unfortunately, this reduction cannot be made for the two detectors without backing (nos. 4 and 5).

4.1.1 Geometry calibration

The geometry of the DSSSDs is extracted from their hit-patterns, i.e. the number of events in each pixel on the detector. Since the decay has no preferred direction, we expect the particles to be uniformly distributed over 4π. From geometrical considerations this means that the distribution on a DSSSD in the xy-plane and center in (x, y, z) facing a point source at $(0, 0, 0)$ would be given as

$$\Omega(i, j) = \cos\theta \frac{a^2}{4\pi R^2}, \tag{4.1}$$

with

$$\begin{aligned} R &= \sqrt{R_x^2 + R_y^2 + R_z^2}, \\ \cos\theta &= \frac{R_z}{r}, \end{aligned} \tag{4.2}$$

where

$$\begin{aligned} R_x &= i(a + b) - c + x, \\ R_y &= j(a + b) - c + y, \\ R_z &= z. \end{aligned} \tag{4.3}$$

Here $\vec{R}$ is the vector from the point source to the relevant pixel with front and back strip number i and j respectively, $a = 3.0\,\mathrm{mm}$ and $b = 0.1\,\mathrm{mm}$ are the strip width and strip gab respectively and $c = \frac{16+1}{2}(a + b)$. This can be solved using χ^2-minimisation giving the coordinates (x, y, z) from the hit-pattern of the DSSSD. This method is used for the alpha calibration, where all the spectra have sufficient statistics and the background is easily removed. Even though the alpha source is not a point source, this suffices for a rough first calibration. Note that the orientation of the coordinate system used for the calibration of the DSSSDs is not the same as used for the analysis. For the calibration the orientation is chosen for each DSSSD with the positive z-direction pointing

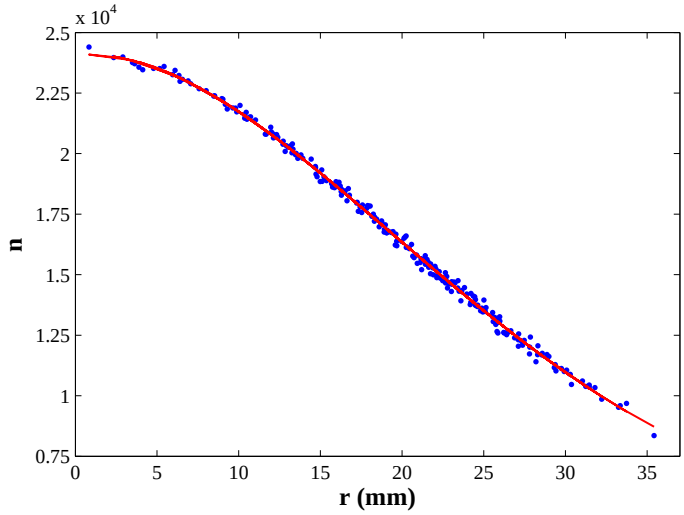

Figure 4.2: The number of counts n in each pixel as a function of the distance r from the pixel to the center of the perpendicular projection of the beam spot onto the detector plane for DSSSD 6. The red line is the fitted fourth order polynomial.

to the DSSSD and positive x- and y-direction following the increasing front and back strip numbers respectively. The orientation of the DSSSDs in the coordinate system used for the analysis is shown in Figure 4.1.

However, the minimisation routine is unstable when using the ^{33}Ar hit-patterns (see Figure 4.1) for a number of reasons: Firstly, the beam is not a point and the ^{33}Ar collected in the foil is thus not a point source. Secondly, the foil is fixed to a metal holder and the beam not only hit the foil but also the metal holder. As a consequence there are more events in the part of the cube where the beam enters, which is clearly observed in DSSSD 1 and 2 in Figure 4.1. Furthermore, there were shading effects caused by the metal holder on the upper and lower DSSSD (nos. 1 and 2) and shading effects on the edge of DSSSD 3 and most of DSSSD 5 caused by a relatively large bolt, which was used for connecting the target holder to a small metal rod entering between detectors 3 and 5. Finally, the minimisation routine is very sensitive to broken strips.

To solve this problem we do the geometry calibration in two steps: First, finding the midpoint of the DSSSD relative to the center of the beam spot,

i.e. the x and y coordinate, and then finding the distance, i.e. the z coordinate. In the same terms as above, the distance of a pixel to the center of the perpendicular projection of the beam spot onto the projector plane is given as

$$r = \sqrt{R_x^2 + R_y^2}. \tag{4.4}$$

We then plot the number of counts n as a function of the distance r for each pixel and find that this forms a curve, which can be approximated by a fourth order polynomial, see Figure 4.2. When the detector is correctly placed in relation to the center of the beam spot, the points will be as close to the polynomial as possible. The correct value for the x and the y coordinate can thus be found by minimising the sum of the absolute difference between all points and the polynomial, that is by minimising:

$$\sum_i \mathrm{abs}\left(f_4(r_i) - n_i\right), \tag{4.5}$$

where f_4 is the fourth order polynomial. However, it is not possible to choose a fixed function for f_4, since the distance r, and thereby the shape of the polynomial, is directly related to the detector position. Instead we use a sum of orthogonal polynomials as described by R. Barlow in Ref. [Bar00]:

$$f_4(r) = c_0 + c_1 P_1(r) + c_2 P_2(r) + c_3 P_3(r) + c_4 P_4(r) \tag{4.6}$$

with

$$c_t = \frac{\overline{nP_t}}{\overline{P_t^2}} = \frac{\sum_i n_i P_t(r_i)}{\sum_i P_t(r_i)^2}, \tag{4.7}$$

where the orthogonal polynomials are given as

$$P_t(r) = b_{0t} P_0(r) + b_{1t} P_1(r) + \ldots + r^t \tag{4.8}$$

with

$$b_{st} = -\frac{\sum_i r_i^t P_s(r_i)}{\sum_i P_s(r_i)^2}. \tag{4.9}$$

Table 4.1: The coordinates (x,y,z) of the midpoint of the DSSSDs with respect to the coordinate system introduced in Figure 4.1 are shown below together with the thickness of the DSSSDs and the solid angle Ω of the working strips (see Figure 4.1 and Section 4.1.2).

Detector	1	2	3	4	5	6
Thickness (μm)	69	288	300	287	494	296
x (mm)	0.8	-1.5	39.3	0.7	-1.9	-36.0
y (mm)	-2.5	3.0	-3.6	38.4	-36.9	-2.3
z (mm)	30.5	-39.0	3.1	2.2	-0.6	1.2
Ω (% of 4π)	7.6	3.1	7.5	6.5	9.4	9.0

This minimisation is done for each detector. For DSSSD 1 and 2, where there are more events in one half of the detector, a factor to scale the side with the lowest number of counts is found and included. The pixels with fewer counts caused by shading or broken strips are not included in the minimisation. The perpendicular projection of the midpoint of the beam spot onto the detectors is shown in Figure 4.1.

We can now determine the z coordinate by assuming a point source, i.e. using Eq. (4.1) with fixed x and y. Due to the shading effects and the excess of counts on the beam side of the cube, this cannot be done for DSSSD 1, 2 and 5. For DSSSD 5 we can assume that the distance between DSSSD 5 and 4 is the same as between DSSSD 3 and 6 based on the construction of the cube. For DSSSD 1 and 2 the z coordinate is found from physical measurements. The coordinates of the detectors in the coordinate system introduced in Figure 3.2 are shown in Table 4.1.

4.1.2 Energy calibration of the strip detectors

The energy calibrations of the DSSSDs are made strip by strip using histograms of the number of counts as a function of channel for each strip. Figure 4.3 shows one of these histograms for the alpha calibration. The histograms here contain four peaks, one for the main decay of each isotope. The kth peak corresponds to the energy $\widetilde{E}_k$ deposited in the active part of the detector. The known energies E_k for the decays thus have to be corrected for the

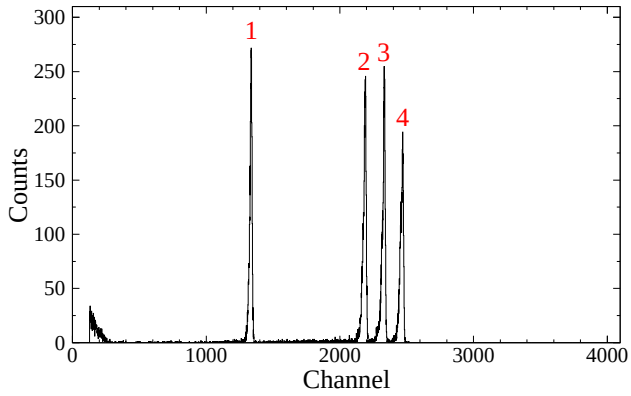

Figure 4.3: The energy spectrum from the alpha source for front strip 7 of DSSSD 4 before calibration showing the energy deposited in the active part of the strip.

energy loss in the dead layer of the detector. This can be done as described in Section 3.3. However, the distance travelled in the dead layer depends on the angle of the incident particle which varies over the strip as depicted in Figure 4.4. It does not vary significantly over a pixel and we can thus calculate the corrected energy $\widetilde{E}_{k,ij}$ for each pixel using its midpoint as point of entry. For each front strip i (back strip j) we thus have 16 different $\widetilde{E}_{k,ij}$s for each peak k. But since we need one calibration for the entire front (back) strip we can use only one value for $\widetilde{E}_k$ per peak for each strip i (j). To find $\widetilde{E}_k$ from the 16 $\widetilde{E}_{k,ij}$s we use a weighted average, where the weight is the number of counts n_{ij} in the pixel deduced from the hit-pattern. For each strip we then have four $\widetilde{E}_k$s, which we can fit to the four peaks in the corresponding energy spectrum. We do this by first fitting the peaks to Gaussian distributions to find their mean and then perform a linear calibration to the $\widetilde{E}_k$s using χ^2-minimisation. Finally, the calibration is improved by including all the decay channels of the isotopes.

The ^{33}Ar calibrations are done in a similar manner. We can only use protons which are stopped in the DSSSD and we thus demand that only noise is detected in the pad detector behind the DSSSD (except for DSSSD 4 and 5). The proton spectrum of ^{33}Ar contains several peaks as shown in Figure 4.5. So to ensure that the calibration routine can identify the peaks chosen for calibra-

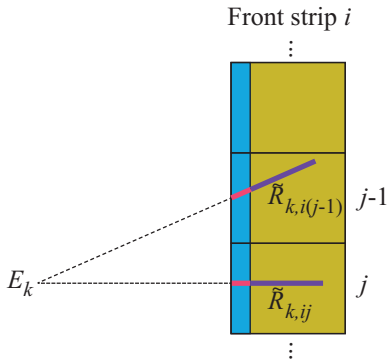

$$\widetilde{R}_{k,ij} \to \widetilde{E}_{k,ij},$$
$$\widetilde{R}_{k,i(j-1)} \to \widetilde{E}_{k,i(j-1)},$$
$$R_{k,ij} > \widetilde{R}_{k,i(j-1)},$$
$$E_{k,ij} > \widetilde{E}_{k,i(j-1)}.$$

Figure 4.4: Section of a front strip i. A particle with energy E_k will deposit different energy in the 16 different pixels on the strip. As an example we consider here pixel j and $j-1$ of strip i. The total distance travelled in the detector (pink plus purple line) of the particle is the same in the two pixels, but due to the difference in angle the (purple) distance $\widetilde{R}$ travelled (and thus the energy $\widetilde{E}_k$ deposited) in the active (yellow) parts are different.

tion, we use spectra with only these peaks included. As mentioned above, we employ the previous calibration to reduce noise and background by matching the front and the back strips. This also allows us to determine one set of upper and lower bounds for each peak, which can by used for all the strips. The energy is then converted back to channel number and the histograms are filled. To make the weighted average we also fill hit-patterns for these particles. Since the matching allows the energy deposited in the front and the back strip to be different (up to either $200\,\mathrm{keV}$ or $40\,\mathrm{keV}$), there will be a few events, where for example, the energy deposited in the back strip lies below the lower bound for a peak, while the energy deposited in the front strip lies above. For this reason we fill two hit-patterns for each detector: One corresponding to the particles included in the front strip histograms and one corresponds to the particles included in the back strip histograms.

For the calibration of DSSSDs 3–6, three well known levels of ^{33}Cl are chosen: $3971.24(19)\,\mathrm{keV}$, $4112.34(20)\,\mathrm{keV}$, and $5548.6(5)\,\mathrm{keV}$ [Che11], corresponding to proton energies of $1642.8(5)\,\mathrm{keV}$, $1779.5(5)\,\mathrm{keV}$, and $3171.9(7)\,\mathrm{keV}$. The ^{33}Ar spectrum can be seen in Figure 4.5, where the peaks used for calibration are marked. They are first corrected for the energy lost in the collection

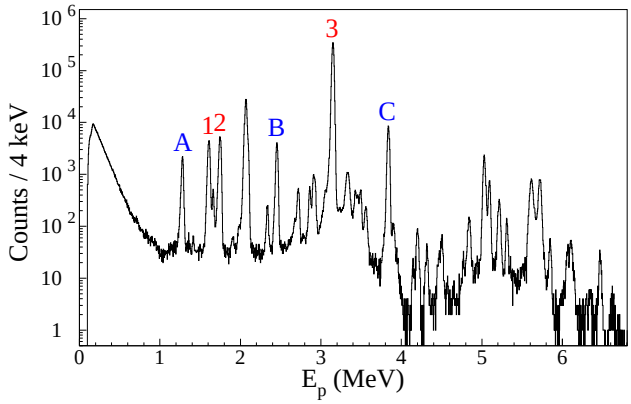

Figure 4.5: The calibrated energy spectrum for ^{33}Ar for DSSSD 3. The peak marked with red numbers are used for calibration of DSSSDs 3–6. The energies of the peaks marked with blue letters are found from the calibrated energy spectra of DSSSD 3 and 6. For calibration of DSSSD 2 peaks 3, B and C are used and for calibration of DSSSD 1 peaks 1, 2, A and B are used.

foil and in the dead layer of the DSSSD pixel by pixel and then averaged using the weights obtained from the hit-patterns, as described for the alpha calibration. The lines are clearly identified in the proton spectrum and their means are again found by a Gaussian fit. We then perform a linear calibration to the known energies corrected for energy losses by χ^2-minimisation using the uncertainties of the known energies, since they are significantly larger than the errors from the Gaussian fits. DSSSD 2 has several broken strips and thus fewer counts. For this reason the $1642.8(5)$-keV and $1779.5(5)$-keV lines cannot be identified and instead two higher-lying proton peaks are used. Their energies are $2479.2(20)\,\mathrm{keV}$ and $3856.9(20)\,\mathrm{keV}$ found from the calibrated proton spectra of DSSSD 3 and 6. We use the spectrum for DSSSD 3 and 6 because they have the best energy resolution since their pad detectors can be used to eliminate background. Due to the small thickness of DSSSD 1, not all protons with energies above $2.5\,\mathrm{MeV}$ are stopped in the detector. For calibration of this detector the $1642.8(5)$-keV and $1779.5(5)$-keV lines are used together with two proton peaks found from DSSSD 3 and 6 at $1320.1(20)\,\mathrm{keV}$ and $2479.2(20)\,\mathrm{keV}$. Not all peaks are visible in all strips, which is the reason why four energies are chosen.

4.1.3 Energy calibration of the pad detectors

Protons with energies below $6\,\mathrm{MeV}$ are stopped in the $300\,\mu\mathrm{m}$ DSSSDs so the ^{33}Ar runs cannot be used to calibrate the back detectors. Instead the calibration is made using the α-sources and the DSSSDs unmounted. It is done in a similar way as described for the alpha calibration of the DSSSDs, but here the weighted average of the $E_{n,ij}$s is done over the entire detector, since only one set of E_ns can be used. Due to the thickness of DSSSD 1 the calibration can be tuned using the $3171.9(7)$-keV proton peak to find the thickness of the dead layer on the back of the DSSSD and on the front of the pad detector. It is found to be $800\,\mathrm{nm}$ and $790\,\mathrm{nm}$ respectively and these values are then used for all the detectors.

The uncertainty on the overall calibration of the silicon detectors are estimated to be $3\,\mathrm{keV}$ for energies up to $6\,\mathrm{MeV}$. The protons with energies above $6\,\mathrm{MeV}$ will pass through the $300\,\mu\mathrm{m}$ DSSSDs and deposit the rest in the pad detector behind. Since there is a high uncertainty on the alpha calibration of the pad detectors the uncertainty will be larger for higher proton energies. The uncertainty can be found by considering the decay of the IAS as described in Section 8.1. From the energy of the IAS (found from the two-proton decays), the proton separation energy of ^{31}Cl (from Ref. [Saa11]) and the energies of the levels in ^{30}S (see Table 2.1) we can calculate the energy of the one-proton lines and compare them to the signal in our detectors. We see that detector 6 has the best resolution, but that the energies are up to $150\,\mathrm{keV}$ below what we expect from calculations. For DSSSD 2 and 3 differences are up to $70\,\mathrm{keV}$. When possible we thus consider the spectra separately for high energies and take the energy from detector 3 using $80\,\mathrm{keV}$ as the uncertainty.

4.1.4 Efficiency calibration

The proton efficiency is taken as the angular coverage of the DSSSDs. The solid angle of the working strips, i.e. excluding broken strips, for the individual DSSSDs is listed in Table 4.1. For DSSSD 1 and 2 the pixels shaded by the target holder are also excluded. These pixels are also excluded from the analysis.

The total solid angle is $43(2)\,\%$ of 4π. For parts of the analysis the two detectors without backing are disregarded giving a total solid angle of $27(2)\,\%$ of

4π. Protons with energies below $500\,\mathrm{keV}$ can be stopped inside the collection foil depending on their emitted angle. The low-energy protons, which are of interest for this work, have an energy around $280\,\mathrm{keV}$ (see Chapter 6). The solid angle of these protons is $20(2)\,\%$ of 4π when the two detectors without backing are disregarded.

To normalise of the total number of ^{31}Ar collected during the run, we can use the largest one-proton peak at $2083\,\mathrm{keV}$ (see Section 5.1) with a known absolute branching ratio of $26.2(29)\,\%$ [Axe98a, Baz92]. This normalisation was used for the publications [Kol13, Kol14a, Kol14b], but the total beta-delayed proton branching ratio has been measured very recently by Lis *et al.* [Lis15] to $77.4(3)\,\%$. We also measure the total beta-delayed proton branching ratio and can thus compare and rescale this to the branching ratio measured by Lis *et al*. From this we get that the absolute branching ratio of the one-proton peak at $2083\,\mathrm{keV}$ is $25.9(10)\,\%$.

Since a small fraction of the activity could only be seen from the beam entrance side and because of the different shading effects, the extracted total number of ^{31}Ar collected vary depending on which detector is used. An overall estimate of the number of ^{31}Ar collected during the experiment can be found using DSSSD 6 as $6.03(\,24) \times 10^5$. When using all detectors we use an average of $5.6(4) \times 10^5$.

The two-proton efficiency times the total number of ^{31}Ar, when including only detectors 3 and 6 (in Chapter 8) can be found by weighing the two-proton efficiencies with the total number of ^{31}Ar calculated from events in detector 3 and 6, $N_{\mathrm{Ar,d3}}$ and $N_{\mathrm{Ar,d6}}$. It is then given as

$$N_{\mathrm{Ar,d3}} \cdot \varepsilon_{2p,\mathrm{d3+6}} + \left(N_{\mathrm{Ar,d3}} - N_{\mathrm{Ar,d6}}\right) \varepsilon_{2p,\mathrm{d6}}, \tag{4.10}$$

where $\varepsilon_{2p,\mathrm{d3+6}} = \left(\Omega_{\mathrm{d3}} + \Omega_{\mathrm{d6}}\right)^2$ and $\varepsilon_{2p,\mathrm{d6}} = \Omega_{\mathrm{d6}}^2$ are the two-proton efficiencies when including both detector 3 and 6 and when including only detector 6, respectively. We then divide by the overall average estimate of ^{31}Ar we get an effective two-proton efficiency for detector 3 and 6 of $2.4(3)\,\%$.

The three-proton efficiency is estimated to be $6.2(16)\,\%$, when using all the detectors and lower energy cut-offs as described in Section 3.4.

Table 4.2: Coordinates of the center of the MINIBALL detectors, defined as the point where the three hexagonal clusters touch [War13].

	x	y	z
Ge 1 (mm)	−17	103	50
Ge 2 (mm)	100	−21	16

4.2 Germanium detectors

The coordinates of the MINIBALL detectors are found from physical measurements and can be found in Table 4.2.

The energy and efficiency of the MINIBALL germanium detectors was calibrated by J. Kusk and a detailed exposition can be found in Ref. [Kus11]. We will now give a short summary and describe some improvements and checks that we made.

4.2.1 Energy calibration

A preliminary energy calibration of each of the clusters is made using ^{137}Cs and ^{60}Co and then improved using a ^{152}Eu source and high energy gamma lines from the decay of ^{16}N and ^{15}C, which are found in the runs with ^{31}Ar. A linear approximation is used, which was shown to be accurate to about $1\,\mathrm{keV}$ for gamma energies less than $1.8\,\mathrm{MeV}$. At higher energies non-linear effects might play a significant role, and therefore an uncertainty of $3\,\mathrm{keV}$ is assigned to the calibration for gammas above $1.8\,\mathrm{MeV}$. This part was made by J. Kusk and a detailed exposition can be found in Ref. [Kus11]. Using the decays of ^{16,18}N and ^{32,33}Ar recorded on-line, we find that this calibration can be improved above $1.8\,\mathrm{MeV}$ by shifting the energies upwards by $0.7\,\mathrm{keV}$. The uncertainty of the energies in the interval 1.8–$2.5\,\mathrm{MeV}$ is thus reduced to $1\,\mathrm{keV}$, while it is still $3\,\mathrm{keV}$ for energies above $2.5\,\mathrm{MeV}$. This shift is not done in the analysis program but only later when extracting energies from the gamma spectra.

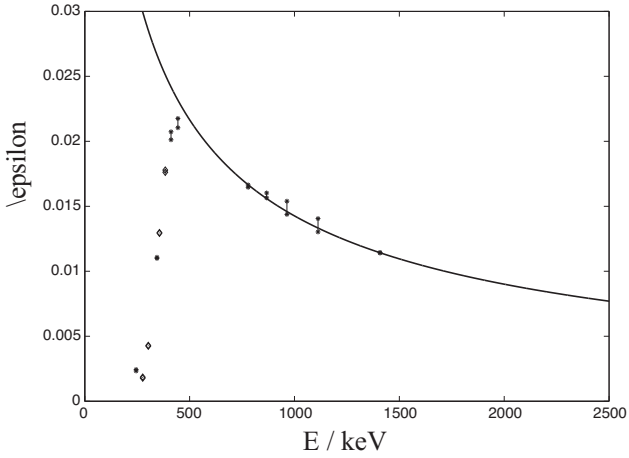

Figure 4.6: The efficiency calibration of the MINIBALL detectors from Ref. [Kus11]. The rhombi represents the absolute calibrated points from ^{133}Ba and the asterisks represents the relative calibrated points from ^{152}Eu. The full line is the function from Eq. (4.11).

4.2.2 Efficiency calibration

A total efficiency calibration was made for the two MINIBALL detectors by J. Kusk and a detailed description can also be found in Ref. [Kus11]. First an absolute efficiency calibration is made using Ref. [Deb88] and the low-lying gamma lines from a ^{133}Ba source with a known activity of $17.0(3)\,\mathrm{kBq}$ at the time of the experiment. The gamma lines from the ^{152}Eu source are corrected for emission probabilities using Ref. [Deb88] to obtain the relative efficiency between them. They are then scaled so the 344-keV point from ^{152}Eu is placed on a straight line between the 302- and 356-keV points from ^{133}Ba as shown in Figure 4.6.

To be able to find the efficiency for the gamma lines detected in the experiment we need an analytical formula to represent the efficiency above the $600\,\mathrm{keV}$ cut-off. Above this the energy dependence of the efficiency is believed to originate only from the detectors. Thus the absolute efficiency above $600\,\mathrm{keV}$ can be found by scaling the results from an experiment with a slightly different detector configuration [Joh13] (which used four different gamma sources: ^{152}Eu, ^{60}Co, ^{207}Bi and ^{11}Be) to fit our 1408-keV ^{152}Eu-point. The result,

using the formula in Ref. [Rad95], is

$$\varepsilon_\gamma(E) = 0.21 \exp\left(-2.669 - 1.457 \log\left(\frac{E}{\mathrm{MeV}}\right) - 0.231 \left[\log\left(\frac{E}{\mathrm{MeV}}\right)\right]^2 \right), \tag{4.11}$$

and is shown in Figure 4.6 together with the calibrated data points from ^{133}Ba and ^{152}Eu.

We check the efficiency calibration using the runs made with ^{33}Ar and runs made with ^{32}Ar during the experiment. Gating the proton spectrum from the decay of ^{33}Ar on the measured $2230.5(10)$-keV gamma line we find that a proton line at $1293(3)\,\mathrm{keV}$ is reduced by a factor of $8.2(4) \times 10^{-3}$. This is then the gamma efficiency at $2230.5\,\mathrm{keV}$ and we can compare it to $\varepsilon_\gamma(2230.5\,\mathrm{keV}) = 8.3 \times 10^{-3}$ obtained from Eq. (4.11). For ^{32}Ar we gate the proton spectrum on a measured gamma line at $1248.5(10)\,\mathrm{keV}$ and find that the proton line at $1190(3)\,\mathrm{keV}$ is reduced by a factor of $10.7(14) \times 10^{-3}$ and from Eq. (4.11) we get $\varepsilon_\gamma(1248.5\,\mathrm{keV}) = 12.4 \times 10^{-3}$. We conclude that we can use Eq. (4.11) to find the efficiency and estimate an uncertainty of $10\,\%$. It should be noted that the MINIBALL detectors were not in the trigger in the data acquisition, and the gamma rays are thus only saved to the data if a signal is detected in the DSSSDs.

CHAPTER 5

Overview of the data and the first results

In this chapter we will have a first look at the data to get an overview before going into a detailed analysis in the next chapters. In the end of the chapter we will determine the half-life of ^{31}Ar (Section 5.5) and examine the gamma spectrum of ^{33}Ar (Section 5.6).

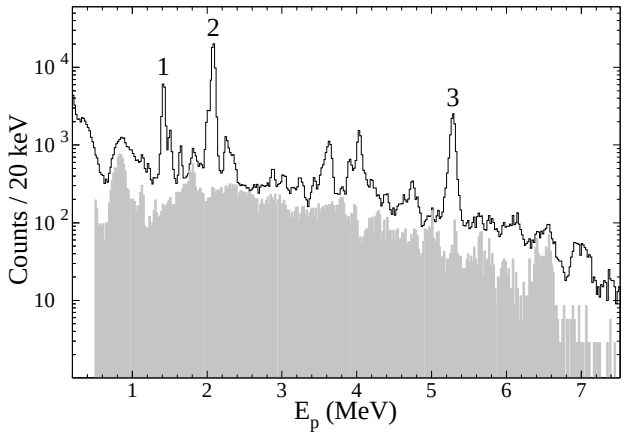

Figure 5.1: The one-proton spectrum for all the data with the two-proton data shown in grey scaled with the relative detection efficiency. Since all the detectors are used there is a large uncertainty on the efficiency and thereby the scaling. Another version of this spectrum can be seen in Figure 8.4, where only a subset of the data is shown resulting in a more precise scaling.

5.1 The one-proton spectrum

Figure 5.1 shows the one-proton spectrum for the whole data set (with no lower energy cut-off) with the two-proton data shown in grey scaled with the relative detection efficiency. The upper part of the spectrum is omitted here. In the spectrum we can identify three major one-proton peaks at $1418(3)\,\mathrm{keV}$, $2083(3)\,\mathrm{keV}$ and $5286(5)\,\mathrm{keV}$. They correspond to proton decays to the ground level in ^{30}S from levels in ^{31}Cl at $1748(5)\,\mathrm{keV}$, $2436(5)\,\mathrm{keV}$ and $5746(7)\,\mathrm{keV}$, respectively. The 2-MeV peak has two components: the $2083(3)$-keV line and a $2008(3)$-keV line, which corresponds to the decay from a ^{31}Cl level at $5762(5)\,\mathrm{keV}$ to the second excited state in ^{30}S.

5.2 The two-proton data

Figure 5.2 shows the two-proton (2p) data. In the scatter spectrum each event is represented by two dots in the same horizontal line, i.e. two proton energies corresponding to one Q_{2p} value. From the scatter plot we clearly see that the decay is mainly sequential, since we can identify a number of diagonal and vertical lines in the spectrum. When several levels in ^{31}Cl decay through a

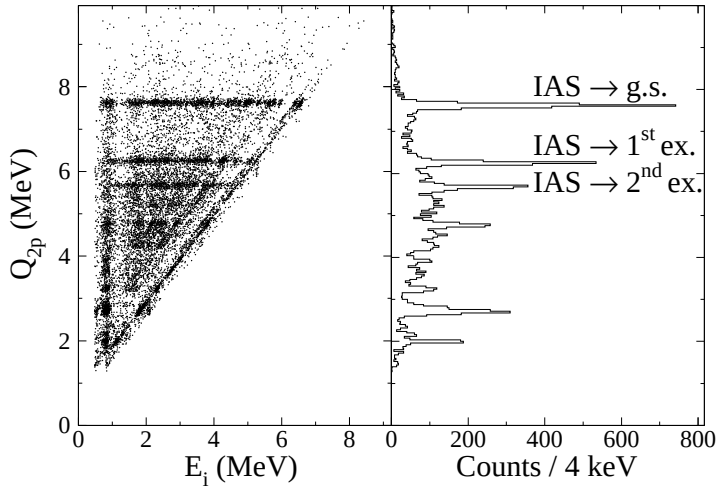

Figure 5.2: The two-proton data. Left: Q_{2p} plotted against the energy E_i of the two particles. Right: The projection onto the Q_{2p}-axis.

single state in ^{30}S to, for example, the ground state in ^{29}P, their Q_{2p} value will differ while the energy of the second proton will be the same (when neglecting recoil) for all the events, which creates a vertical line. The energy of the first emitted proton will depend linearly on the Q_{2p} value, which makes a diagonal line. The diagonal and vertical lines in the spectrum are thus clear evidence of the decay going through several states in ^{30}S. In the right part of Figure 5.2 we can clearly identify the decay of the IAS to the first, second and ground state of ^{29}P. The decay of the IAS will be examined in detail in Section 8.1.

5.3 The gamma spectrum

The full gamma spectrum with no time or proton gate is shown in Figure 5.3. The peaks in the spectrum all originate from background and beam contamination mainly from nitrogen isotopes. A detailed analysis can be found in Ref. [Kus11]. Here we will focus on the gamma rays in the beta-proton daughters of ^{31}Cl (i.e. ^{30}S and ^{29}P) and we will thus only consider the time and proton gated gamma spectrum shown in Figure 6.2a.

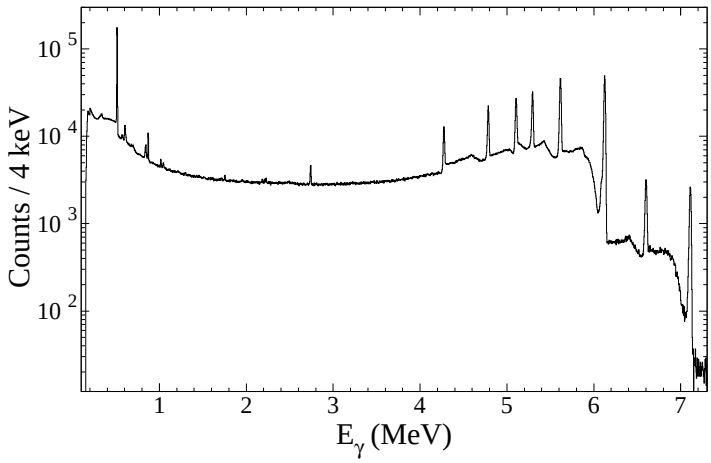

Figure 5.3: The gamma spectrum with no time or proton gate.

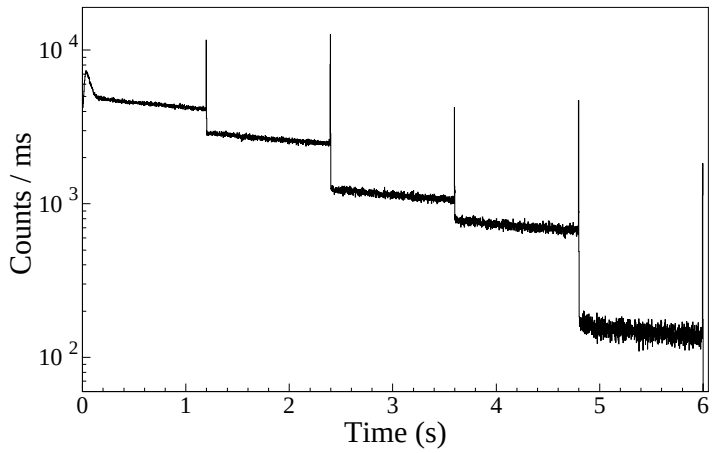

Figure 5.4: The time spectrum of all the events in the ^{31}Ar runs, where at least one particle is detected in the DSSSDs.

5.4 The time spectrum

Figure 5.4 shows the time spectrum of all the events in the ^{31}Ar runs where at least one particle is detected in the DSSSDs. The time is measured from the last proton impact on the primary production target. The super cycle of the PS Booster is $1.2\,\mathrm{s}$, but since ISOLDE does not receive all the pulses from the PS Booster the time between proton impacts will vary, but it will always be some multiple of $1.2\,\mathrm{s}$. The peak in the beginning is the accumulation followed by the rapid decay of ^{31}Ar. Since ^{31}Ar is short-lived (see Section 5.5) the beam gate was closed $100\,\mathrm{ms}$ after proton impact on the production target, so for the analysis we will focus on events from $5\,\mathrm{ms}$ to $100\,\mathrm{ms}$ after proton impact.

5.5 The half-life of ^{31}Ar

To determine the half-life of ^{31}Ar we consider only the events recorded after the beam gate was closed at $100\,\mathrm{ms}$ after proton impact on the production target. To minimise background contributions, we use only the strongest one-proton peak at $2083\,\mathrm{keV}$, corresponding to an energy range between $2040\,\mathrm{keV}$ and $2120\,\mathrm{keV}$. We then plot the number of events as a function of time from proton impact and fit the data using the maximum likelihood method to a

single exponential component and a constant background. The background is insignificant and we obtain a half-life of $15.1(3)\,\mathrm{ms}$. By gating on the one-proton peak at $5.3\,\mathrm{MeV}$, we confirm the result, but obtain a larger uncertainty due to less statistics. Our result is consistent with previous determinations of $14.1(7)\,\mathrm{ms}$ [Fyn00], $15(3)\,\mathrm{ms}$ [Bor87b] and $15.1^{+1.3}_{-1.1}\,\mathrm{ms}$ [Baz92].

5.6 The gamma decay of ^{33}Ar

As explained in Chapter 4, a number of runs with ^{33}Ar were made during the experiment for calibration of the detectors. The gamma spectrum from these runs, i.e. the gamma rays in the decay of ^{33}Ar, can be seen in Figure 5.5. The peak marked with Arabic numerals corresponds to transitions in the beta-daughter ^{33}Cl, the peaks marked with Roman numerals corresponds to transitions in the beta-granddaughter ^{33}S and the one marked by an asterisk to a transition in the beta-proton daughter ^{32}S. A, B, C and D are peaks from annihilation, pile-up and gamma-transitions from decays of ^{40}K and ^{18}N. This assignment is supported by the half-life found for the peaks by

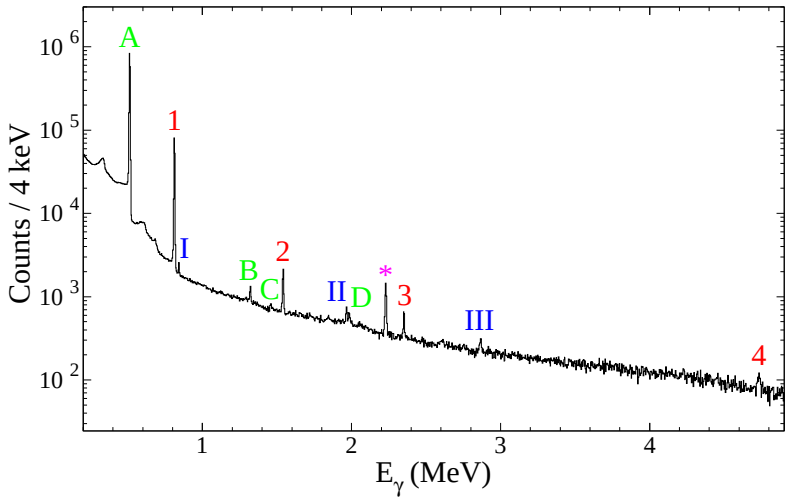

Figure 5.5: The gamma spectrum of ^{33}Ar. The Arabic numerals correspond to transitions in the beta-daughter ^{33}Cl, the Roman numerals to transitions in the beta-granddaughter ^{33}S and the asterisk to a transition in the beta-proton daughter ^{32}S. The letters correspond to background lines.

J. Kusk [Kus11]. The relative intensities of the gamma lines observed in the decay of ^{33}Ar are given in Table 5.1. They are compared to results from three different experiments [Adi10, Bor87a, Wil80]. The interesting transition is the peak at $4734.0(20)\,\mathrm{keV}$. This is an M1 transition of the IAS in ^{33}Cl to the first excited state in ^{33}Cl, which is the anti isobaric analogue state of ^{33}Ar [Esw72]. The M1 transition is very strong and accounts for $92(8)\,\%$ of the gamma decays of the IAS [End78]. This gamma-transition has never previously been observed in the decay of ^{33}Ar, even though the branching ratio of ^{33}Ar to the IAS in ^{33}Cl is $31.0(1)\,\%$ [Adi10].

Table 5.1: The relative branching ratios of the gamma-transitions in the decay of ^{33}Ar (above the line) and ^{33}Cl (below the line). The peak identifier corresponds to Figure 5.5. The intensities of the gamma-transitions from the ^{33}Ar decay are normalised to peak 1 and compared to the results of Ref. [Adi10]. The transition marked by an asterisk is compared to Ref. [Bor87a] as suggested in Ref. [Adi10]. The intensities of the gamma-transitions from the decay of ^{33}Cl are normalised to peak III and compared to the results of Ref. [Wil80].

Peak	E_γ (keV)	I_γ	E_γ^{ref} (keV)	I_γ^{ref}
1	811.2(10)	100(10)	810.6(2)	100(1)
2	1541.0(10)	3.2(3)	1541.4(6)	3.6(2)
3	2342.3(11)	1.10(13)	2352.5(6)	1.3(2)
4	4734(3)	0.46(9)		
*	2230.4(19)	3.9(4)	2230.6(9)	1.7(5)
I	841.3(10)	109(16)	841	118.6(36)
II	1966.9(12)	132(18)	1966	104.2(16)
III	2867(3)	100(15)	2866	100.0(18)

CHAPTER 6

The levels in ^{30}S relevant to astrophysics

We saw in Section 2.2 that the levels just above the proton threshold in ^{30}S are important for determining the reaction rate of $^{29}\mathrm{P}(p,\gamma)^{30}\mathrm{S}$, which influences the rp-process in x-ray bursts and the silicon abundances that can be studied directly from presolar dust grains believed to be produced in classical novae.

In this chapter we will make a detailed investigation of the ^{30}S levels interesting for astrophysics. In addition to determining their energies, we will go through two new methods: One for finding the ratio between the proton and gamma partial widths of these levels and one for determining their spin.

6.1 Identification and energy determination

We begin by considering the excitation energy of ^{30}S calculated from multiplicity-two events using Eq. (1.32) as shown in Figure 6.1. Since we are looking for levels just above the proton threshold, we omit the lower energy cutoff on the second proton in this and the following section. Three peaks below $6\,\mathrm{MeV}$ are clearly identified. Their energies are $5227(3)\,\mathrm{keV}$, $5390(4)\,\mathrm{keV}$ and $5845(5)\,\mathrm{keV}$ consistent with previous measurements cited in Table 2.1. Note that they are all higher than the energies measured by Fynbo *et al.* [Fyn00] even though they are measured in a similar manner from the same decay. This is due to the energy loss in the collection foil and dead layers, which is not included in Ref. [Fyn00]. This gives rise to a systematic error due to the dE/dx energy variation when the energy of the measured protons differs significantly from the energy of the protons used for calibration. As an example, the protons from the 5.2-MeV level will have an energy between $0.6\,\mathrm{MeV}$ and $1\,\mathrm{MeV}$ and if we assume they hit the middle of the DSSSD they will lose about

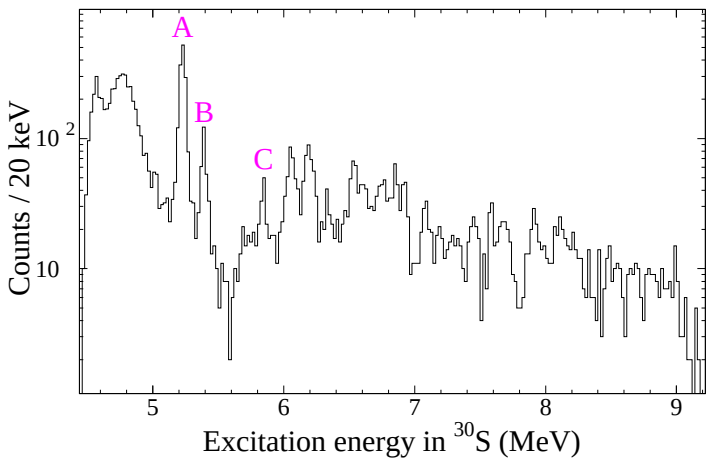

Figure 6.1: The excitation energy of ^{30}S calculated from multiplicity-two events using Eq. (1.32).

30–45 keV in the foil and the dead layer of the DSSSD. By comparison, the protons used for calibration will lose only about 10–25 keV. Not including the energy losses will thus lead to the deduced energies being systematically lower. The uncertainties on the energies measured by Fynbo *et al.* do not include the uncertainty on the calibration. This explains why our uncertainties are larger, even though our energy resolution is better than the one obtained by Fynbo *et al*. The energies found here should replace the ones stated in Ref. [Fyn00].

The levels below 5 MeV cannot be identified in the two-proton decay due to contamination from beta particles and electronic noise, which we cannot distinguish from low energy protons. Instead we turn to the proton-gated gamma spectrum in Figure 6.2a, since the levels below 5 MeV are known to primarily decay by gamma emission. The identified lines, their widths, their relative intensities and their total branching ratios are given in Table 6.1. Previously, only the 1194.1- and the 2210.4-keV lines have been observed in the decay of ^{31}Ar [Axe98a]. The most interesting line from an astrophysical viewpoint is the 2478.8-keV line. It corresponds to the decay of the first level above the proton threshold in ^{30}S to the first excited state in ^{30}S. The 2210.4-keV line corresponds to the decay of the first excited state and together with the 2478.8-keV line we get that the energy of this level is 4689.2(23) keV in com-

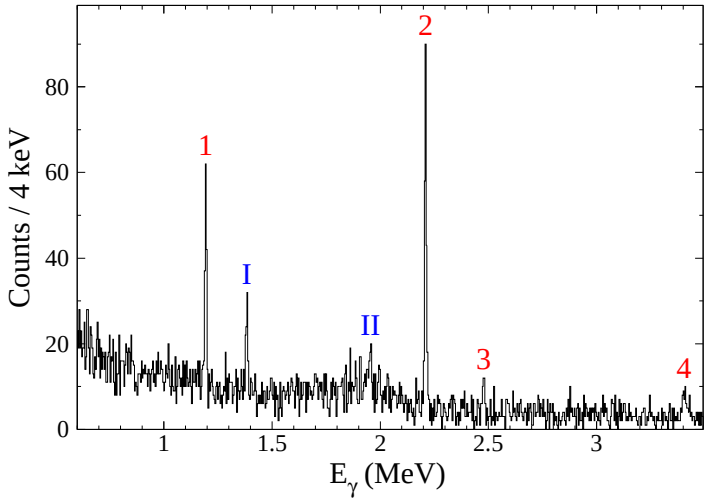

(a)

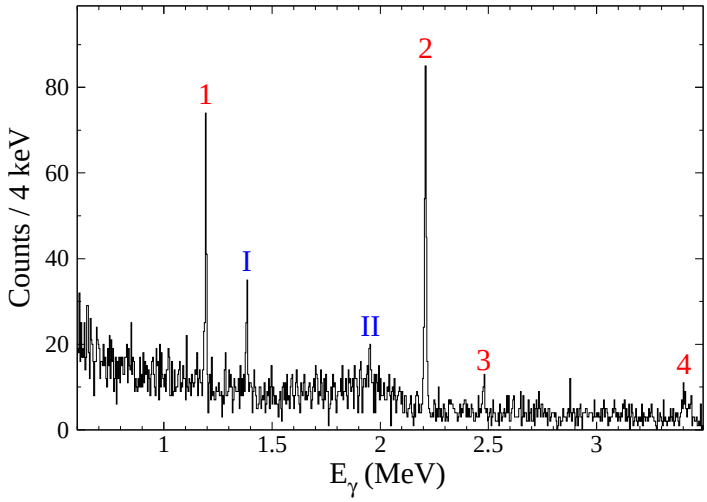

(b)

Figure 6.2: (a) The proton-gated gamma spectrum. The numbers correspond to transitions in ^{30}S and the Roman numbers correspond to transitions in ^{29}P. The energies of the marked peaks and their relative intensities can be found in Table 6.1. (b) The same as (a), but with the gamma energies Doppler shifted using Eq. (1.36).

Table 6.1: The energies of the gamma lines in Figure 6.2a and their full-width half-maximum widths (FWHM), their relative intensities normalised to the 2210.4-keV line and their branching ratio (B.R.) of the total number of ^{31}Ar decays. Peak 4 is spilt into two peaks 4a and 4b after Doppler correction (cf. Section 6.1.1) and the listed values for these two are found using the Doppler corrected spectrum (Figure 6.2b).

Peak	Energy (keV)	FWHM	Intensity	B.R. (%)
1	1194.1(11)	9.7(12)	39(6)	3.6(6)
2	2210.4(12)	8.7(9)	100(13)	9.6(15)
3	2478.8(20)	10.8(28)	15(4)	1.4(4)
4	3411(5)	31(4)	30(7)	2.9(7)
4a	3405(5)	18(6)	21(12)	2.0(6)
4b	3432(5)	15(6)	9(6)	0.8(6)
I	1383.6(14)	10.4(12)	22(4)	1.3(3)
II	1955(4)	12(7)	13(8)	0.8(5)

plete agreement with the previous measurements listed in Table 2.1. Unfortunately we do not see any gamma rays from the $4809.0(3)$-keV level. We do see a small indication of an excess of events around $2585\,\mathrm{keV}$, but not enough to identify it as a peak. However, its energy is anyway too low to identify it with the $2598.6(4)$-keV gamma line from its decay to the first excited level.

6.1.1 The double structure of the 3411-keV gamma line

The 1194.1-keV and the 3411-keV lines both correspond to decays of the second excited state in ^{30}S. From the 2210.4-keV line and the 1194.1-keV line we get that the energy of the second excited state is $3404.5(16)\,\mathrm{keV}$ in agreement with previous measurements in Table 2.1. We suspect that the difference in energy from the ground state decay of the level is due to a double structure of the peak at $3411(5)\,\mathrm{keV}$, since we see a spike in a single bin at $3430\,\mathrm{keV}$. This is supported by the fact that the relative intensity between the 1194.1-keV and the 3411-keV line of $0.77(22)$ differs from $0.25(4)$ measured in Ref. [Kuh73] by two standard deviations. From Eq. (1.37) we expect that the 3411-keV peak should be broader than the 1194.1-keV peak by a factor of $2.856(5)$. Here we

find that it is broader by a factor of $3.6(6)$ and thus a discrepancy of more than one standard deviation.

To further test this hypothesis we will consider the Doppler shift of the lines as described in Section 1.3.1. Assuming that the measured proton has the same, but opposite, momentum as the nuclei emitting the gamma ray we can correct for the Doppler shift using Eq. (1.36). The Doppler corrected gamma spectrum is shown in Figure 6.2b. However, this assumption only holds for the decays of short-lived levels in ^{30}S fed directly in the proton decay, i.e. only for the two gamma lines from the second excited level and the 2478.8-keV gamma line. We do see that these peaks are more narrow in the Doppler corrected spectrum. According to Eq. (1.36) the measured gamma energy should depend linearly on the square-root of the proton energy times the angle between the gamma ray and the proton. Unfortunately there are very limited statistics in the peaks from the decay of ^{31}Ar and even for the 1194.1-keV gamma line we cannot confirm this relation conclusively as shown in Figure 6.3a. Instead we look at the 2230-keV gamma line in ^{32}S from the decay of ^{33}Ar (cf. Section 5.6), where we have much better statistics. The proton gated events of this peak are shown in Figure 6.3b where we clearly see the linear dependence. This justifies the use of Eq. (1.36) for short-lived levels fed directly in the beta-delayed proton decay.

With this justification we can now return to the Doppler corrected gamma spectrum in Figure 6.2b, where we see that the peak at $3411(5)$ keV seems to be split into two peaks: One at $3405(5)$ keV and one at $3432(5)$ keV. The energy of the lower peak agrees completely with the $3404.5(16)$ keV energy found from the cascade decays. The relative intensity of the 1194.1-keV and the 3405-keV lines is here $0.55(16)$, which is still only consistent with $0.25(4)$ within two standard deviations, but with a significantly lower uncertainty than the ratio found using the non-Doppler corrected spectrum. We conclude that there are indeed two contributions to the 3411-keV peak, with the lower originating from the ground state decay of the 3405-keV level in ^{30}S.

We now wish to find a candidate for the higher contribution to the peak with an energy around 3432 keV. Since we only see the peak in the proton gated spectrum, we first search in the beta-delayed proton daughters of ^{31}Ar: ^{30}S, ^{29}P and ^{28}Si. We find only one level with approximately the right energy, namely the $3447.6(4)$-keV level in ^{29}P. However, previously no ground state

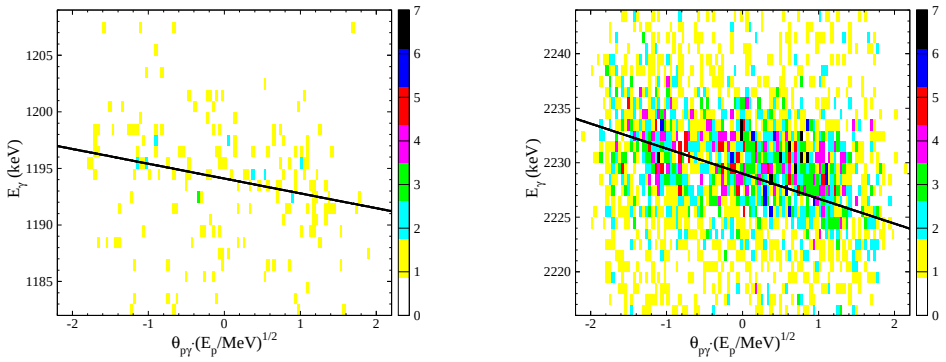

Figure 6.3: The detected gamma energy as a function of the square-root of the proton energy times the angle between the proton. The solid line shown follows Eq. (1.36). (a) The 1194.1-keV gamma line in ^{30}S in the decay of ^{31}Ar. (b) The 2230-keV gamma line in ^{32}S from the decay of ^{33}Ar.

decay has been observed from this level. It decays primarily with a $1493.6\,\mathrm{keV}$ gamma ray [Bas12], which we do not see in our spectrum. Another possibility is that it is a gamma ray from a transition in the beta-granddaughters of ^{31}Ar, but since the peak is not seen without employing the time gate, this is highly unlikely. It is ultimately excluded since the detection of a 3432-keV gamma transition in a beta-granddaughter of ^{31}Ar would entail detection of other stronger gamma transitions in said nucleus. These we do not see in our gamma spectra.

This leaves only ^{31}Cl. Here we would expect it to be the decay of the IAS, since this is the only level in ^{31}Cl which has a life-time long enough to allow gamma decays. A gamma decay of the IAS in ^{31}Cl has never been observed although it is expected since it is seen in both ^{32}Ar [Bha08] and ^{33}Ar (Section 5.6). If the upper part of the 3411-keV peak originates from the decay of the IAS, it does not make sense to Doppler correct these gamma rays with the method used here, since no protons have been emitted from the nucleus prior to the gamma decay. The energy determined here should thus have a larger uncertainty than the $5\,\mathrm{keV}$ deduced from the fit and the calibration. In Figure 6.2a we see a spike in a single bin at $3430\,\mathrm{keV}$, so we assume that the energy of the gamma transition is $3431(6)\,\mathrm{keV}$. Using the energy of the IAS

determined in Section 8.1 to be $12\,313(4)\,\mathrm{keV}$ we predict the existence of a level in ^{31}Cl with an energy of $8882(7)\,\mathrm{keV}$.

To learn more about the transition we now compare with the gamma rays from ^{32}Ar and ^{33}Ar. As mentioned in Section 5.6 the strongest gamma decay of the IAS of ^{33}Ar is an M1 transition from a ($J^\pi = \frac{1}{2}^+$, $T = \frac{3}{2}$) level to a ($J^\pi = \frac{1}{2}^+$, $T = \frac{1}{2}$) level, believed to be the anti isobaric analogue state (AIAS) [Esw72]. ^{32}Ar has $J^\pi = 0^+$ and a gamma transition between the IAS and AIAS is thus forbidden. Instead the IAS gamma-decays to three ($J^\pi = 1^+$, $T = 1$) states [Bha08]. The ground state of ^{31}Ar is a ($J^\pi = \frac{5}{2}^+$, $T = \frac{5}{2}$) level so an M1 gamma transition from the IAS to the AIAS is allowed. We know neither the spin nor the isospin of the 8882-keV level in ^{31}Cl nor the multipolarity of the gamma transition from the IAS. However, by comparison with the ^{32,33}Ar decays and what is known about the AIAS in this region of the nuclear chart (see Section 1.1.4), we would assume that the detected gamma-decay of the IAS of ^{31}Ar is also an M1 IAS to AIAS transition.

From Table 6.1 we see that the total branching ratio of the gamma decay is $0.8(6)\,\%$ and we should thus expect to see the decay of the 8882-keV level in our one- and two-proton decay spectra. We do see peaks in the one-proton spectrum around the energies corresponding to the decay of this level to the ground level and to the first six excited states in ^{30}S. However, if we look at the protons gated on the broad gamma line at $3411\,\mathrm{keV}$, we do not see any protons with these energies. In the two-proton spectrum we see indications of peaks corresponding to the two-proton decay to the ground state and the first excited level in ^{29}P, but due to limited statistics we cannot identify them as peaks. The assignment of the $3431(6)$-keV gamma line as the gamma decay of the IAS thus remains tentative.

As a consistency check we find from the one- and two-proton decay spectrum that the total branching ratio for the decay of ^{31}Ar to a ^{31}Cl level at $8882(7)\,\mathrm{keV}$ is $0.85(13)\,\%$. This is an upper limit since there can be other contributions to the proton peaks found in the one- and two-proton spectra. The proton peak from the decay of the 8882-keV level to the ground state in ^{30}S can for example not be separated from the proton peak from the IAS decay to the 3405-keV level in ^{30}S. As described in Section 1.1.4 we would expect the 8882-keV level to also be fed in the Gamow-Teller decay. However, from Ref. [Wil69] we expect the Gamow-Teller feeding to be around an order of

magnitude smaller than the feeding via the gamma decay of the IAS. The upper limit of $0.85(13)\,\%$ on the total feeding of the 8882-keV level is consistent with this due to the large uncertainty on the $0.8(6)\,\%$ branching ratio found for the feeding via the gamma decay of the IAS. We can compare these branching ratios with ^{32}Ar and ^{33}Ar by dividing with the total branching ratio b_F for feeding the IAS to obtain Γ_γ/Γ. We use the theoretical value of $4.24(43)\,\%$ (found in Section 8.1) and get $< 20(4)\,\%$ and $< 19(14)\,\%$, respectively. This is of the same order of magnitude as Γ_γ/Γ for ^{32}Ar and ^{33}Ar, which we find to be $8.5(29)\,\%$ [Oue11] and $7(12)\,\%$ [Che11], respectively.

6.2 The relative proton and gamma partial widths

Returning now to the levels relevant to astrophysics, i.e. the levels above the proton threshold, we have identified four levels at $4689.1(24)\,\mathrm{keV}$, $5227(3)\,\mathrm{keV}$, $5390(4)\,\mathrm{keV}$ and $5845(5)\,\mathrm{keV}$. The first is one of the two levels thought to dominate the $^{29}\mathrm{P}(p,\gamma)^{30}\mathrm{S}$ reaction rate, cf. Section 2.2.3. This can also be seen in Table 6.2, where theoretical calculations of the ratio between the proton and gamma partial widths are shown. Unfortunately, we were not able to identify the most dominant level at $4809\,\mathrm{keV}$. However, in Section 6.2.5 we will search for this level in the decay of the IAS.

The four levels identified have been found in either the gamma spectrum or the proton spectrum, but unfortunately not both. This means that we cannot easily deduce the ratio between the proton and gamma partial widths. To overcome this we need to reduce the background further around the relevant energies. We can assume that we have detected the first proton in the decay from ^{31}Cl, since the gamma spectrum is gated on a proton and the other ^{30}S levels are found from the two-proton events. Then if we can identify which protons populate the levels in ^{30}S, we can limit our analysis to include only such protons and thus limit the background. We will do this for each of the levels in the following subsections. To further reduce background we omit the two detectors without backing.

Table 6.2: Ratios between calculated proton and gamma partial widths from previous work compared to the 95 % confidence limits we estimate here.

Setoodehnia *et al*. [Set13]			Almaraz-Calderon *et al*. [Alm12]			Richter and Brown [Ric13]			Present work	
E_x (keV)	J^π	Γ_γ/Γ_p	E_x (keV)	J^π	Γ_γ/Γ_p	E_x (keV)	J^π	Γ_γ/Γ_p	E_x (keV)	Γ_γ/Γ_p
4688.1(4)	3^+	270				4688	3^+	370	4689.1(24)	> 5.3
4812.0(20)	2^+	1.3				4809	2^+	2.3		
5132.3(5)	(4^+)	≥ 13	5130	4^+	3.4×10^{-2}	5132	4^+	†		
5225.0(20)	(0^+)	$\geq 0.34 \times 10^{-3}$	5217.8	0^+	0.7014×10^{-3}	5218	0^+	0.93×10^{-3}	5227(3)	< 0.5
						5219	3^+	0.40×10^{-2}		
5315.0(20)	(3^-)	8.8×10^{-3}	5312.1	3^-	4.6	5312	3^-	5.2×10^{-3}		
5393.0(20)	3^+	0.686×10^{-2}	5382	2^+	3.8954×10^{-2}	5382	2^+	0.75×10^{-2}	5390(4)	< 7
5849.0(20)	(2^+)	1.8×10^{-4}	5835.5	4^+	15.7	5836	4^+	†	5845(5)	< 10
5947.0(20)	(4^+)	1.8×10^{-1}								

† No value for Γ_p is given.

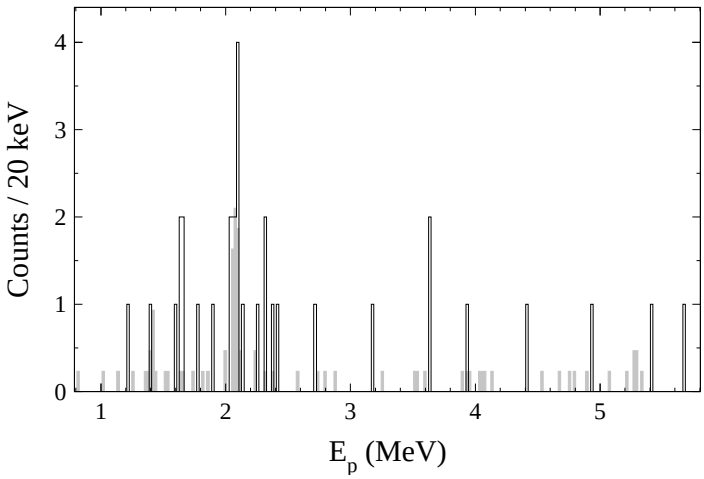

Figure 6.4: The proton spectrum gated on the 2478.7-keV gamma line. The grey histogram is the background found by gating on gamma rays on both sides of the 2478.7-keV gamma line.

6.2.1 The 4689-keV level

The 4689-keV level was identified in the gamma spectrum by the $2478.7(21)$-keV gamma line, so we gate on this gamma line to find the protons feeding this level. Their energies are plotted in Figure 6.4n together with the background, which we find by gating on either side of the $2478.7(21)$-keV gamma line and scale. The peak at $2.1\,\mathrm{MeV}$ originates from a known one-proton decay to the ground state of ^{30}S as described in Section 5.1. Subtracting the background we have an excess of events around $1.6\,\mathrm{MeV}$ and $2.3\,\mathrm{MeV}$ so we can assume that the 4689-keV level is mainly populated by protons with energies around these energies. Due to the limited statistics in this spectrum we look to the one-proton spectrum to find the upper and lower limits of the two intervals, by requiring that the entire proton peaks are included. We find that gating on protons in the intervals $[1580, 1920]$ and $[2200, 2430]\,\mathrm{keV}$ lowers the background in the gamma spectrum substantially while keeping the majority of the events in the 2478.7-keV gamma line. This is clearly seen in the gamma spectrum in Figure 6.5a, which is gated on protons with energies in one of these intervals. The ^{30}S energies calculated from multiplicity two events with the same proton gate are shown in Figure 6.5b. The 4689-keV level is still not

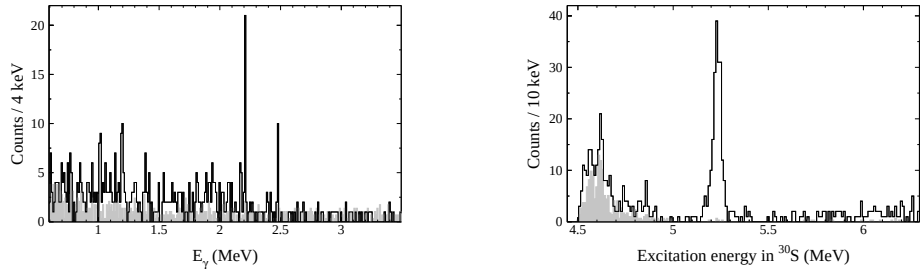

(a) **(b)**

Figure 6.5: Spectra gated on proton energies in the intervals $[1580, 1920]\,\mathrm{keV}$ and $[2200, 2430]\,\mathrm{keV}$ and the background spectra (grey) gated on protons with energies in the interval $[2040, 2120]\mathrm{keV}$ and scaled by $f = 0.321(4)$, which corresponds to the ratio between the number of protons gated on in the interesting intervals and for the background. (a) The gamma spectrum. (b) Excitation energy in ^{30}S calculated from multiplicity two events using Eq. (1.32).

positively identified, so we can only find an upper limit on the Γ_p/Γ_γ ratio. The background can be estimated by gating on the known strong one-proton peak between the two intervals at $2083(3)\,\mathrm{keV}$ (cf. Section 5.1). We do this by gating on the interval $[2040, 2120]\mathrm{keV}$ and then scale the spectra by a factor $f = 0.321(4)$, which corresponds to the ratio between the number of protons gated on in the interesting intervals compared to the number of protons gated on for the background. We then find that the number of gamma rays corresponding to the decay of the 4689-keV level to the first excited state in ^{30}S is $(12 - f10)$. Since we cannot identify the level in Figure 6.5b we find an upper limit for the number of two-proton events as the number of events in a 50-keV interval around $4689\,\mathrm{keV}$. We find $(21 - f38)$ events. Due to the limited number of counts in the spectra it is necessary to determine the upper limit through a simulation. The upper limit is found from an ensemble, which is made by drawing four numbers n_i from a probability function $P(n_i|n_{0i})$, where n_{0i} are the four numbers found from the spectra ($n_{01} = 21$, $n_{02} = 38$, $n_{03} = 12$, $n_{04} = 10$). This probability function is derived as follows: n_{0i} is a number from a Poisson distribution with mean value λ_i and the n_is needed to create the ensemble are random numbers drawn from a Poisson distribution

with this mean value λ_i. The problem arises because λ_i is unknown. Therefore, one has to integrate over all the possible values of λ_i weighted with the probability of this λ_i given n_{0i}:

$$\begin{aligned} P(n_i|n_{0i}) &= \frac{\int_0^\infty d\lambda_i P(n_i|\lambda_i)P(\lambda_i|n_{0i})}{\int_0^\infty d\lambda_i P(\lambda_i|n_{0i})} \\ &= \int_0^\infty d\lambda_i P(n_i|\lambda_i)P(n_{0i}|\lambda_i) \\ &= \frac{(n_i+n_{0i})!}{n_i!n_{0i}!}\frac{1}{2^{n_i+n_{0i}+1}}, \end{aligned} \tag{6.1}$$

where we for the second equality make use of the Poisson distribution being normalised in λ_i and Bayes's theorem, which gives $P(\lambda_i|n_{0i}) = P(n_{0i}|\lambda_i)$ when employing a uniform prior distribution.

We can then find the Γ_p/Γ_γ ratio from these four random numbers n_i drawn from the four distributions by correcting for efficiencies:

$$\frac{\Gamma_p}{\Gamma_\gamma} = \frac{(n_1 - fn_2)/\varepsilon_p}{(n_3 - fn_4)/\varepsilon_\gamma}, \tag{6.2}$$

where the gamma efficiency ε_γ includes the gamma intensities measured by Lotay *et al*. [Lot12]. We produce an ensemble of 10^5 Γ_p/Γ_γ values from which we then find a $95\,\%$ confidence upper limit of 0.19 on the Γ_p/Γ_γ ratio.

Setoodehnia *et al*. [Set13] have shown that the level is a 3^+ level. They calculate the Γ_p/Γ_γ ratio to 0.37×10^{-2} and Richter and Brown [Ric13] calculate it to be 0.27×10^{-2}. The experimental upper limit is thus two orders of magnitude higher than the values found from calculations.

6.2.2 The 5227-keV level

The 5227-keV level is only seen in the two-proton spectrum, whose background we reduce by gating on the protons feeding the level. They are found to have energies in the intervals $[1000, 1350]$ and $[1670, 1950]$keV. The background can be estimated by gating on protons from another strong transition to the ground state of ^{30}S with proton energies in the interval $[1380, 1460]$keV (see Section 5.1). The two-proton spectrum and the gamma spectrum can be seen in Figure 6.6. Lotay *et al*. have observed a level at $5218.8(3)$ keV from its gamma decay to the first excited state of ^{30}S by a $3008.5(2)$-keV gamma and to the second excited state by a $1814.4(3)$-keV gamma with relative branching

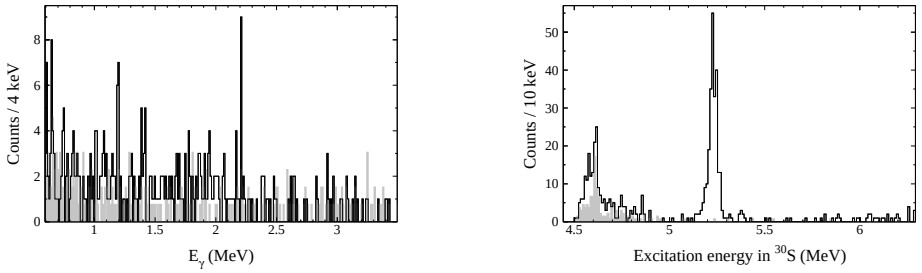

(a) **(b)**

Figure 6.6: Spectra gated on proton energies in the intervals $[1000, 1350]\,\mathrm{keV}$ and $[1670, 1950]\,\mathrm{keV}$ and the background spectra (grey) gated on protons with energies in the interval $[1380, 1460]\mathrm{keV}$ and scaled by $f = 0.703(11)$, which corresponds to the ratio between the number of protons gated on in the interesting intervals and for the background. (a) The gamma spectrum. (b) Excitation energy in ^{30}S calculated from multiplicity two events using Eq. (1.32).

ratios of $0.80(9)$ and $0.20(12)$, respectively [Lot12]. These lines are not seen in the proton gated gamma spectrum (Figure 6.6a). Assuming this is the same level as we have identified in the two-proton spectrum at $5227(3)\,\mathrm{keV}$, we can thus only find an upper limit on the Γ_γ/Γ_p ratio.

The number of two-proton events in the ^{30}S peak at $5227\,\mathrm{keV}$ is 224 ± 16. Since no gamma peak is seen we look in a 50-keV interval around $3008\,\mathrm{keV}$, corresponding to the gamma decay to the first excited state in ^{30}S. We find one gamma ray, but five in the background spectrum, which we have to scale by the factor $f = 0.703(11)$, defined above as the ratio between the number of protons gated on in the interesting intervals and the number of protons gated on for the background. This gives a $95\,\%$ upper limit on the number of gamma rays of 2.32 [Fel98]. If we then correct for efficiencies and include the gamma intensities from Ref. [Lot12], we estimate the $95\,\%$ confidence upper limit of the Γ_γ/Γ_p ratio to be 0.5.

As seen in Table 6.2 calculations for a 0^+ level with energy around $5.2\,\mathrm{MeV}$ gives values for the Γ_γ/Γ_p of the order of 10^{-3} while a 3^+ gives a ratio of 0.40×10^{-2}. Both values are well below the upper value found here. Almaraz-Calderon *et al*. [Alm12] found a proton branching ratio of $1.00(2)$ for a level at

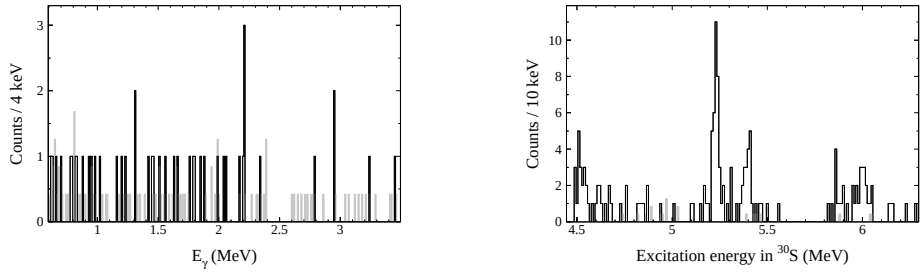

(a) (b)

Figure 6.7: Spectra gated on proton energies in the intervals $[5700, 6600]$ keV and the background spectra (grey) gated on protons with energies in the interval $[5240, 5340]$keV and scaled by $f = 451(11)$, which corresponds to the ratio between the number of protons gated on in the interesting interval and for the background. (a) The gamma spectrum. (b) Excitation energy in ^{30}S calculated from multiplicity two events using Eq. (1.32).

$5200(44)$ keV, but this is hard to reconcile with the gamma rays observed by Lotay *et al*. [Lot12] from a level at $5218.8(3)$ keV if this is the same state. The state populated by Lotay *et al*. was shown to be a 3^+ state, while the spin of the state populated by Almaraz-Calderon *et al*. is not known. We will investigate the spin of the state populated here in Section 6.3.

6.2.3 The 5390-keV level

The 5390-keV level was also only seen in the two-proton spectrum and we find that it is populated by protons with energies in the interval $[5700, 6600]$. Gating on these protons we get the spectra in Figure 6.7, with the background found by gating on the interval $[5240, 5340]$keV as described in Section 5.1. We find 19 ± 4 events in the peak at 5390 keV in Figure 6.7b. The gamma decay of this level has not been observed. However, assuming that the strongest gamma-decay is to the first excited state, as for the 5227-keV and the 5845-keV level, we can search for the gamma rays at $3180(4)$ keV. We find no events in a 50 keV interval around this level and a single event in the background spectrum, which has to be scaled by the factor $f = 0.451(11)$ defined again as the ratio between the number of protons gated on in the interesting intervals

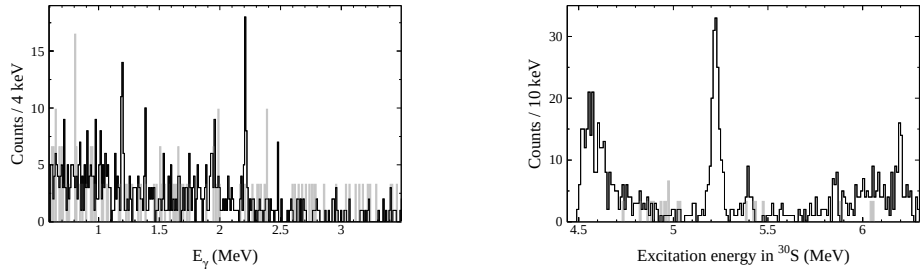

(a) (b)

Figure 6.8: Spectra gated on proton energies in the intervals $[2220, 3400]\,\mathrm{keV}$ and $[5540, 6160]\,\mathrm{keV}$ and the background spectra (grey) gated on protons with energies in the interval $[5240, 5340]\mathrm{keV}$ and scaled by $f = 2.89(5)$, which corresponds to the ratio between the number of protons gated on in the interesting intervals and for the background. (a) The gamma spectrum. (b) Excitation energy in ^{30}S calculated from multiplicity two events using Eq. (1.32).

and the number of protons gated on for the background. The resulting 95% upper limit on the number of gamma rays becomes 2.69. Assuming that all the gamma decays from this level go to the first excited state, we get a 95% upper limit on the Γ_γ/Γ_p ratio of 7. From Table 6.2 we see that this is again a few orders of magnitude above the values obtained from calculations.

6.2.4 The 5845-keV level

We again start by cleaning the spectra by gating on the protons feeding the level. They are found to have energies in the intervals $[2220, 3400]\mathrm{keV}$ and $[5540, 6160]\mathrm{keV}$. We estimate the background as for the 5390-keV level. The spectra are shown in Figure 6.8. The number of two-proton events in the ^{30}S peak at $5845\,\mathrm{keV}$ is 21 ± 7. Lotay *et al*. have observed the gamma decay of this level to the first excited state of ^{30}S by a $3637.7(4)$-keV gamma ray [Lot12]. We do not observe this gamma ray in our spectrum. Instead we find the $95\,\%$ upper limit on the number of gamma rays to be 3.93 [Fel98] from the $2 - f1$ gamma rays observed in a $50\,\mathrm{keV}$ interval around $3637.7\,\mathrm{keV}$. The scale factor $f = 2.89(5)$ is also here defined as the ratio between the number of protons gated on in the interesting intervals and the number of protons gated on for

the background. Lotay *et al*. measured only this gamma decay from the 5390-keV level so we assume that the level exclusively decays by gamma emission to the first excited state. With this assumption we find the 95% upper limit on the Γ_γ/Γ_p ratio to be 10.

Almaraz-Calderon *et al*. [Alm12] do not observe any significant proton branch from this level in their $^{28}\mathrm{Si}(^3\mathrm{He}, n)^{30}\mathrm{S}$ experiment. This does not agree with our result of a proton branching ratio of 0.1 ($95\,\%$ C.L.). They assume it to be a 4^+ state and estimate that $\Gamma_\gamma/\Gamma_p = 15.7$ in contradiction to our upper limit of 7 ($95\,\%$ C.L.). Setoodehnia *et al*. made calculations for a 2^+ level around this energy and found $\Gamma_\gamma/\Gamma_p = 1.8 \times 10^{-4}$ and for a 4^+ level $100\,\mathrm{keV}$ higher where they found $\Gamma_\gamma/\Gamma_p = 1.8 \times 10^{-1}$. Both values disagree with the values from Almaraz-Calderon *et al*. but are in full agreement with the limit we have estimated here.

6.2.5 The 4809-keV level populated in the IAS decay

We have not been able to identify the 4809-keV level in the gamma spectrum or the two-proton spectrum. However, since we should populate the level in the ^{31}Ar decay as indicated by Borge *et al.* [Bor90], we search for the level in the decay of the IAS. The energy of the IAS is found in Section 8.1 to be $12\,313(4)\,\mathrm{keV}$ so the protons from the IAS that populate the 4809-keV level will have an energy of $6986(6)\,\mathrm{keV}$. In the proton spectrum in Figure 6.9a we do see a peak around this energy, but this peak is broad so it will also include the IAS decay to the 4689-keV level. We cannot distinguish these two levels due to our deficient resolution at high energies. However, the ISOLDE experiment from 1997 made by Fynbo *et al.* [Fyn15] had a much better resolution at high energies and the protons feeding the two levels are here clearly separated as can be seen in Figure 6.9b. The energies in this spectrum are a little different from our data in Figure 6.9a, since Fynbo *et al.* did not correct for dead layers. However, the two peaks at $7\,\mathrm{MeV}$ shown in Figure 6.9b are a clear indication of both levels being fed in the decay of the IAS.

The broad peak at $6.5\,\mathrm{MeV}$ in Figure 6.9a should correspond to the IAS decay to the 5227-keV level and the 5390-keV level in ^{30}S, which were clearly identified in Figure 6.1. This peak is clearly separated into two in Figure 6.9b and we see that the widths of these peaks are comparable to the widths of

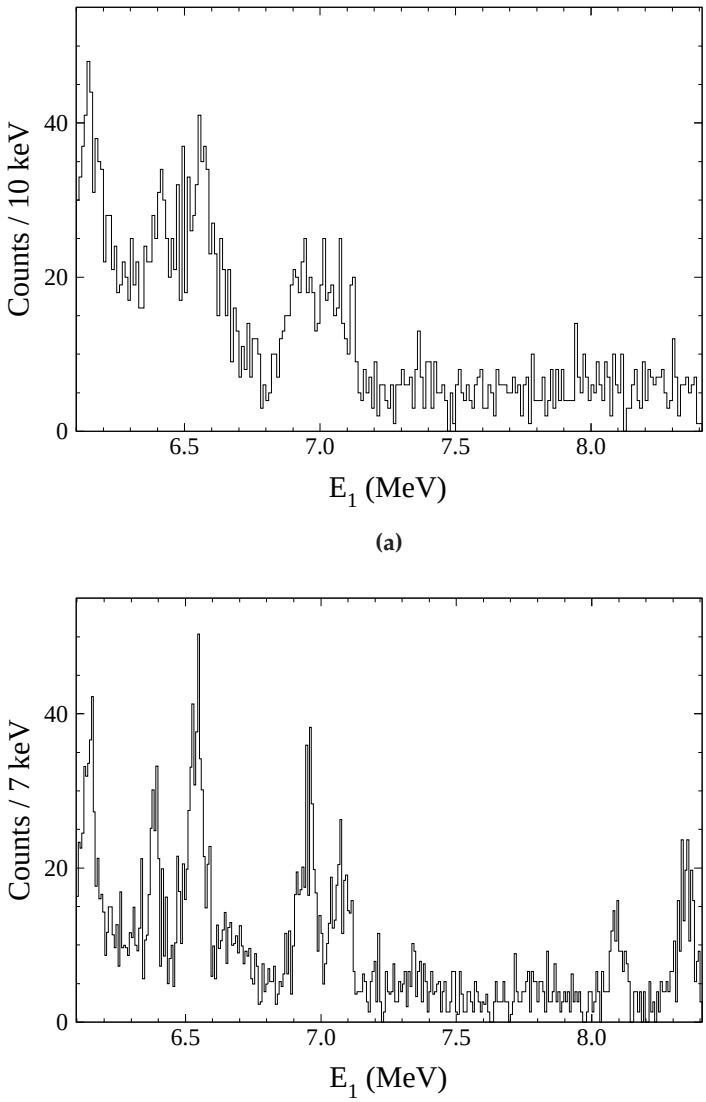

Figure 6.9: The proton energy spectrum for the energy interval of interest for the IAS decay to the levels just above the proton threshold in ^{30}S. (a) Spectrum made from all the detectors. (b) Spectrum made from the 1997 ISOLDE experiment by Fynbo *et al.* [Fyn15].

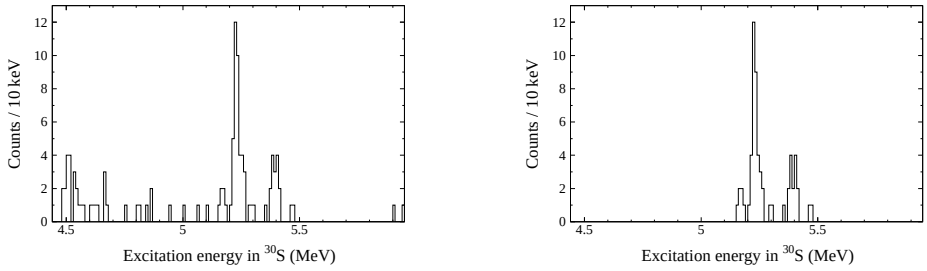

Figure 6.10: (a) The ^{30}S excitation spectrum calculated from multiplicity-two events, where one of the protons has an energy in the interval $[6340, 6700]\,\mathrm{keV}$ corresponding to the decay of the IAS to the 5227-keV level and the 5390-keV level in ^{30}S. (b) The same spectrum as (a) reduced by demanding that the Q_{2p} of the two protons correspond to the decay of the IAS to the ground state of ^{29}P, i.e. belong to the 7.6-MeV peak in Figure 5.2.

the two peaks in this spectrum at $7\,\mathrm{MeV}$ supporting the hypothesis that these peaks also stem from the decay of the IAS. We now gate on the two broad proton peaks in Figure 6.9a at $6.5\,\mathrm{MeV}$ and $7\,\mathrm{MeV}$ and search for two-proton events. To have as much statistics as possible we include detector 4 and 5 when gating on the high energy proton, but to minimise beta background we do not include either DSSSD 4 or 5 for the low energy proton. The calculated ^{30}S spectra are shown in Figure 6.10a and Figure 6.11a. The background in these spectra can be reduced by demanding that the Q_{2p} of the two protons should correspond to the decay of the IAS to the ground state of ^{29}P, i.e. belong to the 7.6-MeV peak in Figure 5.2. These spectra are shown in Figure 6.10b and Figure 6.11b. We do see that the beta background is significantly lowered and from Figure 6.10b we see that this extra cut does not influence the number of real two-proton events in the peaks.

The 5227-keV level and the 5390-keV level primarily decay by proton emission and as expected they are clearly identified in Figure 6.10. The ratio between the number of events in the two peaks is $40(11)\,\%$. This agrees very well with the ratio of $45(4)\,\%$ between the two peaks at $6.5\,\mathrm{MeV}$ in Figure 6.9b (from Table 6.2 we see that we can assume the proton branching ratio of the two levels to be the same). However, if all the events in the 6.5-MeV peak cor-

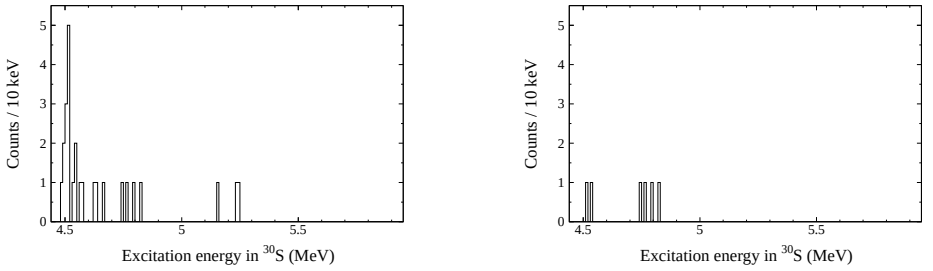

Figure 6.11: (a) The ^{30}S excitation spectrum calculated from multiplicity-two events, where one of the protons has an energy in the interval $[6800, 7160]$ keV corresponding to the decay of the IAS to the 4689-keV level and the 4809-keV level in ^{30}S. (b) The same spectrum as (a) reduced by demanding that the Q_{2p} of the two protons correspond to the decay of the IAS to the ground state of ^{29}P, i.e. belong to the 7.6-MeV peak in Figure 5.2.

responds to decays from the IAS to these two levels we would expect to see approximately three times as many events in our ^{30}S spectrum. This implies that there might be a background from other transitions to the events in the 6.5-MeV peak.

We now return to the protons in the 7-MeV peak, which should populate the 4689-keV level and the 4809-keV level. The 4689-keV level decays primarily trough gamma transitions as can be seen from using the Γ_γ/Γ_p ratios from Table 6.2. If all the protons in the 7-MeV peak corresponds to decays of the IAS and the ratio between the feeding of the two levels is $1.25(11)$ % deduced from Figure 6.9b, then we would expect to see less than 0.2 events in the two-proton spectrum. We do not see any events around 4689 keV in Figure 6.11b in full agreement with this. The 4809-keV level is expected to have a significant proton branching ratio. Using the value for Γ_γ/Γ_p from Ref. [Ric13] and the same assumptions as above, we would expect to see $19(3)$ events (Using the value from Ref. [Set13] gives $27(4)$). However, as indicated by the analysis of the 6.5-MeV peak, there might be contributions to the 7-MeV peak from other proton-transitions than the IAS decay. Nonetheless, even with a significant background contribution to the 7-MeV peak, we would still expect to have more than the 4 events seen in Figure 6.11b. This suggest that the

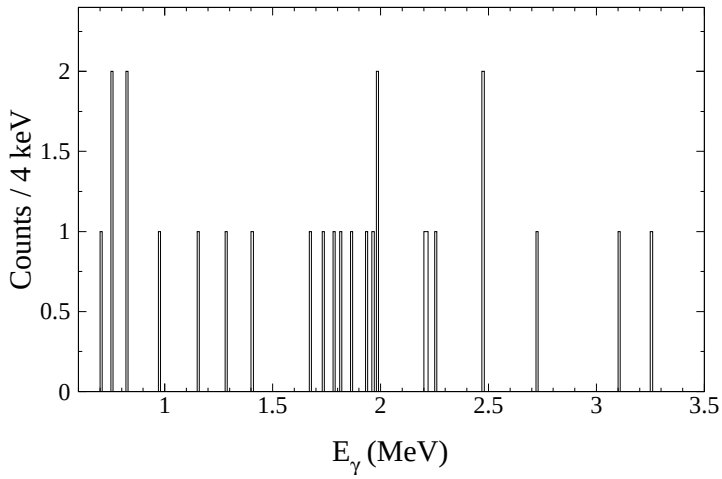

Figure 6.12: The gamma spectrum gated on protons with an energy in the interval $[6800, 7160]\,\mathrm{keV}$ corresponding to the decay of the IAS to the 4689-keV level and the 4809-keV level in ^{30}S.

proton branching ratio of the 4809-keV level is lower than what is currently expected from calculations. Since this level has the strongest influence on the $^{29}\mathrm{P}(p,\gamma)^{30}\mathrm{S}$ reaction rate, this issue should be further examined by experiments.

To test that the protons from the 7-MeV peak in Figure 6.9a do populate the levels in ^{30}S at 4689-keV and $4809\,\mathrm{keV}$ we study the gamma spectrum gated on these protons shown in Figure 6.12. Lotay *et al.* [Lot12] have identified two gamma transitions from the 4689-keV level with energies $1283.4(3)\,\mathrm{keV}$ and $2477.4(1)\,\mathrm{keV}$. We identify 1 event in Figure 6.12 in the bin with centre at $1285\,\mathrm{keV}$ and 2 events in the bin at $2475\,\mathrm{keV}$. This is in perfect agreement with the expected number of $0.44(6)$ and $1.62(23)$, respectively (using the same assumptions as for the two-proton events). The gamma decay of the 4809-keV level have energies $1404.5(1)\,\mathrm{keV}$ and $2598.6(1)\,\mathrm{keV}$ [Lot12]. We identify 1 event in Figure 6.12 in the bin with centre at $1405\,\mathrm{keV}$, but there are no events around $2599\,\mathrm{keV}$. We would expect $1.79(24)b_\gamma$ and $1.16(16)b_\gamma$ events at the two energies, respectively, where b_γ is the total gamma branching ratio for the level. Even with a gamma branching ratio of almost 1 our observation does not contradict this with any statistical significance. The observation of three out of four expected gamma transitions strongly support the hypothesis that

the 7-MeV peak in Figure 6.9a contain protons from the decay of the IAS to the levels in ^{30}S at 4689-keV and 4809 keV.

6.3 Spin determination

As discussed in the previous section and in Section 2.2.3, there are some disagreements in the spin assignment of the levels just above the proton threshold. The proton-proton angular correlations in a beta-delayed two-proton decays will depend on spin. By exploiting this we have developed a new method for determining the spin of a level by looking at beta-delayed two-proton decays going through the level. The distribution of angles Θ_{2p} between the two protons can be written as [Bie53]

$$W(\cos\Theta_{2p}) = \sum_{k=0}^{k_{\max}} A_k P_k(\cos\Theta_{2p}), \tag{6.3}$$

where P_k is the kth Legendre Polynomial and the sum extends to

$$k_{\max} = \min(2l_1, 2l_2, 2j), \tag{6.4}$$

so that we obtain an isotropic distribution if the angular momenta involved are small. Here j_1 (l_1) and j_2 (l_1) are the spin (orbital angular momentum) of the first and second emitted proton, respectively, and j is the spin of the ^{30}S state coupled with the first proton. The coefficient A_k is given by

$$A_k = F_k(l_1, j_1, j)\, b_k(l_1, l_1)\, F_k(l_2, j_2, j)\, b_k(l_2, l_2) \tag{6.5}$$

with

$$b_k(l, l') = \frac{2\sqrt{l(l+1)l'(l'+1)}}{l(l+1) + l'(l'+1) - k(k+1)}, \tag{6.6}$$

where F_k can be found from Ref. [Bie53].

Since the protons in the highest energy states in ^{31}Ar are in the $2s$ or $1d$ shells, we expect that the excess protons emitted in the beta-delayed two-proton decay are mainly in the sd-shell. Thus we will assume that only positive parity states in ^{30}S are populated and the sum in Eq. (6.3) can be restricted to even k. The possible values for A_2 in the decay are given in Table 6.3. In many cases there are two possible values for j and the table indicates the range spanned by the two extreme situations in which only one j value contributes.

Table 6.3: The A_2 coefficients for two-proton transitions calculated for the different initial states, J_i^π, (in ^{31}Cl) through five positive parity states, J_m^π, (in ^{30}S) to a $\frac{1}{2}^+$ final state (ground state of ^{29}P) using Eqs. (6.3)-(6.6).

J_m^π \ J_i^π	$\frac{3}{2}^+$	$\frac{5}{2}^+$	$\frac{7}{2}^+$
0^+	0	0	0
1^+	0	0	0
2^+	0	0	$[-0.70; -0.25]$
3^+	$[0.15; 0.87]$	0	0
4^+	$[0.76; 1.00]$	$[0.13; 0.95]$	0

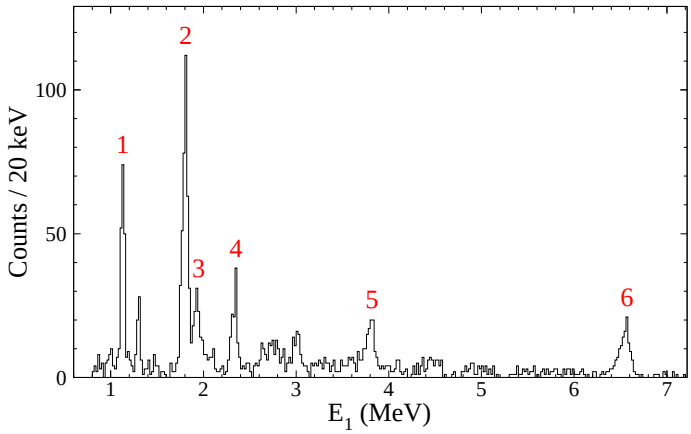

Figure 6.13: Energy of the first particle for transitions going through the 5227-keV level in ^{30}S. The peaks containing most counts are marked by numbers.

6.3.1 The 5227-keV level

To use this method, transitions from distinct levels in ^{31}Cl must be identified with sufficient statistics. This is only possible for the strongest fed level in ^{30}S at 5227 keV. As mentioned in Section 6.2.2, this level has previously been assigned 0^+ [Set13], but has also been identified as a 3^+ state due to its gamma decay [Lot12]. To have as much statistics as possible we include all detectors

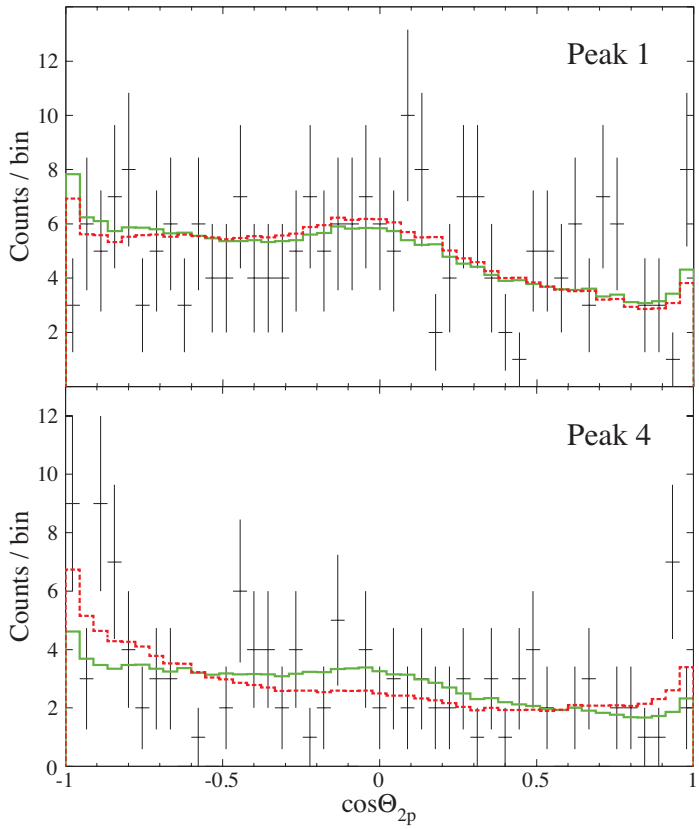

Figure 6.14: Angular distributions of the two proton events forming peak 1 and 4 in Figure 6.13 compared to the corresponding fitted two-proton simulations for either isotropic (green solid distribution) or non-isotropic (red dashed distribution) distributions. For better visualisation they are here shown using 45 bins, while the fits are made using 90 bins.

as for the data presented in Section 5.2. The energy of the first particle (the one with the highest energy) of the events passing through the 5227-keV level is shown in Figure 6.13. Each peak corresponds to population of the 5227-keV level from specific states in ^{31}Cl. The most significant peaks are numbered and are used in the following analysis. In Figure 6.14 the angular correlation for two of the peaks is shown with the corresponding fit to the two-proton simulations for either isotropic (A_0 only) or non-isotropic (A_0 and A_2) distributions. The simulated distributions are fitted to the data for all numbered peaks of Figure 6.13 with and without an A_2 term. The resulting A_2 values are shown in Table 6.4 along with the difference in χ^2 for the two fits. We have also tried to include the A_4 term, but this did not change the value of A_2 significantly for any of the peaks. Also shown in Table 6.4 are the results of a Kolmogorov test for a comparison between the data and a uniform distribution. The original Kolmogorov test is performed by finding the maximum difference in the cumulative distributions $F_{\max}$ and multiplying this with the square root of the total number of values N. However, the critical values differ for small N so we use a modified version of the Kolmogorov test from Ref. [D'A86],

$$D = \left(\sqrt{N} + 0.12 + \frac{0.11}{\sqrt{N}} \right) \cdot F_{\max}. \tag{6.7}$$

In this formula the critical values are independent of N. If the value of D is below 1, we can assume that the two distributions are most likely drawn from the same distribution, i.e. the data agree with being from a uniform distribution. If $D > 1.36$ then we can conclude the data are not uniform with 95% confidence.

Both the χ^2 difference and the Kolmogorov test indicate that the events in peak 1, 5 and 6 are consistent with being uniform. The conclusion for peaks 2 and 3 is less clear: The Kolmogorov test shows with $95\,\%$ confidence [D'A86] that the events in peak 2 are not consistent with a uniform distribution, but the deviations do not correspond to a standard angular correlation shape since the fit does not give a value for A_2 that is significantly different from 0 (including an A_4 term does not change this). The fit for the events of peak 3 points to an A_2 parameter different from 0, but the Kolmogorov test does not find the distribution to be significantly different from uniform. Finally, the events of peak 4 have a distribution significantly different from uniform with more

Table 6.4: The A_2 coefficients for different two-proton transitions from ^{31}Cl through the 5.2-MeV level in ^{30}S together with the difference in χ^2 compared to a uniform fit and the result D of a Kolmogorov test to a uniform distribution. The peak numbers correspond to Figure 6.13.

Peak	$E(^{31}\mathrm{Cl})$ (keV)	A_2	$\Delta\chi^2$	D
1	6674(6)	−0.12(14)	0.67	0.95
2	7380(6)	0.16(11)	1.97	1.37
3	7512(7)	0.35(19)	3.51	0.76
4	7919(8)	0.48(19)	6.69	1.21
5	9434(9)	0.04(19)	0.05	0.58
6 (IAS)	12313(4)	0.03(18)	0.03	0.80
All		0.18(5)	13.18	1.19

than $85\,\%$ confidence [D'A86] using the Kolmogorov test and the value for A_2 differs from 0 with more than two standard deviations. This is also the case if all events of the 5227-keV peak are considered, which implies that there must be components that are non-uniform. With reference to Table 6.3 this excludes that the level is a pure 0^+ or 1^+ level. Spin 2^+ is also excluded because it can only give deviations towards negative A_2 values.

The spin of the states in ^{31}Cl corresponding to the numbered peaks in Figure 6.13 are only known for the case of the IAS (peak 6), where it is $\frac{5}{2}^+$. The other observed states can be either $\frac{3}{2}^+$, $\frac{5}{2}^+$ or $\frac{7}{2}^+$ assuming that only allowed beta decays are populated. The A_2 value for the IAS indicates a uniform distribution. By comparing the value of A_2 with the values in Table 6.3 we can conclude that the 5227-keV level in ^{30}S has spin 0–3^+, while the 4^+ assignment is less likely. By comparing the value of A_2 for peak 4 with Table 6.3 we can only conclude that this peak originates from a $\frac{3}{2}^+$ or $\frac{5}{2}^+$ level in ^{31}Cl. If peak 4 corresponds to a $\frac{5}{2}^+$ level the spin of the ^{30}S level must be 4^+, and if it is a $\frac{3}{2}^+$ level it is most likely a 3^+ while 4^+ is possible but again less likely. Considering in a similar way all the data in Table 6.4, the preferred value for the spin of the 5227-keV level is 3^+, because several of peaks 1–6 give a uniform distribution, which for the 3^+ level would be consistent with both $\frac{5}{2}^+$ and $\frac{7}{2}^+$ levels in ^{31}Cl. One would expect at least one of the peaks 1–6 to originate from

a $\frac{3}{2}^+$ level in ^{31}Cl and therefore a 4^+ assignment of the 5227-keV level would produce an angular correlation significantly different from uniform. However, we cannot exclude that the 5227-keV level measured is an unresolved doublet, and we can thus only conclude that it has a component with either spin 3^+ or 4^+.

We can compare the measured spins of the levels in ^{30}S with the spins of the levels of the stable mirror nucleus ^{30}Si which are very reliable. We do this using Figure 2.2 and see that there is a systematic energy shift, which is less than about $250\,\mathrm{keV}$ relative to the ground state. This means that the only possible spin is 3^+, 4^+, 0^+ and perhaps 3^-. However, the 3^- lies a bit too high and has already been assigned to the $5313.6(14)$-keV level [Yok82], which is not populated in the decay of ^{31}Ar most likely due to the negative parity of the state. The spin of the $5132.1(1)$-keV level has been measured to be 4^+ [Lot12,Set13]. This leaves only the 3^+ and 0^+ and we thus conclude that the spin of the dominant level at 5227-keV feed in the beta-delayed proton decay of ^{31}Ar is 3^+. However, we cannot exclude that a 0^+ level with approximately the same energy is also populated. Lotay *et al.* have seen the gamma decay of a level with spin 3^+ at $5218.8(3)\,\mathrm{keV}$, which is significantly lower than what we measure. However, as we mention in Section 2.2.3 they may have underestimated their uncertainties. One reason for the energy of the level we measure to be higher than the one measured by Lotay *et al.* could be that a 0^+ level with an energy slightly higher than the 3^+ is also populated in the decay of ^{31}Ar. Comparing with the mirror nuclei we see that the 0^+ level here lies about $140\,\mathrm{keV}$ higher than the 3^+ level. If the same is the case for ^{30}S we would expect the 0^+ level to have an energy of about $5360\,\mathrm{keV}$. However, it is very unlikely that the energy of the 0^+ level is that high, because it was observed by Bardayan *et al.* in Ref. [Bar07] as a part of an unresolved doublet measured at $5168(6)\,\mathrm{keV}$, with the 4^+ $5132.1(1)$-keV level identified as the lower part. But the $8\,\mathrm{keV}$ energy difference between our measurement and the one made by Lotay *et al.* can be explained if for example $20\,\%$ of our peak is due to a 0^+ level $40\,\mathrm{keV}$ above the 3^+ level. We investigate this by gating on the upper and lower parts of the peak, but we do not find any significant difference in the angular distributions or in the energies of the particles feeding the state(s). However, with our limited statistics we cannot exclude that a 0^+ level is also populated. In Figure 6.10 we see a hint of a possible peak at $5.17\,\mathrm{MeV}$, but if

this is the 0^+ level, it would not explain the difference between the energy of our 5.2-MeV peak and the energy measured by Lotay *et al*.

6.4 The strong feeding of the 5227-keV level

The strong feeding of the 5227-keV level suggests that there is a strong overlap between the structure of this state and the structure of ^{31}Ar. The reason for this might be explained by a simple picture, where we consider ^{31}Ar to consist of a core of ^{30}Cl plus a $1d_{3/2}$ proton, as was done in Section 1.1.4. The beta operator $\hat{O}$ works on both terms:

$$\hat{O}_\beta \left|{}^{31}\text{Ar}\right\rangle = \hat{O}_\beta \left|{}^{30}\text{Cl} + \text{p}\right\rangle = \left(\hat{O}_\beta \left|{}^{30}\text{Cl}\right\rangle\right) |\text{p}\rangle + \left|{}^{30}\text{Cl}\right\rangle \left(\hat{O}_\beta |\text{p}\rangle\right). \tag{6.8}$$

However, from Eq. (1.19) we see that the largest part of the IAS comes from the Fermi decay of the ^{30}Cl core leaving the $1d_{3/2}$ proton untouched. Expanding upon this picture, we can assume that a major part of the beta-delayed proton decay of ^{31}Ar can be viewed as a beta decay of the ^{30}Cl core with a subsequent emission of the spectator proton. The levels populated in ^{30}S are thus determined by the beta decay of ^{30}Cl. A similar picture is used for neutron halos in Refs. [Nil00, Jon04] and it is shown successful in describing the beta decay of the two-neutron halo ^{14}Be by studying the beta decay of the ^{12}Be core.

Because ^{30}Cl is unbound we do not know its spin or how it decays. However, if we look at the mirror nucleus ^{30}Al, we see that the ground state has spin 3^+ and we can assume that this is also the case for ^{30}Cl. Following this reasoning we expect that a great part of the beta decay of ^{30}Cl, and thus a great deal of the beta-delayed proton decay of ^{31}Ar, will go to a 3^+ level in ^{30}S, which could be the level at $5227\,\text{keV}$.

We now look at the mirror process of the β^+ decay of ^{30}Cl, i.e. the β^- decay of ^{30}Al to ^{30}Si. This process is fairly well known since ^{30}Si is stable. Here the strongest transition is to the 2_2^+ state with a $\log ft$ value of $4.578(12)$ [Bas10]. This state corresponds to the 3405-keV level in ^{30}S and we would thus expect this level to be the strongest fed state in ^{30}S. From Table 6.1 we see that this is indeed the case given that its total branching ratio is $5.6(8)\,\%$ compared to a maximum of $4.6(17)\,\%$ for the first excited state (when subtracting contributions from gamma decays from higher lying levels). Three other

states in ^{30}Si are also strongly fed in the beta decay with $\log ft$ values around 5.0 [Alb74, Klo74]. This is the 2_3^+, 3_1^+ and 3_2^+ levels corresponding to the 4809-keV, 4689-keV and 5227-keV levels in ^{30}S, respectively. Thus we would also expect these three states to be strongly fed in the beta-delayed proton decay of ^{31}Ar. The total branching ratio to the 4689-keV level is about $1.4(4)\,\%$ (cf. Table 6.1 and 6.2) and it is $3.2(6)\,\%$ for the 5227-keV level, while the branching ratio to the 4809-keV level is unknown due to our detection efficiency.

Of course, we do not expect to see the exact same decay pattern as for the beta decay of the mirror nucleus ^{30}Al. Not just because the decay of ^{30}Cl will be different from the decay of ^{30}Al, but mainly due to deviations from the very simple picture of a decaying core and subsequent emission of the spectator proton. However, from this simple model we do get that a strong structure overlap between the ^{31}Ar ground state and the 5227-keV level in ^{30}S is very plausible, justifying a strong feeding to this level.

CHAPTER 7

New decay modes of ^{31}Ar

The beta-delayed three proton decay was recently discovered in the decay of ^{31}Ar [Pfü12a, Lis15]. The decay mode was found using an Optical Time Projection Chamber (OTPC), where the decay is seen directly, since it produces a picture of each event. However, the resolution of the OTPC is limited, especially in multi-particle events. A detailed spectroscopic analysis is thus not possible for the three-proton decay and it was not possible to determine the decay mechanism. Our setup had a very good energy and angular resolution and we can thus for the first time make a detailed spectroscopic analysis of the beta-delayed three-proton decay.

7.1 Beta-delayed three-proton spectroscopy

We start by considering all the three-particle events in the data. A spectrum of their Q_{3p} values can be seen in Figure 7.1. From the three-proton branching ratio from Ref. [Lis15] we would expect to see a total of $24(10)$ events, but our spectrum contains a total of 62 events. However, not all of the events are real three-proton events, some of them are most likely two protons detected in coincidence with a beta particle. To estimate the efficiency of detecting a beta particle in coincidence with a proton we study the decay of ^{33}Ar. Using the same analysis cut-offs as for protons, we can estimate this efficiency as the number of particles with an energy below $1.2\,\mathrm{MeV}$ (beta particles) detected in coincidence with a proton (in two-particle events) divided by the number of all protons detected (in single-particle events). To make sure that we gate on a real proton, we can demand that it should belong to one of the strong ^{33}Ar peaks. We do it for different peaks and the total ^{33}Ar spectrum, and estimate the efficiency of detecting a beta particle in coincidence with a proton to be $0.43(5)\,\%$. Using this efficiency and the measured number of two-proton we can deduce the expected number of events with a beta particle measured in

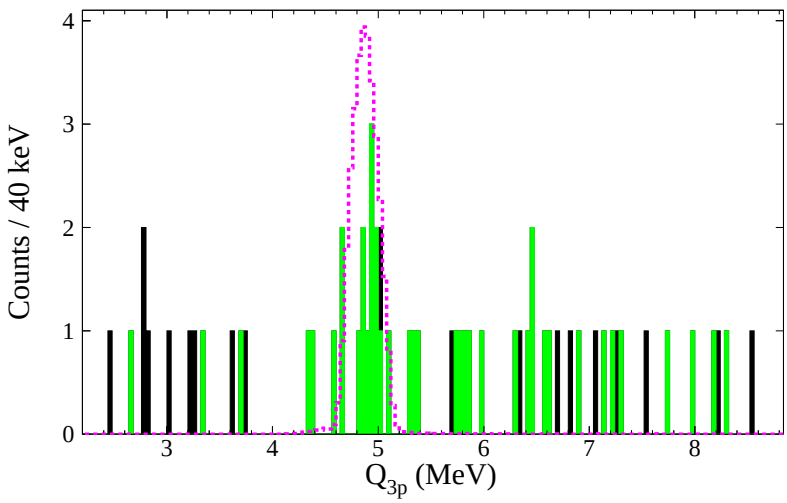

Figure 7.1: Q_{3p} for all three-particle events. The histogram (black and green) shows all the three-particle events detected in the experiment. To obtain the histogram in green, events that are most likely not real three-proton events were removed as described in the text. Only the events in the green histogram are used in the analysis of the three-proton decay presented in this thesis. The dashed histogram is a downscaled simulation of three-proton decays of the IAS in ^{31}Cl to the ground state in ^{28}Si.

coincidence with a two-proton event. We should expect 29(4) which is roughly half of the 62 three-particle events we measure. We can identify some of the events with a beta particle measured in coincidence with a two-proton event if the Q_{2p} value of two of the particles corresponds to one of the prominent two-proton transitions from the IAS to one of the three lowest states in ^{29}P as described in Section 5.2 and the energy of the last particle (assumed to be the beta particle) is less than $1.2\,\mathrm{MeV}$. Some of the three-particle events are all in the same detector, which implies that they are all signals from a scattered beta particle. Finally a few events have a too high Q_{3p} value so they cannot be true three-proton events. In this way 21 background events are identified and removed, and only the 41 remaining events are included in the following analysis. These events are shown as the green histogram in Figure 7.1.

Around $4.89(29)\,\mathrm{MeV}$ we see a peak containing 19 events between $4.3\,\mathrm{MeV}$ and $5.5\,\mathrm{MeV}$. It is most likely attributable to the three-proton decay of the IAS,

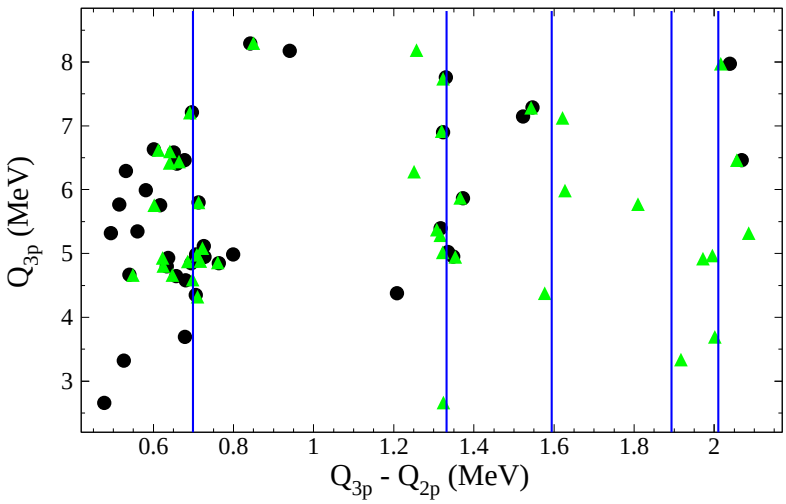

Figure 7.2: Q_{3p} plotted against $Q_{3p} - Q_{2p}$ for the three-proton events. The lines indicate the levels in ^{29}P ($Q_{3p} - Q_{2p} = E(^{29}\mathrm{P}) - S_{p3}$). For the black circles Q_{2p} is calculated assuming that the first two particles are the ones with the highest energy and for the green triangles it is calculated as a best fit to the five levels in ^{29}P shown.

because it corresponds to a ^{31}Cl level at an energy of $12.32(29)\,\mathrm{MeV}$. To investigate the spread in Q_{3p} owing to detection resolution we simulate the three-proton decay from the IAS to the ground state of ^{28}Si. The result is downscaled and included in Figure 7.1. The full width at half maximum (FWHM) for the three-proton events is approximately $0.3\,\mathrm{MeV}$. This is mainly due to the reconstruction of the energy of the recoiling ^{28}Si nucleus, because the resolution for detection of individual protons is $0.05\,\mathrm{MeV}$ FWHM. It is interesting to notice that it is only approximately half of the three-proton events that belong to the decay of the IAS. The remainder are interpreted as coming from levels in ^{31}Cl with excitation energies mainly above the IAS. This implies that there is a contribution to the Gamow-Teller strength, which needs to be extracted by a detailed analysis of the beta-delayed three-proton events. This enables for the first time the inclusion of this decay mode in the determination of the Gamow-Teller distribution, which is done in Section 8.2.

The mechanism of the beta-delayed three-proton emission from the previously studied nuclei has not been determined. If sequential emission occurs in

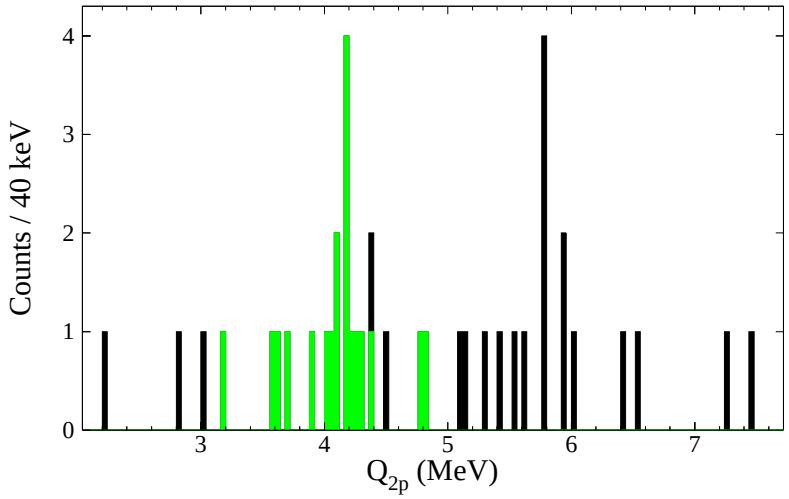

Figure 7.3: Q_{2p} calculated from the two particles with highest energy of the three-particles events in the green histogram of Figure 7.1. The green part of the histogram here is the Q_{2p} from the 19 events around $4.84(29)\,\mathrm{MeV}$ from that histogram.

the case of ^{31}Ar, it should be possible to identify the known levels in both ^{30}S and ^{29}P from the energies of the protons. However, owing to limited statistics and the considerable level density for high excitation energies in ^{30}S, it will not be possible to do the same for ^{30}S. If the decay goes through levels in ^{29}P, we can identify these via the difference between the Q_{3p} value and the Q_{2p} value. This is the $Q_{3p} - Q_{2p}$ difference corresponds to the energy of the level populated in ^{29}P minus the proton separation energy. The reason for using the two Q values is that these can be extracted directly from the experimental data and that a correction for the recoil of the daughter nucleus is included. The Q_{3p} value can be calculated independently of the decay mechanism, while for the Q_{2p} value we must choose which particles should be considered to be the first two in the decay. In Figure 7.2 this difference is plotted for two different choices together with lines indicating the levels in ^{29}P. For the black dots it is assumed that the first two particles are the ones with the highest energy. This is, however, not necessarily a reasonable assumption for all the events. Instead the first two particles can be chosen such that the difference between the Q_{3p} and Q_{2p} value fits the known levels in ^{29}P (only the first five levels

are included). This choice is plotted as the green triangles. This analysis suggests that the three-proton emission is consistent with being fully sequential, but owing to the large expected spread in the Q_{3p} value, a considerable contribution from simultaneous emission cannot be excluded. When the energy of all three particles are above $1.2\,\mathrm{MeV}$, they are most likely all protons, but the density of states in ^{29}P is then so high that it is easy to interpret a simultaneous decay as a sequential decay. This is not a problem for the $\frac{7}{2}^-$ level at $3447.6(4)\,\mathrm{keV}$, which corresponds to a $Q_{3p} - Q_{2p}$ difference of $699\,\mathrm{keV}$. The problem with this is that one of the particles has an energy around $0.7\,\mathrm{MeV}$ and it is thus difficult to distinguish protons from beta particles. As shown in Figure 7.1 the majority of these events originate from the peak in the Q_{3p} spectrum around $4.89(29)\,\mathrm{MeV}$ and they most likely belong to the decay of the IAS. Their Q_{2p} value can be seen in Figure 7.3, which shows that more than half of them lie around an energy of $4.14(13)\,\mathrm{MeV}$. Assuming they go through the $3447.6(4)$-keV level in ^{29}P, this corresponds to a ^{31}Cl energy at $12.27(13)\,\mathrm{MeV}$ in complete agreement with the value of $12.32(29)\,\mathrm{MeV}$ from the Q_{3p} value. These events cannot be beta particles in coincidence with two-proton events; if they were, one would expect more than 2×10^3 events at this energy in the Q_{2p} spectrum made from two-proton events. While there are indications of small peaks around this energy, they contain less than 70 events. The IAS three-proton decay can thus be assigned partly to go through the level at $3447.6(4)\,\mathrm{keV}$ in ^{29}P. This supports the assumption that the events lying close to $699\,\mathrm{keV}$ in Figure 7.2 are also events going through this level.

We have also strong indications of events going through the level with energy $4080.5(3)\,\mathrm{keV}$ corresponding to a $Q_{3p} - Q_{2p}$ difference of $1332\,\mathrm{keV}$. However, this is not conclusive due to the limited statistics available here and the expected large spread in the Q_{3p} value. The sparsity of events with $Q_{3p} - Q_{2p}$ between $0.9\,\mathrm{MeV}$ and $1.1\,\mathrm{MeV}$ is a strong indication that there are no simultaneous three-proton decays with a low-energy proton.

Our choice of energy cut-offs (the lowest energy particle must have an energy above $500\,\mathrm{keV}$) means that we cannot study three-proton decays going through the $3105.9(3)$-keV $\frac{5}{2}^+$ level in ^{29}P since it is only $357\,\mathrm{keV}$ above the proton threshold. However, the penetrability of this level is roughly a factor of 25 below the penetrability of the $\frac{7}{2}^-$ level at $3447.6(4)$-keV, which implies that the $3105.9(3)$-keV level will mainly decay by gamma emission.

To further examine this we will consider the resonance strengths, $(\omega\gamma) = (2J+1)\frac{\Gamma_p\Gamma_\gamma}{\Gamma}$, and the lifetimes, $\tau = \hbar/\Gamma$, of the two levels. These have been measured and their values can be found in Ref. [Bas12]. Since the total width Γ is just the sum of the partial widths, we obtain a quadratic equation

$$0 = \widetilde{\Gamma}^2 - \frac{\hbar}{\tau}\widetilde{\Gamma} + \frac{\hbar(\omega\gamma)}{\tau(2J+1)}, \tag{7.1}$$

which is fulfilled for $\widetilde{\Gamma} = \Gamma_p$ and $\widetilde{\Gamma} = \Gamma_\gamma$. Solving this gives us $\Gamma \sim \Gamma_{\text{max}} = 51(31)\,\text{meV}$ and $\Gamma_{\text{min}} = 0.038(10)\,\text{meV}$ for the $\frac{7}{2}^-$ level, where Γ_{max} (Γ_{min}) refers to the largest (smallest) width of Γ_p and Γ_γ. For the $\frac{5}{2}^+$ level we find $\Gamma \sim \Gamma_{\text{max}} = 19(9)\,\text{meV}$ and $\Gamma_{\text{min}} = 0.46(11)\,\text{meV}$. If $\Gamma_{\text{max}} = \Gamma_\gamma$ for the $\frac{7}{2}^-$ level, we would expect to see around 700 gamma rays at $1493.6\,\text{keV}$, corresponding to the decay of this level to the second excited level, when gating on two protons. This we do not observe in our two-proton-gated gamma spectrum, see Section 7.2 and Figure 7.4. We therefore conclude that $\Gamma_p = \Gamma_{\text{max}}$.

Looking now at the mirror nucleus ^{29}Si, where the $\frac{7}{2}^-$ and $\frac{5}{2}^+$ levels both lie below the proton threshold, we see that the half-lives of these two levels are $2.63(9)\,\text{ps}$ and $33(1)\,\text{fs}$, respectively. The half-lives of the two levels in ^{29}P are $9(6)\,\text{fs}$ and $23(10)\,\text{fs}$, respectively. By comparison it is reasonable to assume that $\Gamma_p = \Gamma_{\text{max}}$ for the $\frac{7}{2}^-$ level, as deduced above, since the large difference in half-lives implies that there is a large contribution from another decay channel for the level in ^{29}P. Since the half-lives for the $\frac{5}{2}^+$ levels are of the same order of magnitude, it is reasonable to assume that $\Gamma_p = \Gamma_{\text{min}}$ for this level in ^{29}P. From this reasoning we find that the proton width of the $\frac{5}{2}^+$ level is $111(72)$ times smaller than the proton width of the $\frac{7}{2}^-$ level and it is thus reasonable to assume that the three-proton decay through the $\frac{5}{2}^+$ level is suppressed.

7.2 Beta-delayed two-proton-gamma decay

The indications of a sequential three-proton branch imply that the decay populates higher-lying levels in ^{29}P than previously found. With our setup it was possible to detect gamma rays in coincidence with protons and we thus have a chance to see the gamma transitions from these levels. However, the detection efficiency is limited and the chance of detecting the gamma ray in coincidence with both the emitted protons is thus very small. For a real two-proton-gamma event it is $2/\varepsilon_p = 4.6(2)$ times more likely to detect it as a

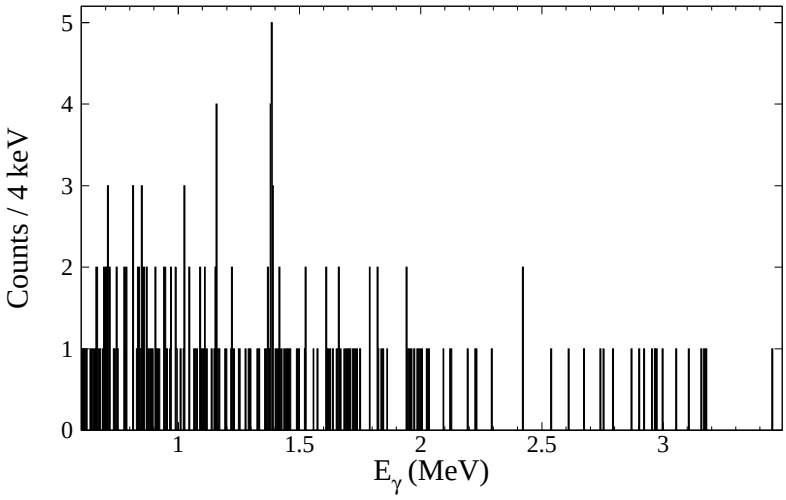

Figure 7.4: The gamma spectrum gated on two protons.

proton-gamma event than to detect it as a two-proton-gamma event. Thus we initially search for the transitions from higher-lying levels in ^{29}P in the one-proton gated gamma spectrum, which is shown in Figure 6.2a. In this spectrum clear peaks are identified from the lowest states of both ^{29}P and ^{30}S as discussed in Section 6.1, but owing to background events in the spectrum there is no clear signal of levels above the second excited state in ^{29}P. In Figure 7.4 the two-proton gated gamma spectrum is shown. In the following we will consider all the levels in ^{29}P up to $4.1\,\mathrm{MeV}$ and compare the number of two-proton-gamma events with what is expected from the one-proton gated gamma spectrum.

The first excited state in ^{29}P ($\frac{3}{2}^+$) is at $1383.55(7)\,\mathrm{keV}$ [Bas12]. The corresponding peak is clearly seen in both the one- and two-proton-gated gamma spectra. There are $64(11)$ events above background in the one-proton-gated spectrum. This implies that there should be $14(2)$ events in the two-proton-gated spectrum, which agrees very well with the $13(4)$ measured above background.

The second excited state in ^{29}P ($\frac{5}{2}^+$) is at $1953.91(17)\,\mathrm{keV}$, and it decays primarily to the ground state. A peak at this energy is seen in the one-proton-gated gamma spectrum. It contains $29(11)$ events and we thus expect $6.3(24)$ in the two-proton-gated spectrum, which again agrees very well with the $7(3)$

events in total found in the spectrum.

The third excited state is a $\frac{3}{2}^+$ state at $2422.7(3)\,\mathrm{keV}$. The primary gamma-decay of this state also goes to the ground state. There is no significant signal above background in the one-proton-gated gamma spectrum at this energy. In the two-proton-gated spectrum there are two events with no significant background at $2422(11)\,\mathrm{keV}$. This would imply $9(7)$ events in the one-proton-gated spectrum, which is consistent with the data.

The next level is the $3105.9(3)$-keV level which is just above the proton threshold. As mentioned in the previous section, it is a $\frac{5}{2}^+$ level and it decays primarily by a 1722.2-keV gamma-ray. Again there is no significant signal above background in the one-proton-gated spectrum. There are a maximum of $14(9)$ events above background, which implies there should be $3(2)$ events in the two-proton-gated spectrum where we find a total of 2.

The $\frac{7}{2}^-$ level at $3447.6(4)\,\mathrm{keV}$ was identified in the three-proton decay. Its primary gamma decay is to the second excited state in ^{29}P by a $1493.6\,\mathrm{keV}$ gamma ray. There is a hint of a peak in the one-proton-gated gamma spectrum at this energy containing $14(7)$ events. From this we expect $3.0(15)$ events in the two-proton-gated spectrum, where we observe a total of 2.

The level at $4080.5(3)\,\mathrm{keV}$ is a $\frac{7}{2}^+$ level, and it decays primarily to the second excited state by a $2126.3\,\mathrm{keV}$ gamma ray. In the one-proton-gated gamma spectrum, there are no indications of a peak at this energy. There are $5(5)$ events, which means that there should be $1(1)$ event in the two-proton-gated spectrum and there is a total of 2 events.

In summary, the gamma decays observed for the six lowest levels in ^{29}P give consistent results for the one- and two-proton-gated gamma spectra, but only the feeding of the lowest two can be seen directly in the gamma spectra.

CHAPTER 8

Determination of the beta-strength

The beta-strength cannot be measured from the neutrinos and beta particles with our setup. Instead we deduce it by considering the decay of the levels in ^{31}Cl fed in the beta-decay. If we measure all the particles in a decay and know the final state, we can calculate the initial state in ^{31}Cl. This makes it possible to find the branching ratios for feeding the different levels in ^{31}Cl in the beta decay. With our improved resolution and the addition of the beta-delayed three-proton branch we are now able to make a much better determination of the beta-strength. Furthermore, the addition of the three-proton branch makes it possible to identify an evolution of decay modes in ^{31}Cl and outline a simple model for proton emission, which we use to predict branching ratios for beta-delayed one-, two- and three-proton emission for two other nuclei in the last section of this chapter.

8.1 The Fermi-strength

The Fermi strength of the beta-decay of ^{31}Ar was previously measured by considering the one- and two-proton decays of the IAS to the lowest states in ^{30}S and ^{29}P [Fyn00]. However, as shown in Chapter 7, there are additional contributions. In addition to the three-proton channel, all the levels up to the vicinity of the proton threshold should, in principle, be included for the one- and two-proton channels. To get an accurate determination of the branching ratios for the different channels, it is important to have a good energy resolution and to know the total number of ^{31}Ar collected as well as the detection efficiency. For this reason only the $300\,\mu$m DSSSDs with backing are selected for this analysis. Out of these detector 2 had several broken strips

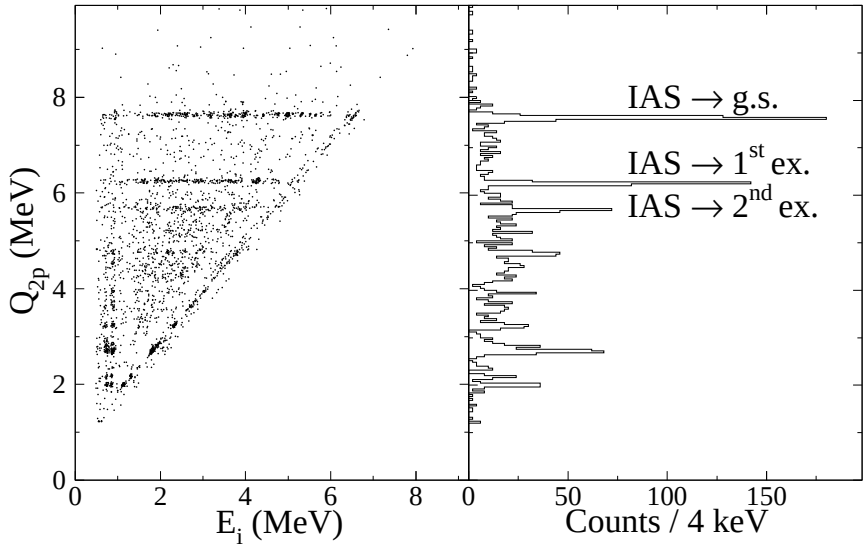

Figure 8.1: Two-proton spectrum constructed using only detector 3 and 6 with a lower energy cut-off of $E > 500\,\mathrm{keV}$ for both protons. Left: Q_{2p} plotted against the energy of the two particles. Right: The projection onto the Q_{2p} axis.

and less accurate efficiency determination owing to shading from the target holder. This leaves only detectors 3 and 6, which are used to determine the branching ratios for the one- and two-proton decays in the following. The statistics is so low for the three-proton decay that all the detectors are needed, and the branching ratio is thus found using the data presented in Chapter 7. The branching ratio for the three-proton decay to the ground state of ^{28}Si is found to be $0.040(20)\,\%$, which is consistent with the $99\,\%$ confidence upper limit of $0.11\,\%$ found by Fynbo *et al.* [Fyn99].

The two-proton spectrum using only detector 3 and 6 can be seen in Figure 8.1. For this spectrum we use a lower energy cut-off of $500\,\mathrm{keV}$ for both protons. The peaks corresponding to the decay to the ground state and the first and the second excited state of ^{29}P are clearly visible in the spectrum at Q_{2p} values of $7.6\,\mathrm{MeV}$, $6.3\,\mathrm{MeV}$ and $5.7\,\mathrm{MeV}$. There may also be a peak at $5.2\,\mathrm{MeV}$ corresponding to the transition to the third excited state in ^{29}P. The branching ratios for these levels are listed in Table 8.1, while transitions to

Table 8.1: Branching ratios for the decay of the IAS. The ^{31}Cl-energies are found using the masses from [Wan12] and a proton separation energy for ^{31}Cl of $282.8(44)\,\mathrm{keV}$ [Saa11]. The decays written in *italic* correspond to decays not uniquely identified in the spectra: There are some indications that the two-proton branch and the one-proton branches cannot be uniquely assigned to levels in ^{30}S. The total branching ratio is quoted with and without these decays. The efficiencies used are different for each of the three decay modes and the uncertainties from these are included for each decay. The correlation is taken into account for the uncertainty on the total branching ratio. Furthermore, there is a systematic error of $3.8\,\%$ originating from the normalisation (cf. Section 4.1.4), which is not included in the uncertainties.

Three-proton branch				
Final state in ^{28}Si (keV)	J^π	Q_{3p} (MeV)	E_{IAS} (MeV)	B.R. (%)
0	0^+	4.89(29)	12.32(29)	0.040(20)
Two-proton branch				
Final state in ^{29}P (keV)	J^π	Q_{2p} (MeV)	E_{IAS} (MeV)	B.R. (%)
0	$\frac{1}{2}^+$	7.633(4)	12.311(6)	1.45(17)
1383.55(7)	$\frac{3}{2}^+$	6.251(4)	12.313(6)	0.87(12)
1953.91(17)	$\frac{5}{2}^+$	5.688(6)	12.320(8)	0.39(9)
2422.7(3)	$\frac{3}{2}^+$	*5.22(8)*	*12.32(8)*	*0.07(4)*
One-proton branch				
Final state in ^{30}S (keV)	J^π	E_p (MeV)	E_{IAS} (MeV)	B.R. (%)
0	0^+	11.57(8)	12.24(8)	0.048(11)
2210.2(1)	2^+	9.46(8)	12.27(8)	0.104(17)
3404.1(1)	2^+	8.33(8)	12.30(8)	0.108(17)
3667.7(3)	*0*$^+$	*8.08(8)*	*12.30(8)*	*0.109(19)*
3677.0(3)	*1*$^+$		*12.31(8)*	
4687.7(2)	*3*$^+$	*7.01(8)*	*12.22(8)*	*0.36(3)*
4809.0(3)	*2*$^+$		*12.34(8)*	
Total			12.313(4)	3.01(28)
Total				*3.56(29)*

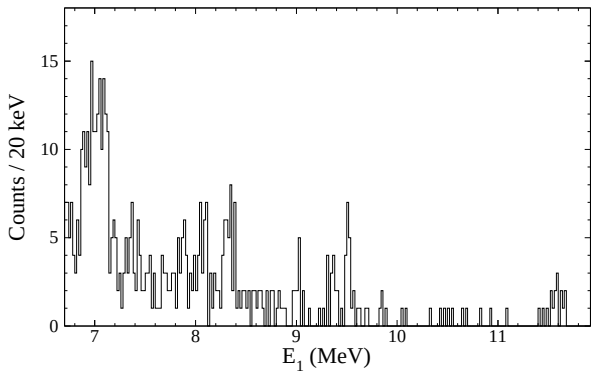

(a)

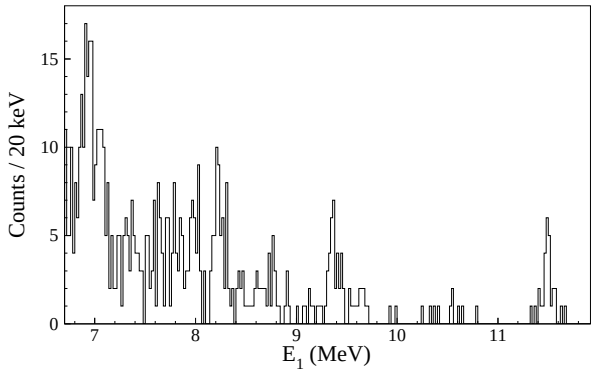

(b)

Figure 8.2: The one-proton energy spectrum for detector 3 (a) and 6 (b) for high energies.

higher-lying states cannot be identified. The branching ratios are systematically lower than those reported by Fynbo *et al.* [Fyn00], which is mainly due to an improvement in energy and angular for this energy range. The peaks of Ref. [Fyn00] were wider so they included contributions from decays with Q_{2p} values close to those for the IAS decays. Furthermore, for the decays to excited states in ^{29}P, the background from Gamow-Teller transitions is estimated and subtracted here, which was not done in Ref. [Fyn00].

In Figure 8.2 we show the one-proton energy spectrum for detector 3 and 6. Note that the energy measured in detector 6 is slightly lower than in detector 3. This is most likely due to an inaccurate calibration or dead layer es-

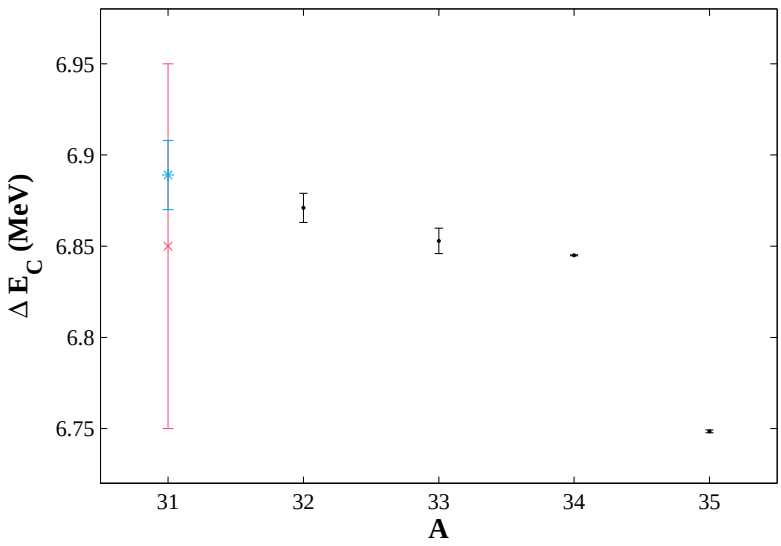

Figure 8.3: The Coulomb displacement energy of argon isotopes. For $^{32–35}$Ar (black dots) it is extracted from Ref. [Lam13]. The blue asterix is obtained from extrapolation of $^{32–34}$Ar and the red x is the value chosen here.

timation of the pad detector behind DSSSD 6. We therefore extract the branching ratios for detector 3 and 6 separately. The efficiency is found for each transition by simulating 10^6 one-proton events to the given level in ^{30}S. The branching ratio is then chosen as the average of the branching ratios found from detector 3 and 6 and is given in Table 8.1. The proton energy is chosen as the energy deposited in detector 3. The large uncertainty in the energy is attributable to limited statistics and a large uncertainty in the calibration of the back detectors for high proton energies. Because the lower energy cut-off of the two-proton spectra is $500\,\mathrm{keV}$, the branching ratios are found up to the ^{30}S level at $4809.0(3)\,\mathrm{keV}$ ($413\,\mathrm{keV}$ above the proton threshold) in the one-proton spectrum. The peaks at $8.1\,\mathrm{MeV}$ and $7.0\,\mathrm{MeV}$ cannot be separated into two components, even though they should both contain contributions from decays to two different levels in ^{30}S. The branching ratios are thus found for the total contribution from the two levels.

The total theoretical branching ratio, b_F can be found using Eq. (1.14). As described in Section 1.1.2 we will need the Q value for electron capture Q_{EC}

for ^{31}Ar. This can be found using Eq. (1.6), which gives $Q_{\mathrm{EC}} = 18.36(21)\,\mathrm{MeV}$. However, the uncertainty is relatively large and it would thus be favourable to find a better estimate. This can be done using the Coulomb displacement energy ΔE_{C} as was done in Ref. [Axe98b]. ΔE_{C} can be found from the Coulomb displacement energy of $^{32\text{–}34}$Ar extracted from Ref. [Lam13] and extrapolated using the relation $k_1 \frac{\bar{Z}}{A^{1/3}} + k_2$ [Ant84], where $\bar{Z}$ is the mean charge of the two isobaric analogue states. We obtain $\Delta E_{\mathrm{C}} = 6.889(19)\,\mathrm{MeV}$. However, as seen in Figure 8.3, ΔE_{C} for ^{35}Ar lies much lower than for $^{32\text{–}34}$Ar, and we should thus be careful using this extrapolation. Furthermore, when moving towards the drip-line the proton separation energy decreases, making the last proton more and more unbound. The proton in ^{31}Ar is very loosely-bound ($S_p = 440(280)\,\mathrm{keV}$), which means it can tunnel far out of the nucleus, and since $E_C \sim \frac{Ze^2}{r}$, this reduces its Coulomb interaction. This effect is known as the Thomas-Ehrman effect and means that we will expect the ΔE_{C} for ^{31}Ar to be lowered compared to ^{32,33}Ar. But since we cannot know by how much, we choose the Coulomb displacement for ^{31}Ar to be equal to the one for ^{34}Ar, but with a large uncertainty of $100\,\mathrm{keV}$, i.e. $\Delta E_{\mathrm{C}} = 6.85(10)\,\mathrm{MeV}$. Notice that the value obtained from extrapolation is fully included in this, see Figure 8.3. Using the energy of the IAS found here (see Table 8.1) we then obtain $Q_{\mathrm{EC}} = 18.38(10)\,\mathrm{MeV}$.

Using our improved half-life of ^{31}Ar (see Section 5.5) and neglecting isospin symmetry breaking (i.e. $B_F = 5$, see Section 1.1.3), we obtain a total theoretical branching ratio from Eq. (1.14) of $4.24(43)\,\%$. The large uncertainty primarily originates from the uncertainty in the Q_{EC} value, and excluding it reduces the uncertainty of the total theoretical branching ratio to $0.09\,\%$. A better determination of the mass of ^{31}Ar would thus be very beneficial. The theoretical branching ratio is larger than the experimental value of $3.56(32)\,\%$ (where the $3.8\,\%$ uncertainty originating from the normalisation is included), but the discrepancy is within one standard deviation. The results here constitute an improvement over the earlier result by Fynbo *et al.* [Fyn00], but please note that the uncertainties on both the total experimental and theoretical branching ratios quoted there are underestimated.

As discussed in Section 6.1.1, there is a possible gamma transition from the IAS. Since the energy of this gamma ray is very close to the energy of the second excited state of ^{30}S, we cannot differentiate between protons from

the IAS to the second excited state in ^{30}S and protons going to the ground state in ^{30}S from the level in ^{31}Cl populated by the IAS gamma decay. The $0.108(17)\,\%$ in Table 8.1 for the one-proton decay to the second excited state in ^{30}S thus include both contributions. If we assume that there is a level in ^{31}Cl at $8882(7)\,\mathrm{keV}$ and that this level is only fed in the gamma decay of the IAS, we can use its one- and two-proton decay to include the gamma branching ratio and obtain a total branching ratio of the IAS of $4.30(36)\,\%$. We see that the discrepancy between this experimental branching ratio and the calculated theoretical branching ratio lies within one standard deviation. However, the found experimental branching ratio is an upper limit since the 8882-keV level should also be populated in the Gamow-Teller decay of ^{31}Ar and there might be contributions from other decays to the peaks found in the one- and two-proton spectra. There remain levels in ^{29}P below the proton threshold and one above to which two-proton decays could not be extracted, but their contributions are expected to be small. Due to the large uncertainties, including these will not change the agreement between the theoretical and experimental branching ratios.

8.2 The Gamow-Teller strength

The extraction of the Gamow-Teller strength is much more complicated than the extraction of the Fermi strength, since one has to include all decay modes of the many levels populated in ^{31}Cl. It was attempted by Fynbo *et al.* [Fyn00], but we now have a significantly improved energy and angular resolution and we can now for the first time include the three proton component. The Gamow-Teller strength B_{GT} is given by Eq. (1.15). As for the Fermi strength it is important to determine the branching ratio precisely, and we thus again choose only detector 3 and 6 for the two-proton analysis. For the one-proton analysis we choose only detector 3, since the energy is shifted for high energies for detector 6. Since the number of three-proton events is so limited, all detectors are again used in the three-proton analysis.

The Q_{1p} spectrum is shown in Figure 8.4. A lower energy cut-off of $1\,\mathrm{MeV}$ is used since the spectrum below is dominated by background. There is a contribution from two-proton decays to the multiplicity-one proton spectrum, which we find by scaling the two-proton spectrum by the difference in effi-

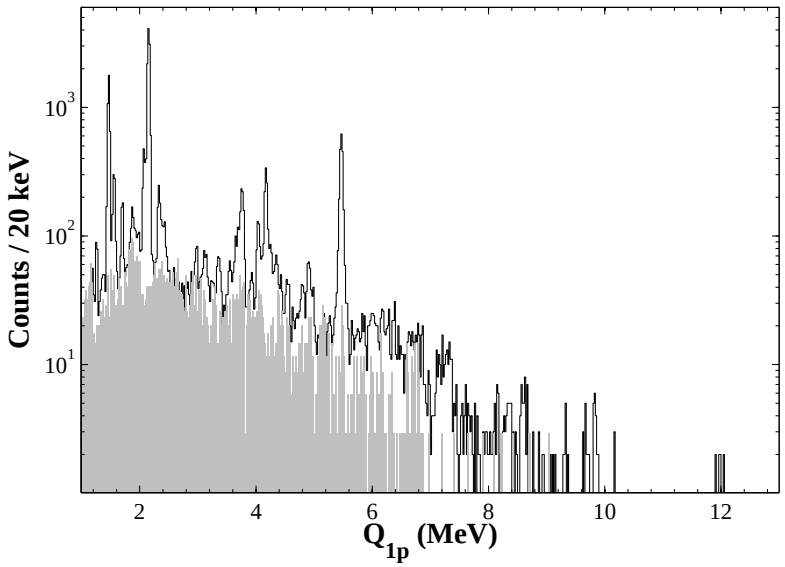

Figure 8.4: The Q_{1p} spectrum calculated for all the particles that has hit detector 3. Also shown is the normalised background from two-proton events estimated from coincidence data in detector 3 and 6 (grey).

ciency. We then subtract it to estimating the B_{GT} distribution from events leading to bound states in ^{30}S. There is also a number of peaks known to originate from decays of the IAS which are also removed. Finally, some transitions are known not to feed the ground state of ^{30}S. The peaks known to go to excited levels in ^{30}S below $5.2\,\mathrm{MeV}$ (listed in Table 2 of Ref. [Fyn00]) are shifted upwards with the excitation energy of $2210.2\,\mathrm{keV}$, $3404.1\,\mathrm{keV}$, $3673\,\mathrm{keV}$ and $5136\,\mathrm{keV}$. Notice that an average energy ($3673\,\mathrm{keV}$) for the third (0^+) and fourth (1^+) level is used, since their energy is so close to each other that it is not possible to deduce which one is populated. The branching ratio is then evaluated bin by bin and the B_{GT} strength deduced.

For the Q_{2p} spectrum shown in Figure 8.5 a lower energy cut-off of $500\,\mathrm{keV}$ is again used for both protons so the spectrum contains the same data as shown in Figure 8.1. For the extraction of the B_{GT} strength the three major peaks from the IAS at $7.6\,\mathrm{MeV}$, $6.3\,\mathrm{MeV}$ and $5.7\,\mathrm{MeV}$ are removed by changing the B_{GT} value in these bins to the average of the values in the bins on each side of the peaks. Some of the remaining two-proton decays will also correspond to transitions to excited states in ^{29}P as discussed in Section 7.2. However, at

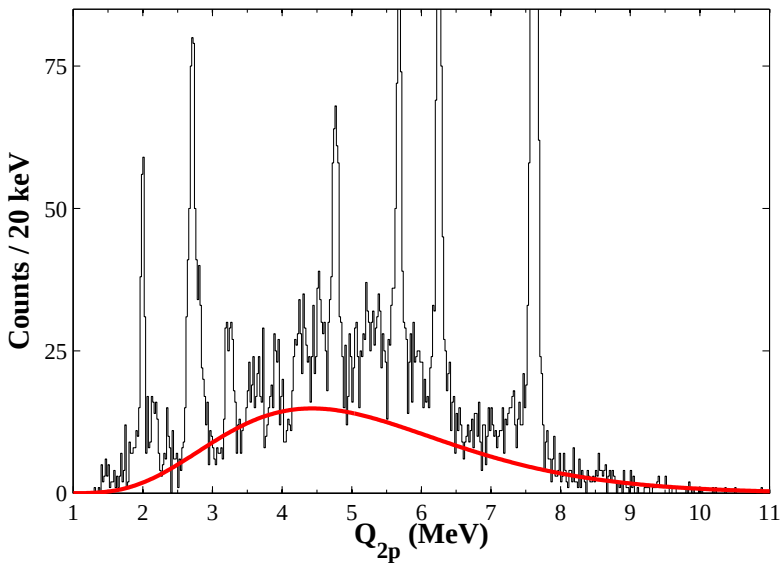

Figure 8.5: Q_{2p} calculated for multiplicity-two events in detector 3 and 6. The vertical range has been cut off for better visualisation of the unresolved structure. The red distribution is the χ^2-distribution from Figure 8.10 folded with itself and manually scaled to the data.

the current level of statistics we cannot identify those transitions so they are all assumed to feed the ground state in ^{29}P. This assumption means that we systematically shift some of the B_{GT} strength to lower energy and somewhat underestimate the total B_{GT} strength.

Finally, the three-proton data used are shown in Figure 8.6. Here the decays from the IAS are the events between $4.3\,\mathrm{MeV}$ and $5.5\,\mathrm{MeV}$. Thus only events above $5.5\,\mathrm{MeV}$ are used for the extraction of the B_{GT} strength. Again all events are assumed to go to the ground state of ^{28}Si.

The total summed B_{GT} spectrum obtained from these spectra can be seen in Figure 8.7 (blue distribution). The individual contributions from the one-proton events (pink distribution) and for the sum of the one- and two-proton events (yellow distribution) are also shown. The total observed Gamow-Teller strength in the one-proton spectrum is $0.60(2)(2)$ compared to $0.58(3)$ found in Ref. [Fyn00]. There are two different contributions to the uncertainties. The first is comprised of (in order of importance) counting statistics, the Q value, the half-life and the setup related uncertainties, while the second is

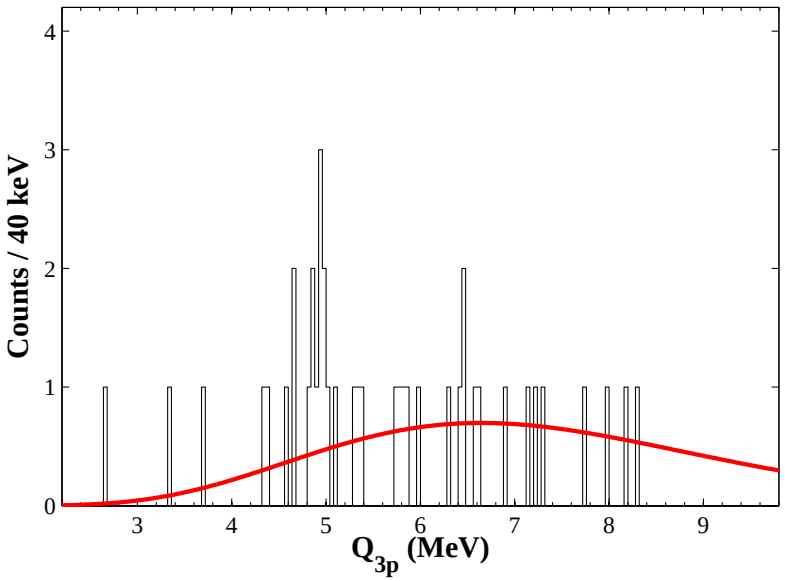

Figure 8.6: Q_{3p} calculated for multiplicity-three events. The red distribution is the χ^2-distribution from Figure 8.10 folded with itself three times and manually scaled to the data.

the $3.8\,\%$ uncertainty on the absolute branching ratio of the main one-proton peak used to extract the number of ^{31}Ar ions in the experiment as described in Section 4.1.4. Fynbo *et al.* use an older result for this normalisation of $11\,\%$, but do not propagate this error correctly. In the two-proton spectrum the total observed Gamow-Teller strength is $2.11(19)(8)$ compared to $1.86(12)$ in Ref. [Fyn00] and in the three-proton spectrum it is $1.03(28)(4)$. There is a systematic bias in the extracted strength such that it underestimates the true strength. This is because we assume all transitions populate the ground state in the one-, two- and three-proton daughters unless population of excited states is explicitly measured from coincident gamma rays.

In Figure 8.7 the total observed Gamow-Teller strength is compared to a shell-model calculation made by Brown [Bro15] in the full sd-shell model space ($0d_{5/2}$, $1s_{1/2}$ and $0d_{3/2}$) using the USDB interaction [Bro06] and a quenching factor of 0.5. The experimental and theoretical distributions follow each other closely, indicating that most of the Gamow-Teller strength has been measured up to about $15.7\,\mathrm{MeV}$. At the highest energies there is more strength

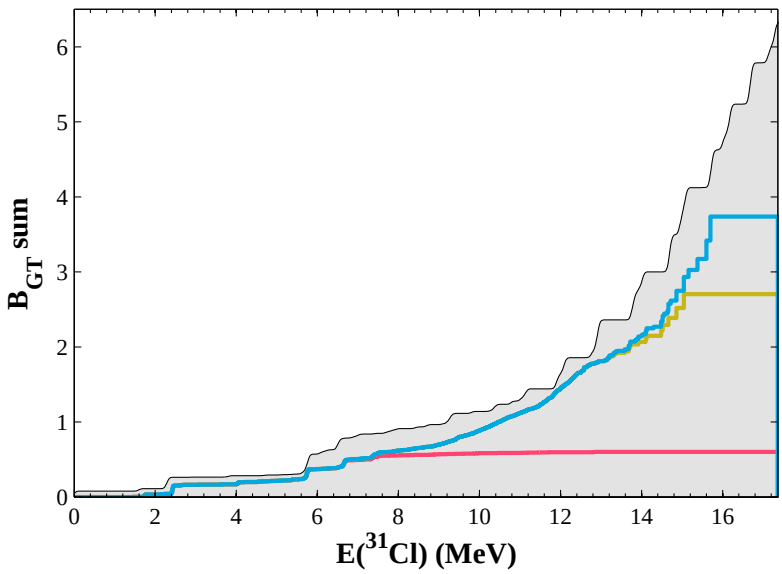

Figure 8.7: The total summed Gamow-Teller strength from one-, two- and three-proton events (blue upper distribution) as a function of excitation energy in ^{31}Cl in the full Q_β energy window ($17.36(21)\,\mathrm{MeV}$). Also shown are the summed B_{GT} spectrum from the one-proton events (pink lower distribution) and for both the one- and two-proton events (yellow middle distribution). The shaded area shows the summed Gamow-Teller strength from a shell-model calculation in the full sd-shell by Brown [Bro15].

predicted than experimentally identified. However, the missing strength corresponds to only 1–3 missing events in that energy region, which means that the deviation is not statistically significant.

The one-proton decay mode contributes up to $12.85\,\mathrm{MeV}$ and the two-proton decay mode starts contributing at $5.90\,\mathrm{MeV}$, and is the dominant contribution from around $7.5\,\mathrm{MeV}$. The two-proton decay mode contributes until $15.04\,\mathrm{MeV}$ and the three-proton decay mode is observed for the Gamow-Teller beta decay at $13.16\,\mathrm{MeV}$ and dominates above $15.04\,\mathrm{MeV}$. According to this there is an evolution in the dominating decay modes, i.e. more protons are emitted with increasing excitation energy, which is known to be the case for neutron emission from nuclei close to stability [Gho50, Mor53]. This behaviour is investigated in more detail in the following sections.

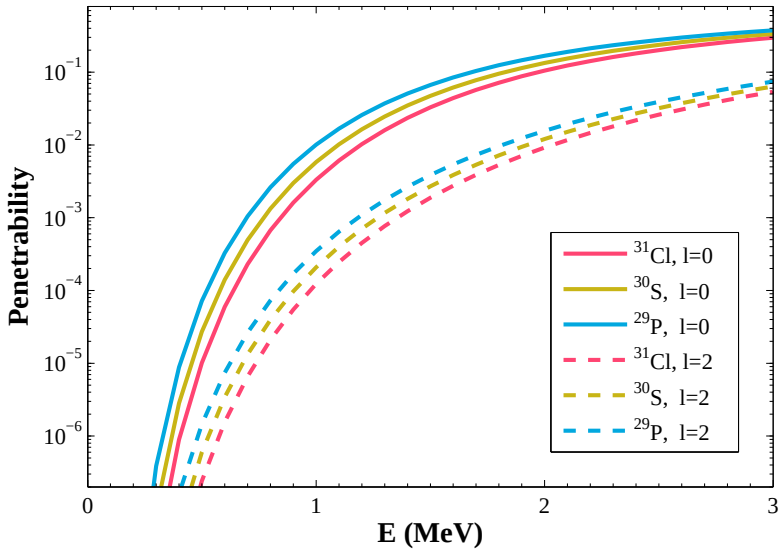

Figure 8.8: The penetrability as a function of energy for $l = 0, 2$ for ^{31}Cl, ^{30}S and ^{29}P calculated using Ref. [Tho09].

8.3 A simple model for proton emission

The energy distribution of the emitted proton from a given level depends on three factors: The phase space, the level density in the daughter nucleus and the penetrability [Hor72]. The phase space grows proportionally to the proton energy and the level density in the daughter nucleus increases with excitation energy. At low proton energy the spectrum is dominated by the penetrability, since it decreases strongly with decreasing energy. We expect proton decay branches to be suppressed if the penetrability is less than 10^{-4} because the widths of the ^{31}Cl levels are of the order $10\,\mathrm{keV}$ when disregarding the penetrability and that gamma decays enter when the widths of the levels are of the order $1\,\mathrm{eV}$. We expect the emitted protons to be predominantly from the sd-shell and hence $l = 0, 2$ to be favoured in the proton emissions due to the structure of ^{31}Ar. The penetrability can be found using Ref. [Tho09] and is shown in Figure 8.8. In our case a penetrability of 10^{-4} corresponds to proton energies of around $0.6\,\mathrm{MeV}$ for s-wave transitions and around $0.9\,\mathrm{MeV}$ for d-wave transitions for the isotopes involved in the decay so we expect decay branches with proton energies below this energy to be suppressed. This

agrees well with what we observe for the levels of ^{30}S, where we observe proton decays down to the 5.2-MeV level approximately $0.8\,\mathrm{MeV}$ above the proton threshold. For high energies the level density will be so high that the decay can be treated purely statistically [Bor13]. In his paper Ref. [Dét91], Détraz calculated and plotted the intensity of protons as a function of energy for the decay of the IAS taking into account all three factors. The result is a bell-shaped distribution with a long high-energy tail. Extending this to our case, where multiple levels in ^{31}Cl are populated, the energy distribution should be a sum of similar distributions shifted in energy. Since the energy shifts are small, the resulting sum should be similar in shape. This will also be the case for decays of excited levels in both ^{29}P and ^{30}S, and thus also when one considers the two- and three-proton energy spectra. However, for levels close to the threshold this picture breaks down, and the decay will instead result in a number of resolved lines in the spectrum. We now check our current sensitivity to modelling by using a simple model that relies on a few assumptions, namely that the three stages of proton emission are independent and that they all can be described by the same distribution.

We first consider the energy spectrum for two-proton events in Figure 8.9. The reason for starting with the two-proton spectrum is that the levels fed in ^{30}S have a sufficiently large excitation energy so that the level density is high. This means that this spectrum contains fewer resolved lines than the one-proton spectrum. The major resolved lines around $0.7\,\mathrm{MeV}$ are most likely due to an overlap in the structure of ^{31}Ar and the $5.2\,\mathrm{MeV}$ level fed in ^{30}S (cf. Section 6.4). Disregarding the resolved lines in the spectrum, the energy distribution does seem to have the same shape as calculated by Détraz [Dét91], i.e. a bell-shape with a long high-energy tail. A well known function with this shape is the χ^2-distribution. By manually adjusting the parameters of this function to the data we find the parametrisation

$$h_{2p} = 560 \cdot \chi^2(x,k) = 560 \cdot \frac{1}{2^{\frac{k}{2}}\Gamma\left(\frac{k}{2}\right)} x^{\frac{k}{2}-1} e^{-\frac{x}{2}}, \tag{8.1}$$

with $$x = 2.8 \cdot \tfrac{E_p}{\mathrm{MeV}} - 2.0 \quad \text{and} \quad k = 6,$$

which is shown together with the data in Figure 8.9. The distribution has an average energy of $2.86\,\mathrm{MeV}$.

Correcting the energy of the proton for recoil (see Eq. (1.27)) we get the

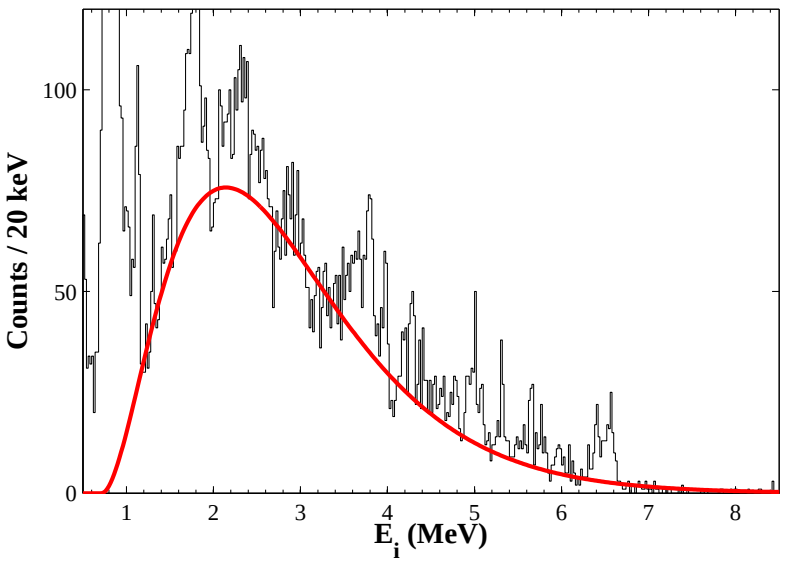

Figure 8.9: Energies of the individual protons detected in multiplicity-two events. The vertical range has been cut off for better visualisation of the unresolved structure. The red distribution is a χ^2-distribution adjusted manually to the data: $h_{2p} = 560 \cdot \chi^2(2.8 \cdot \frac{E}{\mathrm{MeV}} - 2.0, 6)$.

typical value of Q_{1p}. This is scaled and plotted in Figure 8.10 together with the Q_{1p} value for all particles which hit detector 3. Again disregarding the resolved lines, the shape of the data seems to match the distribution.

By folding the distribution with itself the typical value of Q_{2p} is obtained corresponding to randomly adding the energies of the two protons. Here we benefit from having chosen the χ^2-distribution since, when folding the χ^2-distribution with another χ^2-distribution, the result is just a χ^2-distribution with a k-parameter equal to the sum of the k-parameters from the original distributions [Jam06]. The Q_{2p} spectrum can be seen in Figure 8.5 together with this distribution, which is again scaled to fit the data. The simple model still describes the data fairly well when disregarding the resolved lines.

Finally, folding the distribution with itself once more gives the typical values of Q_{3p}. This is shown in Figure 8.6 together with the data. Here the statistics are very limited, but the data are consistent with the trend displayed by the simple model.

It should be stressed that the fitted distributions are only simplified mod-

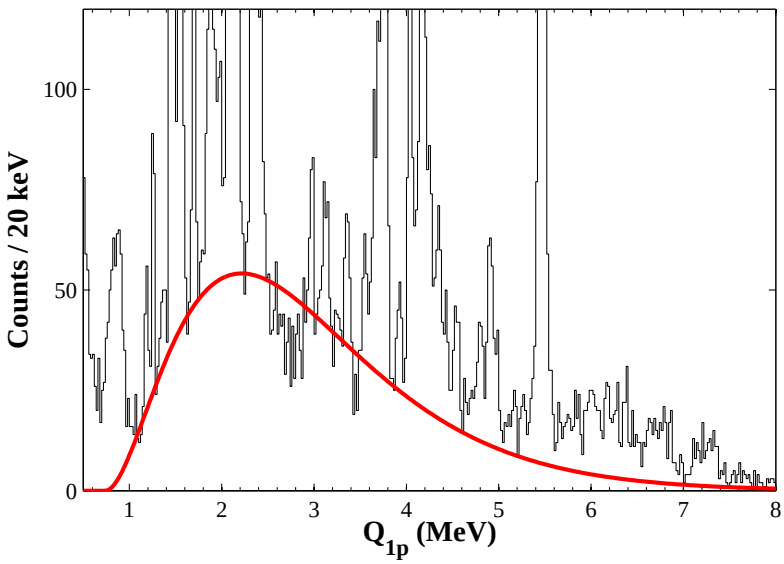

Figure 8.10: Q_{1p} calculated for all particles detected in detector 3. The vertical range has been cut off for better visualisation of the unresolved structure. The red distribution is the χ^2-distribution from Figure 8.9 transformed using the recoil factor and manually scaled to the data.

els and that they are not fitted to the data, but only adjusted and scaled manually. However, it is remarkable that with this very simple approach it is possible to relate Q_{ip} distributions (for $i = 1, 2, 3$) to each other. In the next section we will extend our model to give predictions for one-, two- and three-proton branching ratios.

8.4 The evolution of decay modes

In Section 8.2 we saw that there was an evolution in the dominating decay modes, where more protons are emitted with increasing excitation energy. We now want to expand our model from Section 8.3 to see if it is possible to predict this evolution and thereby the branching ratios for the three decay mechanisms.

We start by considering ^{31}Ar and assume that the energies of the protons in the decays are given by the relation in Eq. (8.1). For a given level in ^{31}Cl the distribution of Q_{1p}, Q_{2p} and Q_{3p} from this level can be represented by a known

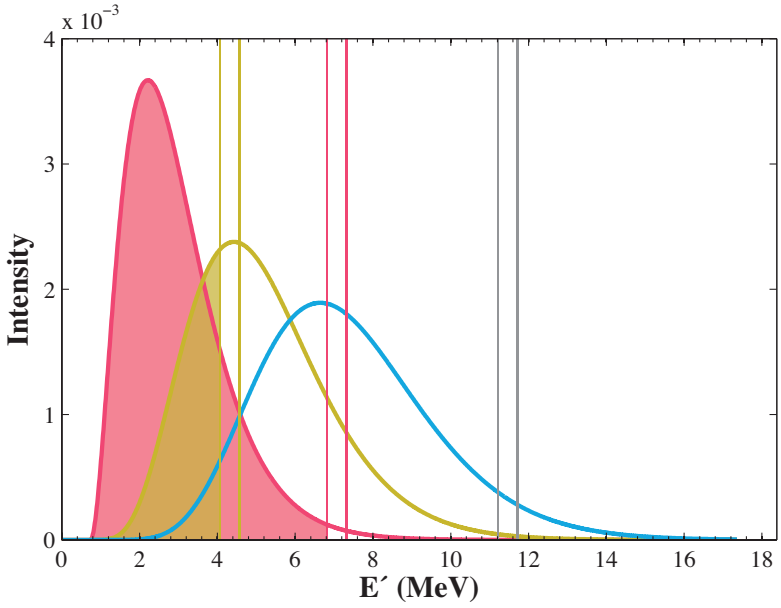

Figure 8.11: The Q_{1p} distribution (red), Q_{2p} distribution (yellow) and Q_{3p} distribution (blue) drawn as a function of E', which is the energy from the chosen level in ^{31}Cl (i.e. $E' = 0$ corresponds to the energy of the level in ^{31}Cl and $E' = 1\,\mathrm{MeV}$ is $1\,\mathrm{MeV}$ below this level). Here we have chosen the energy of the ^{31}Cl level to be $12\,\mathrm{MeV}$. The yellow, red and grey thick vertical lines correspond to the three-, two- and one-proton thresholds, respectively. The corresponding thinner lines below illustrate the chosen threshold t of $500\,\mathrm{keV}$. The red shaded area corresponds to the fraction of the one proton emissions that will lead to further proton emission (b'_{1f}) and the yellow shaded area likewise corresponds to the fraction of the two proton emissions that will lead to further proton emission (b'_{2f}).

function as described in Section 8.3. Now assume that, after emitting the first proton, we populate a level in ^{30}S with energy above a certain limit t above the proton threshold, then the nucleus will again decay by a proton. From the penetrabilities we know that this threshold should be somewhere below 0.6–$0.9\,\mathrm{MeV}$. In ^{30}S we see proton decays from the level $0.8\,\mathrm{MeV}$ above the proton threshold and in ^{29}P we see proton decays from the level $0.7\,\mathrm{MeV}$ above the proton threshold. We thus choose the threshold t to be $500\,\mathrm{keV}$ corresponding to penetrabilities of the order 10^{-5} for s-wave transitions and 10^{-6} for d-wave transitions. For a given level in ^{31}Cl the fraction of one proton emissions that will lead to further proton emissions is just the fraction of the χ^2 distribution for Q_{1p} which lies below $E\big(^{31}\mathrm{Cl}\big) - S_{2p} - t$. An illustration can be seen in Figure 8.11, where this corresponds to the red shaded area. By integrating over all energies in ^{31}Cl we can find the fraction of one proton emissions that will lead to further proton emissions as

$$b'_{1f} = \frac{\int_0^{E\left(^{31}\mathrm{Cl}\right)-S_{2p}-t} \chi^2\left(a\cdot r\cdot \frac{E'}{\mathrm{MeV}}+b,k\right)\,dE'}{\int_0^{\infty}\chi^2\left(a\cdot r\cdot \frac{E'}{\mathrm{MeV}}+b,k\right)\,dE'}, \tag{8.2}$$

where $a = 2.8$, $b = 2.0$ and $k = 6$. $E\big(^{31}\mathrm{Cl}\big)$ is the level chosen in ^{31}Cl, S_{2p} the two-proton separation energy and $r = \frac{M\left(^{30}\mathrm{S}\right)}{M\left(^{30}\mathrm{S}\right)+m_p}$ is the recoil factor (see Eq. (1.27)). Since the χ^2-distribution is normalised, the denominater is 1. The integral in the numerator can be solved analytically and we obtain the solution

$$b'_{1f} = \Gamma_{\mathrm{inc}}\left(\tfrac{1}{2}\cdot\left(a\cdot r\cdot\frac{E\left(^{31}\mathrm{Cl}\right)-S_{2p}-t}{\mathrm{MeV}}+b\right),\frac{k}{2}\right), \tag{8.3}$$

where the incomplete gamma function is defined as $\Gamma_{\mathrm{inc}}(x,k)\equiv\int_0^x e^{-t}t^{k-1}\,dt$. We obtain the fraction of the two proton emissions that will lead to further proton emission in a similar manner:

$$\begin{aligned} b'_{2f} &= \frac{\int_0^{E\left(^{31}\mathrm{Cl}\right)-S_{3p}-t} \chi^2\left(a\cdot r\cdot \frac{E'}{\mathrm{MeV}}+b,2k\right)\,dE'}{\int_0^{\infty}\chi^2\left(a\cdot r\cdot \frac{E'}{\mathrm{MeV}}+b,k\right)\,dE} \\ &= \Gamma_{\mathrm{inc}}\left(\tfrac{1}{2}\cdot\left(a\cdot r\cdot\frac{E\left(^{31}\mathrm{Cl}\right)-S_{3p}-t}{\mathrm{MeV}}+b\right),\frac{2k}{2}\right), \end{aligned} \tag{8.4}$$

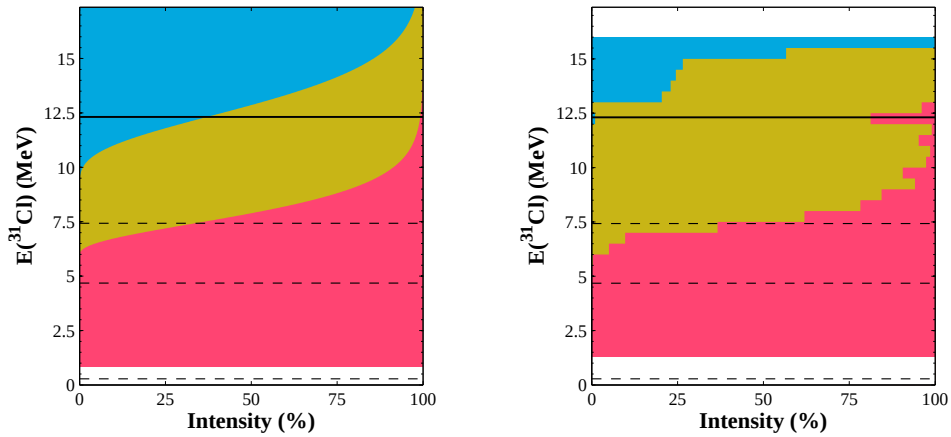

Figure 8.12: The intensities of one- (red), two- (yellow) and three-proton (blue) decays as a function of excitation energy in ^{31}Cl. The horizontal dashed lines corresponds to the one-, two- and three-proton separation energy, respectively. The horizontal full line corresponds to the energy of the IAS. (a) is calculated using Eqs. (8.2)-(8.5). A lower threshold of $500\,\mathrm{keV}$ above the one-proton separation energy is chosen for the one-proton decays and similar for the two- and three-proton decays. (b) is calculated from the data using $500\,\mathrm{keV}$ energy bins.

where S_{2p} is the three-proton separation energy and we again choose $t = 500\,\mathrm{keV}$. The one-, two and three-proton branching ratios for the level in ^{31}Cl are then

$$b'_{1p} = 1 - b'_{1f}, \quad b'_{3p} = b'_{1f} \cdot b'_{2f}, \quad b'_{2p} = b'_{1f} - b'_{2p}. \tag{8.5}$$

Figure 8.12a shows these branching ratios as a function of the energy in ^{31}Cl. We can compare these with the measured ratios shown in Figure 8.12b. It is clear that the one-proton decay dominates for the low-lying levels in ^{31}Cl. When the excitation energy increases, the two-proton decay takes over and finally the three-proton decays dominate for very high excitation energies. This is the same trend which is observed in neutron emission from nuclei close to stability as we mentioned previously. From Figure 8.12 we see that our prediction is very good for the crossing from one-proton dominance to two-proton dominance, while the three-proton decay is introduced too early

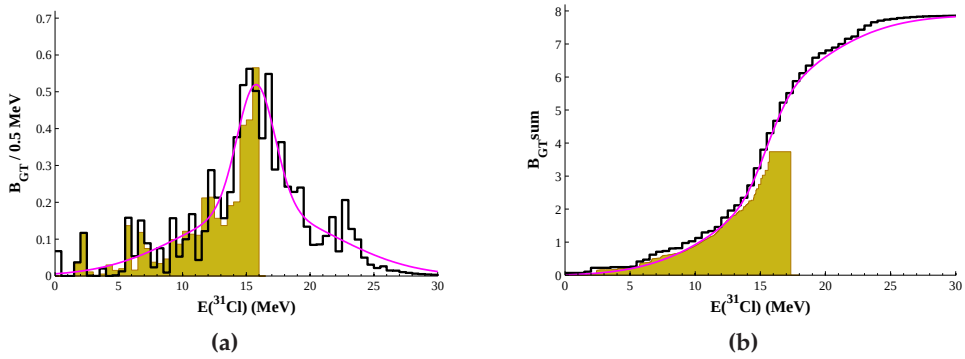

Figure 8.13: (a) The theoretical B_{GT} distribution calculated by Brown [Bro15] (black) shown together with the B_{GT} calculated from the data (yellow). The purple distribution is a fit to the theoretical distribution by two Gaussian distributions. (b) The summed B_{GT} distributions of (a).

with our model.

To make a prediction for the beta-delayed one-, two- and three-proton branching ratios we now just need to fold the distribution in Figure 8.12a with the branching ratio for feeding the different levels in ^{31}Cl. This we can of course get directly from the data, but since we want the model to have as little data input as possible, we instead use a theoretically computed B_{GT} distribution. In Figure 8.13a a calculation of the B_{GT} by Brown [Bro15] (the same as used in Figure 8.7) is shown together with the B_{GT} extracted from the data. Also shown in Figure 8.13a is a fit to the distribution by two Gaussian distributions, which means $\mu_1 = 15.76(16)\,\mathrm{MeV}$ and $\mu_2 = 15.9(6)\,\mathrm{MeV}$, standard deviations $\sigma_1 = 1.48(21)\,\mathrm{MeV}$ and $\sigma_2 = 6.1(9)\,\mathrm{MeV}$ and amplitudes $N_1 = 1.28(26)\,\mathrm{MeV}$ and $N_2 = 2.67(31)\,\mathrm{MeV}$. In Figure 8.13b we see that the summed distribution to a good approximation follows the summed B_{GT} distribution.

We now find the branching ratio for feeding the different levels in ^{31}Cl using Eq. (1.15). We normalise it to the expected total Gamow-Teller beta-delayed proton branching ratio. From our data we find it to be $73.9(36)\,\%$. However, because this value includes the gamma-delayed proton decays of the IAS (assuming our hypothesis from Section 6.1.1 is correct), the real value should be smaller. Instead we use the $74.4(3)\,\%$ found by Lis *et al.* [Lis15]

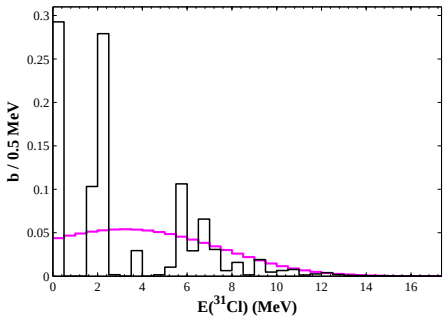

Figure 8.14: The beta branching ratio calculated using Eq. (1.15) from the B_{GT} distributions shown in Figure 8.13a. The black distribution is from the B_{GT} calculated by Brown and the purple distribution is from the Gaussian distributions fitted to this B_{GT} distribution.

for the total beta-delayed proton branching ratio and subtract the theoretical Fermi contribution of $4.24(43)\,\%$ (cf. Section 8.1). This gives us a total Gamow-Teller beta-delayed proton branching ratio of $73.2(5)\,\%$. Because we have a lower energy cut on the one-proton spectrum of $1\,\mathrm{MeV}$ we exclude the contributions for energies below the one-proton separation energy plus $1\,\mathrm{MeV}$ when we do the normalisation. The branching ratios found as a function of excitation energy in ^{31}Cl are shown in Figure 8.14. We see that the fitted distribution underestimates the branching ratio for small energies, where the one-proton decay is dominant. We thus expect the fitted distribution to underestimate the one-proton branching ratio compared to the one deduced from the theoretically calculated B_{GT} distribution. We can now fold this with the probability for one-, two and three-proton emission to obtain the total branching ratios for the beta-delayed Gamow-Teller decays. Again we exclude the contributions for energies below the one-proton separation energy plus $1\,\mathrm{MeV}$.

The result can be found in Table 8.2, where the branching ratios obtained from the data are shown for comparison. For most nuclei where a three-proton decay is kinematically allowed, the proton branching ratios measured experimentally will include both the Gamow-Teller and Fermi contribution. To be able to compare our model with the experimental results, we thus have to include the Fermi contribution as well. We do this by assuming that the proton branching ratio of the decay of the IAS is split in the same way as a level with the same energy fed by a Gamow-Teller decay. This assumption

Table 8.2: The total branching ratios for the beta-delayed one-, two- and three-proton decays of ^{31}Ar, ^{43}Cr and ^{39}Ti as predicted by the model using either the B_{GT} calculated by Brown or the double Gaussian fit to this distribution. Both the prediction for the full beta strength (GT+IAS) and for only the Gamow-Teller part is shown. For ^{31}Ar the experimental results (Exp.) obtained in this chapter are shown for comparison. An independent measurement have been made by Lis *et al.* [Lis15] using an optical time projection chamber, which is also shown for the full beta strength (Exp. O.). Experimental values have also been found for ^{43}Cr using an optical time projection chamber [Pom11] and they are shown for comparison (Exp. O.).

			$b_{\beta 1p}$ (%)	$b_{\beta 2p}$ (%)	$b_{\beta 3p}$ (%)
^{31}Ar	GT	Brown	66	7	0.6
		Fit	60	12	0.9
		Exp.	65.8(32)	8.0(9)	0.055(19)
	GT + IAS	Brown	66	10	2
		Fit	60	15	2
		Exp.	66.5(33)	10.8(10)	0.095(28)
		Exp. O.	68.3(3)	9.0(2)	0.07(2)
^{43}Cr	GT	Brown	67	4	0.10
		Fit	67	4	0.10
	GT + IAS	Brown	75	13	0.10
		Fit	75	13	0.10
		Exp. O.	81(4)	7.1(4)	0.08(3)
^{39}Ti	GT	Brown	69	3	0.03
		Fit	68	4	0.05
	GT + IAS	Brown	74	20	0.04
		Fit	73	21	0.06

should in principle be correct, since the IAS due to isospin mixing will proton decay via a nearby level, cf. Section 1.1.1. However, the IAS can also decay by gamma emission, which means that the subsequent proton decay will originate from a lower lying level, whose decay modes are divided in another way with a stronger weight to the decay modes with low multiplicity. In this way we incorrectly assign more strength to the decay branches with higher multiplicity. How much depends on the energy of the IAS and the gamma daughter(s) of the IAS. The total one-, two- and three-proton branching ratios for the decay of ^{31}Ar are also shown in Table 8.2. These can be compared with an independent measurement made by Lis *et al.* [Lis15] using an optical time projection chamber (OTPC). Their result is also shown in Table 8.2 and we see that it agrees very well with our measurement.

We also see that there is a fairly good agreement between our model and the experimental results for the one- and two-proton branching ratios. Using the fit for the B_{GT} underestimates the one-proton branching ratio and overestimates the two-proton branching ratio as expected, since the fit underestimates the beta branching ratio to the lowest levels in ^{31}Cl as seen in Figure 8.14. The model overestimates the three-proton branching ratio by an order of magnitude compared to the data. One possible explanation is that only some of the full three-proton strength has been measured. However, this is not likely since it has been measured by two independent experiments (ours and Ref. [Lis15]) using different techniques. Instead, it is most likely caused by the crude assumptions of the model. The assumption that the emitted protons can have an arbitrary energy does not hold when the level density is low. This is the case for the levels populated in ^{29}P in the three-proton decay, which will lie relatively close to the proton threshold. Here a full model will need to take the structure of the nuclei in the individual transitions into account. The estimate given by the model here will be an upper limit of the three-proton branching ratio unless there are special structure effects, which will favour the three-proton decay. Note, however, that overestimating the three-proton branching ratio does not influence the estimate of the one- and two-proton branching ratios significantly.

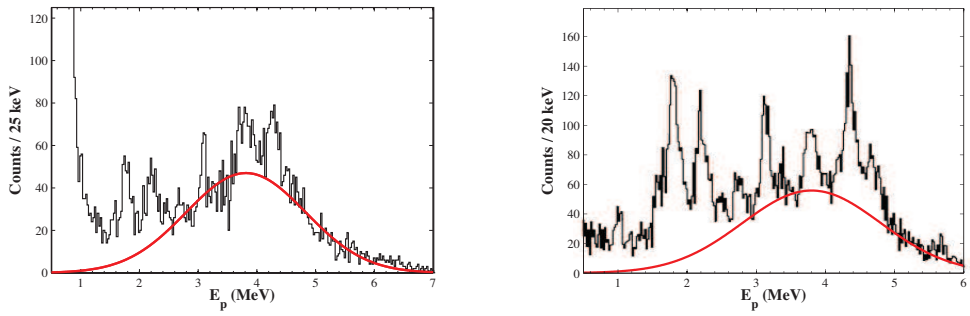

(a) (b)

Figure 8.15: The proton energies from the decay of ^{43}Cr (a) measured by Giovinazzo *et al.* [Gio01] (b) measured by Dossat *et al.* [Dos07]. The red distribution is a Gaussian distribution adjusted manually to fit both dataset.

8.5 Predictions of branching ratios

We can now use the model to make predictions about the branching ratios for other nuclei. Since the model depends on the distribution of the energies of the emitted protons, it can only be used for nuclei with sufficient proton data. In the following subsections the model is used on two other nuclei, ^{43}Cr and ^{39}Ti. The assumptions used are explained in detail for the case of ^{43}Cr.

8.5.1 ^{43}Cr

The proton spectrum for the decay of ^{43}Cr has been measured by Giovinazzo *et al.* [Gio01] and by Dossat *et al.* [Dos07] and can be seen in Figure 8.15. The spectra also include summed proton energies of beta-delayed two-proton events. In principle these events should be removed, but unfortunately this is not possible. The peak at $4.3\,\mathrm{MeV}$ is believed to originate from the beta-delayed two-proton decay of the IAS and we will thus try to discard it when fitting.

The energy distribution when disregarding the resolved lines seems to be more symmetric than was the case for ^{31}Ar. A χ^2-distribution is therefore not a good approximation. Instead we use a Gaussian distribution which is symmetric. By manually adjusting it to fit the data, we obtain a distribution

with mean $\mu = 3.8\,\mathrm{MeV}$ and standard deviation $\sigma = 1.0\,\mathrm{MeV}$. The branching ratios for the one-, two- and three proton decay from a level in the ^{43}Cr beta daughter can be found as for ^{31}Ar using Eq. (8.2)-(8.5). But since we now use the Gaussian distribution we have to substitute this for the χ^2-distribution and we get

$$b'_{1f} = \frac{\int_0^{E(^{43}\mathrm{V})-S_{2p}-t} G\Big(r \cdot \frac{E'}{,}\mu, \sigma\Big)\, dE'}{\int_0^{\infty} G\Big(r \cdot \frac{E'}{,}\mu, \sigma\Big)\, dE'} = \frac{\sigma}{2r}\left[\mathrm{erf}\Big(\frac{\mu}{2\sigma^2}\Big) + \mathrm{erf}\left(\frac{r \cdot \big(E(^{43}\mathrm{V}) - S_{2p} - t\big) - \mu}{2\sigma^2}\right)\right], \tag{8.6}$$

where the error function is defined as $\mathrm{erf}(x) \equiv \int_0^x e^{-t^2}\, dt$. Since folding a Gaussian distribution with another Gaussian distribution just gives a Gaussian distribution with the mean equal the sum of the two means and variance equal the sum of the variances, we find that b'_{2f} is given as b'_{1f} with μ substituted by 2μ and σ substituted by $\sqrt{2}\sigma$. The separation energies used can be found in Table 8.3, which contains all the quantities that are different from the case of ^{31}Ar. The resulting branching ratios as a function of energy are shown in Figure 8.16.

The next step is to find a B_{GT} distribution. We choose the same distribution as used for ^{31}Ar, but shifted in energy. In principle we should also scale by the difference in Gamow-Teller strength, but since it is proportional to the Fermi strength B_F (see Section 1.1.3) and this is the same for ^{43}Cr and ^{31}Ar (see Table 8.3), this is not necessary here. To find out how much we need to shift the distribution from ^{31}Ar, we look at the difference between the energy of the IAS and the Gamow-Teller centroid energy ($E_{\mathrm{GT}} - E_{\mathrm{IAS}}$). For ^{31}Cl (the beta daughter of ^{31}Ar) we estimate this as the difference between the energy of the IAS found in Section 8.1 and the mean of the first Gaussian distribution in the Gaussian fit to the B_{GT} distribution (note that the discrepancy between the means of the two Gaussian distributions is within one standard deviation). We find that $E_{\mathrm{GT}} - E_{\mathrm{IAS}}$ for ^{31}Cl is $3.45(16)\,\mathrm{MeV}$ and we now need to the this difference for the beta daughter of ^{43}Cr. In Ref. [Lan00] the shell-model Gamow-Teller centroid energy relative to the energy of the IAS ($E_{\mathrm{GT}} - E_{\mathrm{IAS}}$) is calculated for neutron-rich nuclei as a function of $(N-Z)/A$. Their results are shown in Figure 8.17 and we see that we can approximate the

Table 8.3: A table of the different parameters used as inputs in our model. The one-proton separation energies for the beta-delayed one- (S_{p1}), two- (S_{p2}) and three-proton S_{p3} daughters are all found using the nuclear masses from Ref. [Wan12], except S_{p1} for ^{31}Ar, which is from Ref. [Saa11]. Q_{EC} for ^{39}Ti and ^{43}Cr is also found from Ref. [Wan12]. The half-life, $T_{1/2}$ for ^{39}Ti are from Ref. [Dos07] and for ^{43}Cr it is the weighted average of [Gio01, Dos07, Pom11]. The energy of the IAS, E_{IAS}, for ^{43}Cr and ^{39}Ti are found from the mass-excess of the IAS measured in Ref. [Dos07] and the mass-excess of the ground state from Ref. [Wan12]. The total branching ratio for beta-delayed proton emission, $b_{\beta p}$, is taken from Ref. [Dos07] for ^{39}Ti and from Ref. [Pom11] for ^{43}Cr. They are used to calculate the total branching ratio for Gamow-Teller beta decays $b_{\beta p,\mathrm{GT}}$. $(E_{\mathrm{GT}} - E_{\mathrm{IAS}})_m$ is the difference between the Gamow-Teller centroid energy and the energy of the IAS for the mirror nuclei to the beta daughters and $(E_{\mathrm{GT}} - E_{\mathrm{IAS}})$ is the difference used for the beta daughters to obtain the downwards shift of the B_{GT} distribution, ΔE, as a multiple of $0.5\,\mathrm{MeV}$.

	^{31}Ar	^{43}Cr	^{39}Ti
S_{p1}	$0.2828(44)\,\mathrm{MeV}$	$0.097(47)\,\mathrm{MeV}$	$-0.597(24)\,\mathrm{MeV}$
S_{p2}	$4.3956(7)\,\mathrm{MeV}$	$3.7512(3)\,\mathrm{MeV}$	$4.547\,28(22)\,\mathrm{ms}$
S_{p3}	$2.7486(6)\,\mathrm{MeV}$	$1.084\,99(9)\,\mathrm{MeV}$	$1.857\,63(10)\,\mathrm{ms}$
E_{IAS}	$12.313(4)\,\mathrm{MeV}$	$8.22(4)\,\mathrm{MeV}$	$9.12(4)\,\mathrm{MeV}$
Q_{EC}	$18.38(10)\,\mathrm{MeV}$	$15.62(40)\,\mathrm{MeV}$	$16.37(21)\,\mathrm{MeV}$
$T_{1/2}$	$15.1(3)\,\mathrm{ms}$	$21.1(3)\,\mathrm{ms}$	$28.5(9)\,\mathrm{ms}$
$B_F = Z - N$	5	5	5
$b_{\beta p}$	$77.4(3)\,\%$	$88(4)\,\%$	$93.7(2.8)\,\%$
$b_{\beta p,\mathrm{GT}}$	$73.2(5)\,\%$	$70(4)\,\%$	$72.3(34)\,\%$
$(E_{\mathrm{GT}} - E_{\mathrm{IAS}})_m$	$4.58\,\mathrm{MeV}$	$6.17\,\mathrm{MeV}$	$5.74\,\mathrm{MeV}$
$E_{\mathrm{GT}} - E_{\mathrm{IAS}}$	$3.45(16)\,\mathrm{MeV}$	$5.04\,\mathrm{MeV}$	$4.64\,\mathrm{MeV}$
ΔE	$0\,\mathrm{MeV}$	$2.5\,\mathrm{MeV}$	$2.0\,\mathrm{MeV}$

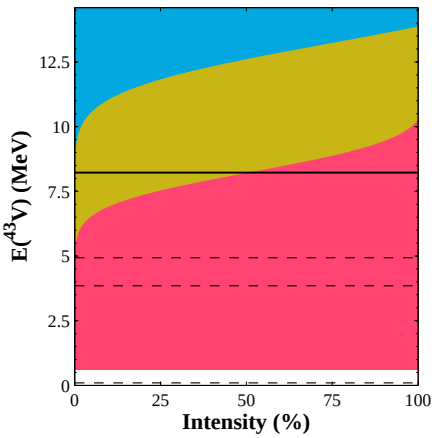

Figure 8.16: The calculated intensities of one- (red), two- (yellow) and three-proton (blue) decays as a function of excitation energy in the beta daughter of ^{43}Cr. The horizontal dashed lines corresponds to the one-, two- and three-proton separation energy, respectively. The horizontal full line corresponds to the energy of the IAS. A lower threshold of $500\,\mathrm{keV}$ above the one-proton separation energy is chosen for the one-proton decays and similar for the two- and three-proton decays.

dependence by a straight line. Using this line we obtain the $(E_{\mathrm{GT}} - E_{\mathrm{IAS}})$ for the mirror nuclei of the beta daughters of ^{31}Ar and ^{43}Cr, see Table 8.3. We see that the $(E_{\mathrm{GT}} - E_{\mathrm{IAS}})$ for the mirror nuclei to ^{31}Cl lies approximately $1\,\mathrm{MeV}$ above the $3.45(16)\,\mathrm{MeV}$ energy difference found above. We thus assume that the $(E_{\mathrm{GT}} - E_{\mathrm{IAS}})$ for the beta daughter of ^{43}Cr is also shifted downwards by approximately $1\,\mathrm{MeV}$. Returning to the B_{GT} distribution, we find that this has to be shifted downwards by the energy:

$$\Delta E = (E_{\mathrm{GT}} - E_{\mathrm{IAS}})_{\,^{31}\mathrm{Ar}} - (E_{\mathrm{GT}} - E_{\mathrm{IAS}}) + E_{IAS,\,^{31}\mathrm{Ar}} - E_{\mathrm{IAS}}. \qquad (8.7)$$

Since our B_{GT} distribution is calculated for $0.5\,\mathrm{MeV}$ bins, we adjust the $(E_{\mathrm{GT}} - E_{\mathrm{IAS}})$, so that we shift the B_{GT} distribution by an integer number of bins. The resulting $(E_{\mathrm{GT}} - E_{\mathrm{IAS}})$ and ΔE can be found in Table 8.3. The B_{GT} distributions used for ^{43}Cr is shown in Figure 8.18a. From this the branching ratios can be found as a function of excitation energy in the beta daughter using Eq. (1.15), where we use the half-life, the energy of the IAS and the Q_{EC} given in Table 8.3. We assume that only levels $500\,\mathrm{keV}$ above the one-proton sep-

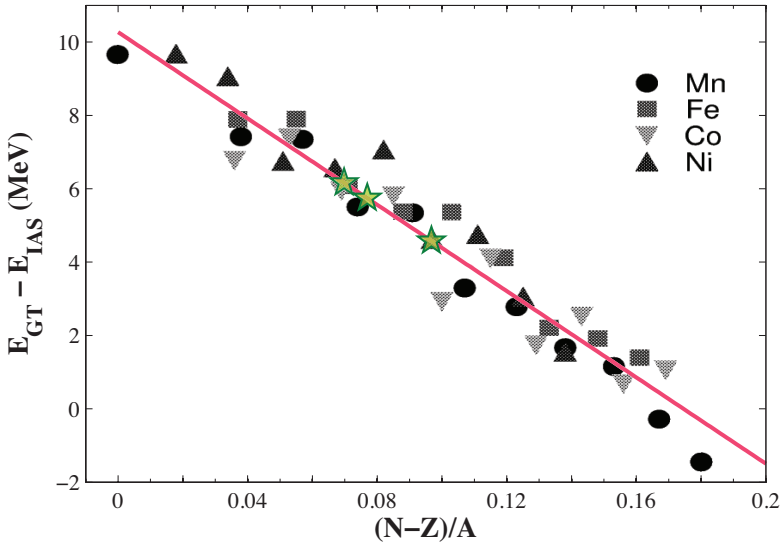

Figure 8.17: The Gamow-Teller centroid energy relative to the energy of the IAS for neutron-rich nuclei as a function of $(N-Z)/A$. The data points are from Ref. [Lan00]. The red line is a fit to these points and the stars mark the values on this line for the daughters of ^{31}Ar, ^{43}Cr and ^{39}Ti.

aration energy will decay by proton emission and we then normalise the distribution to the total proton branching ratio for Gamow-Teller decays. This is found from the total proton branching ratio $b_{\beta p}$ by subtracting b_F found using Eq. (1.14). The branching ratios as a function of excitation energy in the beta daughter that we obtain are shown in Figure 8.18b.

We now fold this by the distribution in Figure 8.16 and obtain the total branching ratios for the beta-delayed one-, two- and three-proton decay given in Table 8.2. As for ^{31}Ar we include a contribution from the IAS by assuming that the IAS decays in the same way as a level fed by a Gamow-Teller transition with the same energy. This is also shown in Table 8.2 together with an experimental result from Ref. [Pom11]. Considering the crude assumptions they agree surprisingly well. Especially the three-proton branching ratios which agree within only one standard deviation. The one-proton branching ratio is slightly underestimated while the two-proton branching ratio is overestimated. This could be due to a number of things. (i) Naturally, it could be that the model is wrong or does not hold for the case of ^{43}Cr due to a special

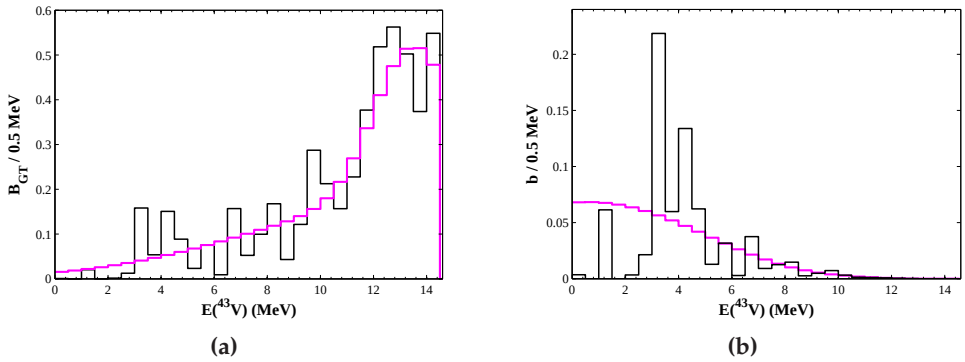

Figure 8.18: (a) The theoretical B_{GT} distributions from Figure 8.13a shifted downwards by $2.5\,\mathrm{MeV}$ used for the decay of ^{43}Cr. (b) The distribution of the branching ratios for the beta-decay of ^{43}Cr found using (a).

structure, since the beta-delayed three-proton daughter is doubly magic. (ii) It could be due to a wrong estimate of the IAS decay branches. If our model holds for the prediction of the Gamow-Teller strength (i.e. we assume that the $67\,\%$, the $4\,\%$ and the $0.10\,\%$ in Table 8.2 are correct), then about $80\,\%$ of the IAS decays need to be one-proton decays and the rest two-proton decays in order to obtain the experimental results of $81(4)\,\%$, $7.1\,4\%$ and $0.08(3)\,\%$ listed in Table 8.2. From Figure 8.16 we see that this would be the case if the IAS was situated approximately $1\,\mathrm{MeV}$ below the value given in Table 8.3. The uncertainty of the energy of the IAS is only $40\,\mathrm{keV}$ using the new mass measurements [Wan12], and it is thus highly unlikely that the differences are caused by the energy determination of the IAS. However, since the IAS only proton decays through isospin mixing it might have a large gamma branch, which will move the strength downwards, giving a bigger one-proton decay branch. (iii) The difference could originate from the determination of ΔE. However, changing the value of ΔE with up to $2.5\,\mathrm{MeV}$ in both direction does not change the branching ratios significantly. (iv) It could be caused by the Gaussian fit to the data. The branching ratios are highly sensitive to even small changes to the parameters. For example, changing the mean to $4.2\,\mathrm{MeV}$ and the standard deviation to $0.8\,\mathrm{MeV}$ would give the experimentally measured values for the one- and two-proton branching ratio, but at the same time it lowers the three-proton branching ratio by a factor of ten. However, a Gaus-

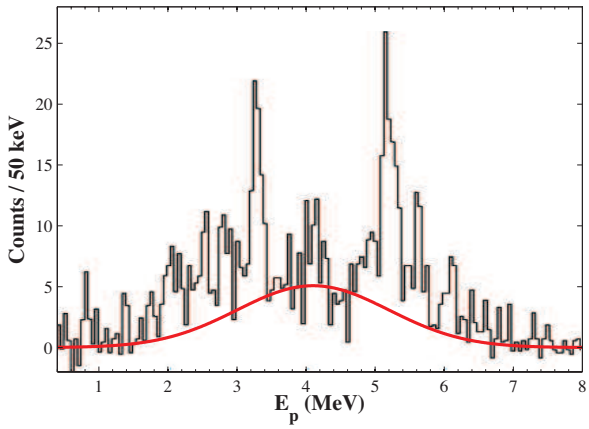

Figure 8.19: The proton energies from the decay of ^{39}Ti measured by Giovinazzo *et al.* [Gio01]. The red distribution is a Gaussian distribution adjusted manually to fit the data.

sian distribution with these parameters would no longer fit the data very well. Considering the data in Figure 8.15 it is more likely that the mean should be slightly smaller than the one used and the standard deviation larger. The dataset in Figure 8.15b seems more flat than the one in Figure 8.15a. This could be due to a possible energy dependent detection efficiency for one of the experiments, which is not taken into account here. The Gaussian distribution does not seem to be the best fit to the data in Figure 8.15b and perhaps another distribution should have been chosen. It is, however, very encouraging that this simple model gives branching ratios this close to the experimentally measured.

8.5.2 ^{39}Ti

The details for the calculation of the total branching ratios for the beta-delayed one-, two- and three-proton decay using our model are described above for the case of ^{43}Cr. As data input for the proton energies, we use the spectra measured by Dossat *et al.* [Dos07] shown in Figure 8.19. As for ^{43}Cr it seems like the distribution is symmetric when neglecting the resolved lines so we once again assume a Gaussian distribution. We obtain the distribution shown in Figure 8.19 with mean $\mu = 4.1\,\mathrm{MeV}$ and standard deviation $\sigma = 1.1\,\mathrm{MeV}$.

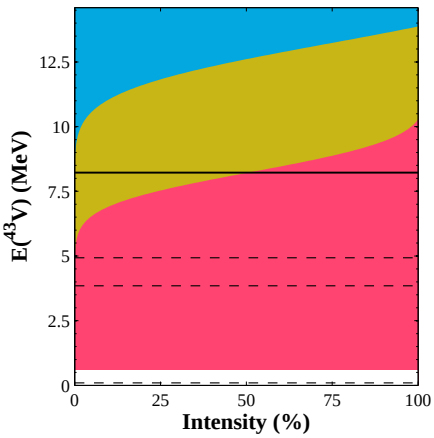

Figure 8.20: The calculated intensities of one- (red), two- (yellow) and three-proton (blue) decays as a function of excitation energy in the beta daughter of ^{39}Ti. The horizontal dashed lines correspond to the one-, two- and three-proton separation energy, respectively. The horizontal full line corresponds to the energy of the IAS. A lower threshold of $500\,\mathrm{keV}$ above the one-proton separation energy is chosen for the one-proton decays and similar for the two- and three-proton decays.

The values for the different parameters that we need as input in the model are given in Table 8.3. The calculated ratios of one-, two- and three-proton decays as a function of excitation energy in the beta daughter of ^{39}Ti are shown in Figure 8.20. The B_{GT} distribution used and the resulting distribution of the branching ratios for the beta-decay are shown in Figure 8.21. Finally, the total branching ratios for the beta-delayed one-, two- and three-proton decay of ^{39}Ti are given in Table 8.2.

Unfortunately there are no experimental measurements of the beta-delayed one-, two- and three-proton branching ratios. According to Ref. [Aud12a] the beta-delayed two-proton branching ratio is estimated to $15\,\%$ presumably based on Ref. [Gio01]. However, studying the results of Giovinazzo *et al.* [Gio01] in detail and comparing their identified peaks with the beta-delayed two-proton spectrum measured my Moltz *et al.* [Mol92], we find that the two peaks measured at energies $2440(25)\,\mathrm{keV}$ and $4880(40)\,\mathrm{keV}$ are most likely due to beta-delayed two-proton decays. The energies measured are the summed energies of the two protons and their branching ratios are found

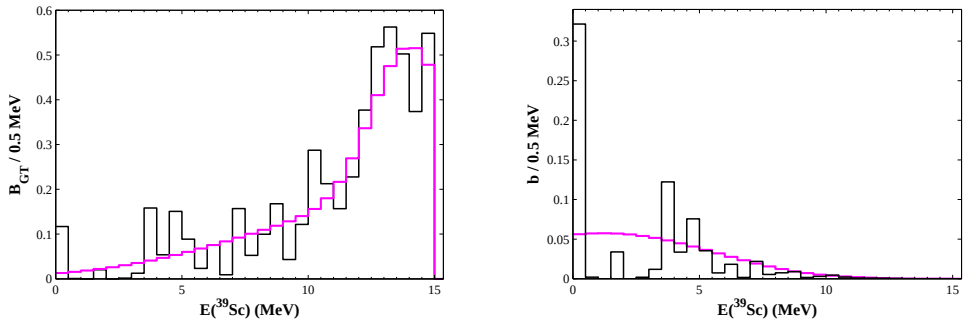

Figure 8.21: (a) The theoretical B_{GT} distributions from Figure 8.13a shifted downwards by $2.0\,\mathrm{MeV}$ used for the decay of ^{39}Ti. (b) The distribution of the branching ratios for the beta-decay of ^{39}Ti found using (a).

to be $8.0(50)\,\%$ and $12.5(65)\,\%$, respectively, giving a total branching ratio of $20.5(82)\,\%$ for beta-delayed two-proton decay. Both Giovinazzo *et al.* and Moltz *et al.* have very limited statistics and we thus turn to the spectrum from Dossat *et al.* [Dos07] shown in Figure 8.19. Dossat *et al.* measure a peak at $5.17(3)\,\mathrm{MeV}$ with branching ratio $10(3)\,\%$, which they assume is the same as the 4.88-MeV peak measured by Giovinazzo *et al.* They only give the branching ratio of the other strong peak at $3.27(2)\,\mathrm{MeV}$, but this is most likely not from beta-delayed two-proton events. So from their results we can only conclude that the branching ratio for beta-delayed two-proton decay is more than $10\,\%$, in agreement with our estimated prediction of $20\,\%$.

CHAPTER 9

Summary and outlook

9.1 Summary

We have studied the complex decay of the drip-line nucleus ^{31}Ar. The large window for beta emission and the small proton separation energies along with our compact setup for particle detection have made it possible for us to use this decay to study a variety of topics.

We have been able to study the exotic three-proton decay mode which was only recently discovered in the decay of ^{31}Ar and has only been observed in two other nuclei. We have performed the first spectroscopic analysis of this decay mode made possible by the good resolution of our setup and the large solid angle for particle detection. We have shown that roughly half of the three-proton events in the decay of ^{31}Ar originate from the isobaric analogue state (IAS) in ^{31}Cl, while the rest originate from higher-lying levels fed in the Gamow-Teller decay. We also see that the three-proton emission is mainly sequential primarily going through the two levels at $3447.6(4)\,\mathrm{keV}$ and $4080.5(3)\,\mathrm{keV}$ in ^{29}P lying above the proton threshold of $2748.6(6)\,\mathrm{keV}$. However, a simultaneous component cannot be excluded due to limited statistics. We have made a quantitative analysis of the beta-delayed two-proton-gamma events to search for gamma transitions from excited states in ^{29}P. Even though we know from the three-proton decay that levels above the proton threshold are populated, only gamma rays from the two lowest excited states in ^{29}P could be clearly identified.

In the process of analysing the data we have developed a new method for finding the geometry of a double-sided silicon strip detector (DSSSD) from its hit-pattern. The method is more robust than the previous, where the source is assumed to be a point, and the new method can thus be used even when the detector is exposed to shading effects. The calibration is made from runs with ^{33}Ar and from these we have improved the energy determinations of three

proton decays from the decay of ^{33}Cl, with proton energies of $1320.1(20)\,\mathrm{keV}$, $2479.2(20)\,\mathrm{keV}$ and $3856.9(20)\,\mathrm{keV}$. The gamma decay from the ^{33}Ar runs have also been examined and we have for the first time in the ^{33}Ar decay seen the M1 gamma decay of the IAS in ^{33}Cl to the anti isobaric analogue state (AIAS). We determine the energy of this transition to be $4734.0(20)\,\mathrm{keV}$. Furthermore, we have used the new results from Lis *et al.* [Lis15] of the total beta-delayed proton branching ratio for normalisation of the total number of ^{31}Ar atoms collected. This reduces the normalisation uncertainty to $3.8\,\%$ from the $11\,\%$ obtained when normalising to the absolute branching ratio of $26.2(29)\,\%$ from Refs. [Axe98a, Baz92] of the strong $2083(3)$-keV one-proton peak. To ease future ^{31}Ar experiments we find the revised absolute branching ratio of this peak to be $25.9(10)\,\%$.

We have improved the previous determinations of the beta-strength in several ways. For the Fermi decay we have analysed all the identified proton channels of the IAS including the recently discovered three-proton decay and contributions from decays to higher-lying levels in ^{30}S than previously observed. To obtain the refined Fermi strength we have used our improved half-life of ^{31}Ar of $15.1(3)\,\mathrm{ms}$, which we have determined from our data. The energy of the IAS is found to be $12.313(4)\,\mathrm{MeV}$ and the branching ratio for the Fermi decay is found to be $3.56(32)\,\%$ when only the proton branches of the IAS are included. We found a gamma signal at $3431(6)$-keV, which is most likely the gamma decay of the IAS, since it does not match any other transition in the ^{31}Ar decay. It is most likely an M1 transition to the AIAS, which then has an energy of $8882(7)\,\mathrm{keV}$. Including this gives a branching ratio for the Fermi decay of $4.30(36)\,\%$, and we have thus accounted for all the decays of the IAS (or almost), since the theoretical value of the Fermi decay branching ratio is $4.24(43)\,\%$, which is found using our improved Coulomb displacement energy of $6.85(10)\,\mathrm{MeV}$.

The determination of the Gamow-Teller strength has been significantly improved from previous measurements. The identified contributions from the one-, two- and three-proton branches are found to be $0.60(2)(2)$, $2.11(19)(8)$ and $1.03(28)(4)$, respectively. By comparison with a shell-model calculation we have shown that we can account for the majority of the strength distribution.

We have measured all three proton decay modes with a good energy res-

olution. This made it possible to study the evolution of the proton decay modes in the same way as is done for neutron emission for nuclei close to stability [Gho50, Mor53]. We have shown that the evolution of the proton channels follows the same tendency with the multiplicity of the dominating decay mode increasing with increasing excitation energy. Furthermore, we have shown that with a simplified model it is possible to give an estimate of the Q_{2p} and Q_{3p} distributions from the Q_{1p} distribution, when disregarding resolved lines, and that we can use this simple model to make predictions of the beta-delayed one-, two- and three-proton branching ratios in other decays. We have used the model to make predictions for the decay of ^{39}Ti and ^{43}Cr, where the latter can be compared to experimental data and shows an encouraging agreement, when taking the limitations of the model into account.

We have examined the gamma spectrum from the decay of ^{31}Ar and identified the ground state decay of the two lowest lying levels in ^{29}P and ^{30}S and the decay of the second excited level and the $4689.1(24)$-keV to the ground state. The latter is observed for the first time in the decay of ^{31}Ar. Finally, as mentioned above, we have found a gamma line at $3431(6)$-keV, which we assign to the decay of the IAS in ^{31}Cl. We have shown that the gamma lines from the short-lived levels in ^{30}S (and in ^{32}S in the decay of ^{33}Ar) are Doppler broadened due to the previous proton decay. The resolution of these lines can thus be improved by correcting for the Doppler shift.

The levels of ^{30}S above the proton threshold (and up to about $6\,\mathrm{MeV}$) are of interest to astrophysics, since their characteristics are essential when determining the $^{29}\mathrm{P}(p,\gamma)^{30}\mathrm{S}$ reaction rate, which influences explosive hydrogen burning in type I x-ray bursts and classical novae. We have identified three such levels in the beta-delayed two-proton decay at $5227(3)\,\mathrm{keV}$, $5390(4)\,\mathrm{keV}$ and $5845(5)\,\mathrm{keV}$ besides the one found in the gamma decay at $4689.1(24)\,\mathrm{keV}$, which is one of the two levels, which strongest influence the $^{29}\mathrm{P}(p,\gamma)^{30}\mathrm{S}$ reaction rate. We have developed a new analysis method, by which we identify the protons feeding the level of interest and gate on these. In this way we are able to lower our background significantly and provide experimental limits on the ratio between the proton and gamma partial widths. The upper limit of the Γ_p/Γ_γ ratio has been found for the $4689.1(24)\,\mathrm{keV}$ level to be 0.19 ($95\,\%$ C.L.), which is well above the theoretical predictions of 0.37×10^{-2} [Set13] and 0.27×10^{-2} [Ric13]. For the three levels identified in the two-proton de-

cay an upper limit on the Γ_γ/Γ_p are found to be 0.5, 7 and 10 ($95\,\%$ C.L.), respectively, where the latter are in conflict with the 15.7 obtained by calculations in Ref. [Alm12]. Furthermore, we have studied the decay of the IAS trough the levels just above the proton threshold. Even though we cannot positively identify the 4809-keV level, our analysis suggest that the proton branching ratio of this level is smaller than what is currently expected from calculations. This level has the strongest influence on the $^{29}\mathrm{P}(p,\gamma)^{30}\mathrm{S}$ reaction rate and this issue should thus be further examined by experiments.

The spin of the levels of astrophysical interest in ^{30}S is also important when determining the $^{29}\mathrm{P}(p,\gamma)^{30}\mathrm{S}$ reaction rate and there is still some disagreement in their spin assignment. We present a new method of determining the spin using angular correlations between the two protons in the beta-delayed two-proton decay passing through the level of interest. Due to the spins of the ^{31}Cl levels being unknown an ensemble of states in ^{31}Cl is used. We use the method for the strongest populated level at $5227(3)\,\mathrm{keV}$ and find it to have spin 3^+ or 4^+, with the data favouring a 3^+ assignment. When comparing with the mirror nucleus and the measurements from Ref. [Lot12] we find that the spin should be either 3^+ or 0^+ and thus conclude that we populate a 3^+ level. However, due to our limited statistics we cannot exclude that a 0^+ level with approximately the same energy is also populated, which could explain the difference between our measured energy of $5227(3)\,\mathrm{keV}$ and the one measured in Ref. [Lot12] of $5218.8(3)\,\mathrm{keV}$.

Finally, we have attempted to explain the strong feeding of the $5227(3)$-keV level by a simple picture, where we consider ^{31}Ar to consist of a core of ^{30}Cl plus a $1d_{3/2}$ proton. We then view the beta-delayed proton decay of ^{31}Ar as a beta decay of the ^{30}Cl core with a subsequent emission of the spectator proton. The levels populated in ^{30}S are thus determined by the beta decay of ^{30}Cl, which we find would favour population of a 3^+ state, by comparing with the mirror nucleus. When comparing with the mirror process, we also find that the strongest populated levels (including the ones below the proton threshold) are the same in the two.

9.2 Outlook

With the results presented here, we have shown that the beta decay of nuclei close to the drip-line is a competitive tool for studying spectroscopic properties of nuclear levels. Reaction experiments normally suffer from a large background and a large scattering of the reaction products in the detector. This is not the case when using the beta decay as a probe. The beta-decaying nuclei can be implanted on a thin foil with a relatively small background and since there is no scattering we obtain a very clean spectroscopic system. We have shown that beta-decay experiments are competitive with reaction experiments in accessing information of astrophysical interest even though we populate the relevant levels in two steps from the drip-line, while the reaction experiments populate the levels in two steps from stable nuclei.

Even though the results in this thesis are competitive it is clear that an experiment with a purer beam and a higher yield, would make it possible to improve most of the results. After the experiment was performed significant developments have been made at ISOLDE on the primary target, which shows that a nano-structured CaO target should improve the yield with an order of magnitude [Ram14]. In addition we showed during the experiment that lowering the temperature of the primary target also lowered the nitrogen contamination in the beam.

With this beam, the same amount of beam time, a compact setup for particle detection (with backing on all DSSSDs) and a large coverage for detection of gamma particles it should be possible to provide values for the Γ_p/Γ_γ ratio of both the 4688-keV and 4809-keV levels relevant to astrophysics. Furthermore, it would be possible to investigate the beta-delayed three-proton decay in greater detail and shed further light on the decay mechanism. An experiment of this sort has been proposed [Alg13]. The proposal was approved and the experiment was carried out in October 2014. Unfortunately the beam time was shorter than for the experiment presented here and the anticipated improved yield was not obtained. Still the improved setup should make it possible to improve some of the results presented here. The experiment is currently being analysed by a PhD student in our collaborating group at CSIC in Madrid.

The new analysis methods developed here could also benefit other beta-

decay studies with subsequent particle emission. The methods developed here for finding the spin and the ratio between the proton and gamma partial widths for levels in ^{30}S could for example be used to study the astrophysically interesting ^{25}Al(p,γ)^{26}Si reaction using the beta-delayed proton decays of ^{27}S. However, due to the large reactivity of sulphur this isotope is not easily extracted from the primary target unit at ISOLDE so a ^{27}S beam with a sufficient yield is currently not available.

Naturally, it would also be interesting to use the method for predicting beta-delayed one-, two- and three-proton branching ratios from the decay of other nuclei along the drip-line to search for new possible beta-delayed three-proton emitters. The problem with the method is that it needs a good proton spectrum as an input. The most promising nuclei with fairly good one- and two-proton data include ^{27}S, ^{23}Si and ^{35}Ca and naturally it would be desirable to also use the model on the known three-proton emitter ^{45}Fe.

Bibliography

[Adi10] Adimi, N. et al., *Detailed β-decay study of ^{33}Ar*, Phys. Rev. C **81** (2010), 024311.

[Alb74] Alburger, D. E. and Goosman, D. R., *Decay schemes of ^{30}Al, ^{30}P, and ^{20}O*, Phys. Rev. C **9** (1974), 2236.

[Alg13] Algora, A. et al., *β3p spectroscopy and proton-γ width determination in the decay of ^{31}Ar*, Proposal CERN INTC-P-386, IS577, 2013, Spokespersons: Fynbo, H. O. U. and Koldste, G. T., `http://cds.cern.ch/record/1602880?ln=en`.

[Alm12] Almaraz-Calderon, S. et al., *Level structure of ^{30}S and its importance in the $^{28}Si(\alpha,p)^{29}P$ and $^{29}P(p,\gamma)^{30}S$ reaction rates*, Phys. Rev. C **86** (2012), 065805.

[Ama01] Amari, S. et al., *Presolar grains from novae*, Astrophys. J. **551** (2001), 1065.

[And72] Anderson, P. W., *More is different*, Science **177** (1972), no. 4047, 393.

[Ant84] Antony, M. S. and Pape, A., *Isobaric mass systematics for $A \leq 60$*, Phys. Rev. C **30** (1984), 1286.

[ATL12] ATLAS Collaboration, *Observation of a new particle in the search for the Standard Model Higgs boson with the ATLAS detector at the LHC*, Physics Letters B **716** (2012), 1.

[Aud12a] Audi, G. et al., *The ame2012 atomic mass evaluation*, Chin. Phys. C **36** (2012), 1287.

[Aud12b] Audirac, L. et al., *Direct and β-delayed multi-proton emission from atomic nuclei with a time projection chamber: the cases of ^{43}Cr, ^{45}Fe, and ^{51}Ni*, Eur. Phys. J. A **48** (2012), 179.

[Axe98a] Axelsson, L. et al., *Beta decay of ^{31}Ar*, Nuclear Physics A **634** (1998), 475, Erratum ibid **641** (1998), 529.

[Axe98b] Axelsson, L. et al., *Two-proton emission in the decay of ^{31}Ar*, Nucl. Phys. A **628** (1998), 345.

[Bar00] Barlow, R., *SLUO Lectures on Statistics and Numerical Methods in HEP - Lecture 7: Fitting Methods*, `http://www-group.slac.stanford.edu/sluo/lectures/stat_lecture_files/sluolec7.pdf`, 28th of August 2000.

[Bar07] Bardayan, D. W. et al., *^{30}S studied with the $^{32}S(p,t)^{30}S$ reaction and the $^{29}P(p,\gamma)^{30}S$ reaction rate*, Phys. Rev. C **76** (2007), 045803.

[Bas10] Basunia, M. S., *Nuclear data sheets for $A = 30$*, Nucl. Data Sheets **111** (2010), 2331.

[Bas12] Basunia, M. S., *Nuclear data sheets for $A = 29$*, Nucl. Data Sheets **113** (2012), 909.

[Baz92] Bazin, D. et al., *Decay modes of ^{31}Ar and first observation of β-delayed three-proton radioactivity*, Phys. Rev. C **45** (1992), 69.

[Bea12] Beane, S. R. et al., *Deuteron and exotic two-body bound states from lattice QCD*, Phys. Rev. D **85** (2012), 054511.

[Bel08] Belle Collaboration, *Observation of a resonancelike structure in the $\pi^{+-}\psi^{'}$ mass distribution in exclusive $B \to K\pi^{+-}\psi^{'}$ decays*, Phys. Rev. Lett. **100** (2008), 142001.

[Bel13] Belle Collaboration, *Experimental constraints on the spin and parity of the $Z(4430)^{+}$*, Phys. Rev. D **88** (2013), 074026.

[Bha08] Bhattacharya, M. et al., *ft value of the $0^{+} \to 0^{+}$ β^{+} decay of ^{32}Ar: A measurement of isospin symmetry breaking in a superallowed decay*, Phys. Rev. C **77** (2008), 065503.

[Bie53] Biedenharn, L. C. and Rose, M. E., *Theory of angular correlation of nuclear radiations*, Rev. Mod. Phys. **25** (1953), 729.

[Bjö85] Björnstad, T. et al., *Study of the giant Gamow-Teller resonance in nuclear β-decay: The case of ^{32}Ar*, Nucl. Phys. A **443** (1985), 283.

[Bla08] Blank, B. and Borge, M. J. G., *Nuclear structure at the proton drip line: Advances with nuclear decay studies*, Prog. Part. Nucl. Phys. **60** (2008), 403.

[Bor87a] Borge, M. J. G. et al., *Study of the Giant Gamow-Teller Resonance in nuclear beta decay: The case of ^{33}Ar*, Phys. Scr. **36** (1987), 218.

[Bor87b] Borrel, V. et al., *Beta-delayed proton decay of the $T_z = -\frac{5}{2}$ isotope ^{31}Ar*, Nucl. Phys. A **473** (1987), 331.

[Bor90] Borge, M. et al., *The decay of ^{31}Ar*, Nucl. Phys. A **515** (1990), 21.

[Bor91] Borrel, V. et al., *^{31}Ar and ^{27}S: Beta-delayed two-proton emission and mass excess*, Nucl. Phys. A **531** (1991), 353.

[Bor13] Borge, M. J. G., *Beta-delayed particle emission*, Phys. Scr. **2013** (2013), 014013.

[Bro06] Brown, B. A. and Richter, W. A., *New "usd" hamiltonians for the sd shell*, Phys. Rev. C **74** (2006), 034315.

[Bro15] Brown, B. A., *Private communication*, 2015.

[Cau95] Caurier, E., Poves, A., and Zuker, A. P., *Missing and quenched Gamow-Teller strength*, Phys. Rev. Lett. **74** (1995), 1517.

[CER] CERN Program Libary (CERNLIB), `https://cernlib.web.cern.ch/cernlib/`.

[Che11] Chen, J. and Singh, B., *Nuclear data sheets for $A = 33$*, Nucl. Data Sheets **112** (2011), 1393.

[CMS12] CMS Collaboration, *Observation of a new boson at a mass of 125 GeV with the CMS experiment at the LHC*, Physics Letters B **716** (2012), 30.

[Dét91] Détraz, C., *The branching ratio of β-delayed two-proton emission*, Z. Phys. A **340** (1991), 227 (English).

[D'A86] D'Agostino, R. B. and Stephens, M. A., *Goodness-of-Fit Techniques*, Marcel Dekker, Inc, 1986.

[Deb88] Debertin, K. and Helmer, R. G., *Gamma- and X-ray spectrometry with semiconductor detectors*, North-Holland, 1988.

[Dos07] Dossat, C. et al., *The decay of proton-rich nuclei in the mass $A = 36$–56 region*, Nuclear Physics A **792** (2007), 18.

[Dür08] Dürr, S. et al., *Ab initio determination of light hadron masses*, Science **322** (2008), no. 5905, 1224.

[End78] Endt, P. and Leun, C. V. D., *Energy levels of $A = 21$–44 nuclei (VI)*, Nucl. Phys. A **310** (1978), 1.

[Erl12] Erler, J. et al., *The limits of the nuclear landscape*, Nature **486** (2012), 509.

[Esw72] Eswaran, M. A., Ismail, M., and Ragoowansi, N. L., *Studies on analog states in ^{33}Cl by isospin-forbidden resonances in the reaction $^{32}S(p,\gamma)^{33}Cl$*, Phys. Rev. C **5** (1972), 1270–1277.

[Fel98] Feldman, G. J. and Cousins, R. D., *Unified approach to the classical statistical analysis of small signals*, Phys. Rev. D **57** (1998), 3873.

[Fis04] Fisker, J. L. et al., *The nuclear reaction waiting points: ^{22}Mg, ^{26}Si, ^{30}S, and ^{34}Ar and bolometrically double-peaked type I X-Ray bursts*, Astrophys. J. **608** (2004), L61.

[Fis08] Fisker, J. L. et al., *Explosive hydrogen burning during type I X-ray bursts*, Astrophys. J. Suppl. Ser. **174** (2008), 261.

[Fyn99] Fynbo, H. O. U. et al., *^{31}Ar examined: New limit on the β-delayed three-proton branch*, Phys. Rev. C **59** (1999), 2275.

[Fyn00] Fynbo, H. O. U. et al., *The $\beta 2p$ decay mechanism of ^{31}Ar*, Nucl. Phys. A **677** (2000), 38.

[Fyn03] Fynbo, H. O. U., *Doppler broadened γ-lines from exotic nuclei*, Nucl. Instrum. Meth. B **207** (2003), 275.

[Fyn08] Fynbo, H. O. U. et al., *Studies of β-delayed two-proton emission : The cases of ^{31}Ar and ^{35}Ca*, Proposal CERN INTC-P-248, IS476, 2008,

Spokespersons: Fynbo, H. O. U. and Blank, B., `http://cds.cern.ch/record/1100376?ln=en`.

[Fyn15] Fynbo, H. O. U., *Private communication*, 2015.

[Gho50] Ghoshal, S. N., *An experimental verification of the theory of compound nucleus*, Phys. Rev. **80** (1950), 939.

[Gio01] Giovinazzo, J. et al., *Decay of proton-rich nuclei between ^{39}Ti and ^{49}Ni*, Eur. Phys. J. A. **10** (82001), 73.

[Gol60] Goldansky, V., *On neutron-deficient isotopes of light nuclei and the phenomena of proton and two-proton radioactivity*, Nucl. Phys. **19** (1960), 482.

[Gol61] Goldansky, V., *Two-proton radioactivity*, Nucl. Phys. **27** (1961), 648.

[Hor72] Hornshøj, P. et al., *Beta-delayed proton emission from heavy nuclei: (II). The calculation of spectral shapes and intensities in a compound-nucleus model*, Nucl. Phys. A **187** (1972), 609.

[Ili01] Iliadis, C. et al., *Proton-induced thermonuclear reaction rates for $A = 20$–40 nuclei*, Astrophys. J. Suppl. Ser. **134** (2001), 151.

[Ili02] Iliadis, C. et al., *The effects of thermonuclear reaction-rate variations on nova nucleosynthesis: A sensitivity study*, Astrophys. J. Suppl. Ser. **142** (2002), 105.

[Ili07] Iliadis, C., *Nuclear Physics of Stars*, Wiley-VCH, 2007.

[Jac98] Jackson, J. D., *Classical Electrodynamics*, John Wiley & Sons, 1998.

[Jam06] James, F., *Statistical Methods in Experimental Physics*, World Scientific Publishing Co. Pte. Ltd., 2006.

[Jen87] Jensen, A. S. and Siemens, P. J., *Elements of Nuclei*, Addison Wesley, 1987.

[Joh13] Johansen, J. G. et al., *Experimental study of bound states in ^{12}Be through low-energy ^{11}Be(d,p)-transfer reactions*, Phys. Rev. C **88** (2013), 044619.

[Jon04] Jonson, B., *Light dripline nuclei*, Phys. Rep. **389** (2004), 1.

[Jos01] José, J., Coc, A., and Hernanz, M., *Synthesis of intermediate-mass elements in classical novae: From Si to Ca*, Astrophys. J. **560** (2001), 897.

[Jos04] José, J. et al., *The imprint of nova nucleosynthesis in presolar grains*, Astrophys. J. **612** (2004), 414.

[Klo74] Klotz, G. and Walter, G., *Désintégration β^- de ^{30}Al*, Nucl. Phys. A **227** (1974), 341.

[Kol09] Koldste, G. T., *β-forsinket to-proton udsendelse af ^{31}Ar*, Bachelor's project, Aarhus University, 2009.

[Kol13] Koldste, G. T. et al., *Relative proton and γ widths of astrophysically important states in ^{30}S studied in the β-delayed decay of ^{31}Ar*, Phys. Rev. C **87** (2013), 055808.

[Kol14a] Koldste, G. T. et al., *Multi-particle emission in the decay of ^{31}Ar*, Phys. Rev. C **89** (2014), 064315.

[Kol14b] Koldste, G. T. et al., *Sizeable beta-strength in ^{31}Ar ($\beta 3p$) decay*, Phys. Lett. B **737** (2014), 383.

[Kuh73] Kuhlmann, E. et al., *The γ-ray decay of levels in ^{30}S*, Nucl. Phys. A **213** (1973), 82.

[Kus11] Kusk, J. H., *Gamma-rays in the decay of ^{31}Ar, ^{32}Ar and ^{33}Ar*, Master's thesis, Aarhus University, 2011.

[Lam13] Lam, Y. H. et al., *The isobaric multiplet mass equation for revisited*, At. Data Nucl. Data Tables **99** (2013), 680.

[Lan00] Langanke, K. and Martínez-Pinedo, G., *Shell-model calculations of stellar weak interaction rates: II. Weak rates for nuclei in the mass range $A = 45$–65 in supernovae environments*, Nuclear Physics A **673** (2000), 481.

[LHC14] LHCb Collaboration, *Observation of the resonant character of the $Z(4430)^-$ state*, Phys. Rev. Lett. **112** (2014), 222002.

[LHC15] LHCb Collaboration, *Observation of $J/\Psi p$ resonances consistent with pentaquark states in $\Lambda_b^0 \to J/\Psi K^- p$ decays*, arXiv (2015), 1507.03414.

[Lis15] Lis, A. et al., *β-delayed three-proton decay of ^{31}Ar*, arXiv (2015), 1505.07990.

[Lot12] Lotay, G. et al., *Level structure of ^{30}S: Implications for the astrophysical $^{29}P(p,\gamma)^{30}S$ reaction rate in ONe novae and X-ray bursts*, Phys. Rev. C **86** (2012), 042801.

[Mat09] Matea, I. et al., *The Silicon Cube detector*, Nucl. Instrum. Meth. A **607** (2009), 576.

[Mie07] Miernik, K. et al., *First observation of β-delayed three-proton emission in ^{45}Fe*, Phys. Rev. C **76** (2007), 041304.

[Mol92] Moltz, D. et al., *Beta-delayed two-proton decay of ^{39}Ti*, Z. Phys. A **342** (1992), 273 (English).

[Mor53] Morrison, P., *A Survey of Nuclear Reactions*, John Wiley, 1953, Part VI of Experimental Nuclear Physics, Vol II, E. Serge (Ed).

[Nil00] Nilsson, T., Nyman, G., and Riisager, K., *Halo-nuclei at ISOLDE*, Hyperfine Interactions **129** (2000), 67.

[Nit05] Nittler, L. R. and Hoppe, P., *Are presolar silicon carbide grains from novae actually from supernovae?*, Astrophys. J. Lett. **631** (2005), 89.

[Oue11] Ouellet, C. and Singh, B., *Nuclear data sheets for $A = 32$*, Nucl. Data Sheets **112** (2011), 2199.

[Pen10] Penescu, L. et al., *Development of high efficiency Versatile Arc Discharge Ion Source at CERN ISOLDE*, Rev. Sci. Instr. **81** (2010), 02A906.

[Pfü12a] Pfützner, M. et al., *Observation of beta-delayed three-proton emission from ^{31}Ar with the Optical Time Projection Chamber at the FRS*, GSI Scientific Report (2012), 147.

[Pfü12b] Pfützner, M. et al., *Radioactive decays at limits of nuclear stability*, Rev. Mod. Phys. **84** (2012), 567.

[Pom11] Pomorski, M. et al., *β-delayed proton emission branches in ^{43}Cr*, Phys. Rev. C **83** (2011), 014306.

[Rad95] Radford, D. C., *ESCL8R and LEVIT8R: Software for interactive graphical analysis of HPGe coincidence data sets*, Nucl. Instrum. Meth. A **361** (1995), 297.

[Ram14] Ramos, J. P. et al., *Intense 31-35Ar beams produced with nano-structured CaO target at ISOLDE*, Nucl. Instrum. Meth. B **320** (2014), 83.

[Rei89] Reiff, J. et al., *A fast in-beam recoil catcher wheel and the observation of beta-delayed two-proton emission from ^{31}Ar*, Nucl. Instrum. Meth. A **276** (1989), 228.

[Ric13] Richter, W. A. and Brown, B. A., *Shell-model studies of the astrophysical rp reaction $^{29}P(p,\gamma)^{30}S$*, Phys. Rev. C **87** (2013), 065803.

[Saa11] Saastamoinen, A., *Studies of $T_2 = -3/2$ nuclei of astrophysical interest*, Ph.D. thesis, University of Jyväskylä, 2011.

[Sch11] Schatz, H., *Rare isotopes in thermonuclear explosions on neutron stars*, Prog. Part. Nucl. Phys. **66** (2011), 277.

[Set10] Setoodehnia, K. et al., *Structure of ^{30}S with $^{32}S(p,t)^{30}S$ and the thermonuclear $^{29}P(p,\gamma)^{30}S$ reaction rate*, Phys. Rev. C **82** (2010), 022801.

[Set11] Setoodehnia, K. et al., *Spins and parities of astrophysically important ^{30}S states from $^{28}Si(^3He,n\gamma)^{30}S$*, Phys. Rev. C **83** (2011), 018803.

[Set13] Setoodehnia, K. et al., *Nuclear structure of ^{30}S and its implications for nucleosynthesis in classical novae*, Phys. Rev. C **87** (2013), 065801.

[Sou11] Souin, J. et al., *Precision half-life and Q-value measurement of the superallowed β emitter ^{30}S*, Eur. J. phys. A **47** (2011), 40.

[Tho09] Thompson, I. J. and Nunes, F. M., *Nuclear reactions for astrophysics*, Cambridge University Press, 2009.

[Tow10] Towner, I. S. and Hardy, J. C., *The evaluation of V_{ud} and its impact on the unitarity of the Cabibbo–Kobayashi–Maskawa quark-mixing matrix*, Rep. Prog. Phys. **73** (2010), 046301.

[Wan12] Wang, M. et al., *The AME2012 atomic mass evaluation*, Chinese Phys. C **36** (2012), 1603.

[War13] Warr, N. et al., *The Miniball spectrometer*, Eur. Phys. J. A **49** (2013), 40.

[Wil69] Wilkinson, D., *Isospin in Nuclear Physics*, North-Holland, 1969.

[Wil74] Wilkinson, D. and Macefield, B., *A parametrization of the phase space factor for allowed β-decay*, Nucl. Phys. A **232** (1974), 58.

[Wil80] Wilson, H. S. et al., *Gamow-Teller transitions in some intermediate-mass nuclei*, Phys. Rev. C **22** (1980), 1696.

[Yok82] Yokota, H. et al., *The $T = 1$, isospin triplet states in $A = 30$ nuclei*, Nucl. Phys. A **383** (1982), 298.

[Zie83] Ziegler, J. F., *SRIM - The Stopping and Range of Ions in Matter*, `http://www.srim.org`, 1983.

List of Figures

List of Tables